MATTHIAS PUHR

TRANSPORT PROPERTIES OF CHIRAL FERMIONS

TRANSPORT PROPERTIES OF CHIRAL FERMIONS

DISSERTATION

zur Erlangung des Doktorgrades der Naturwissenschaften (Dr. rer. nat.) der Fakultät für Physik der Universität Regensburg

vorgelegt von

Matthias Puhr
aus Oberwart, Österreich

März 2017

Die Arbeit wurde von Dr. Pavel Buividovich angeleitet.

Das Promotionsgesuch wurde am 25.01.2017 eingereicht.
Das Promotionskolloquium fand am 26.04.2017 statt.

Prüfungsausschuss:

Vorsitzender:	Prof. Dr. Dieter Weiss
1. Gutachter:	Dr. Pavel Buividovich
2. Gutachter:	Prof. Dr. Tilo Wettig
weiterer Prüfer:	Prof. Dr. Klaus Richter

Id fieri potest, ut fallar.

ABSTRACT

Anomalous transport phenomena have their origin in the chiral anomaly, the anomalous non-conservation of the axial charge, and can arise in systems with chiral fermions. The anomalous transport properties of free fermions are well understood, but little is known about possible corrections to the anomalous transport coefficients that can occur if the fermions are strongly interacting.

The main goal of this thesis is to study anomalous transport effects in media with strongly interacting fermions. In particular, we investigate the Chiral Magnetic Effect (CME) in a Weyl Semimetal (WSM) and the Chiral Separation Effect (CSE) in finite-density Quantum Chromodynamics (QCD).

The recently discovered WSMs are solid state crystals with low-energy excitations that behave like Weyl fermions. The inter-electron interaction in WSMs is typically very strong and non-perturbative calculations are needed to connect theory and experiment. To realistically model an interacting, parity-breaking WSM we use a tight-binding lattice Hamiltonian with Wilson-Dirac fermions. This model features a non-trivial phase diagram and has a phase (Aoki phase/axionic insulator phase) with spontaneously broken $\mathcal{CP}$ symmetry, corresponding to the phase with spontaneously broken chiral symmetry for interacting continuum Dirac fermions. We use a mean-field ansatz to study the CME in spatially modulated magnetic fields and find that it vanishes in the Aoki phase. Moreover, our calculations show that outside of the Aoki phase the electron interaction has only a minor influence on the CME. We observe no enhancement of the magnitude of the CME current.

For our non-perturbative study of the CSE in QCD we use the framework of lattice QCD with overlap fermions. We work in the quenched approximation to avoid the sign problem that comes with introducing a finite chemical potential on the lattice. The overlap operator calls for the evaluation of the sign function of a matrix with a dimension proportional to the volume of the lattice. For reasonably large lattices it is not feasible to compute the matrix sign function exactly and one has to resort to approximation methods. To compute conserved currents for the overlap operator it is necessary to take derivatives of the overlap operator with respect to the $\mathrm{U}(1)$ lattice gauge field. Depending on which approximation is used to evaluate the overlap operator it is not always clear how to compute this derivative. We develop and implement a new numerical method to take derivatives of matrix functions. This method makes it possible to calculate the conserved currents of the finite-density overlap operator with high precision and opens the way to explore anomalous transport phenomena on the lattice.

We study the CSE in the confining and deconfining phase of QCD. On very small lattices we observe corrections to the CSE in the phase with broken chiral symmetry, which seem to be of topological origin. For larger lattices we find that in both phases the CSE current is the same as for free fermions.

PUBLICATIONS

Some ideas, results, and figures in this work were previously published in the form of conference proceedings or research papers. The following is a list of all publications related to this thesis:

[1] M. Puhr and P. V. Buividovich. 'A Method to Calculate Conserved Currents and Fermionic Force for the Lanczos Approximation to the Overlap Dirac Operator'. *PoS(LATTICE2014)047* (2014). arXiv: 1411.0477.

[2] P. V. Buividovich and M. Puhr. 'A lattice mean-field study of the phase diagram of interacting parity-breaking Weyl semimetals'. *PoS(Lattice2014)061* (2014). arXiv: 1410.6704.

[3] P. V. Buividovich, M. Puhr and S. N. Valgushev. 'Chiral magnetic conductivity in an interacting lattice model of parity-breaking Weyl semimetal'. *Phys. Rev. B* 92, 205122 (2015). arXiv: 1505.04582.

[4] S. N. Valgushev, M. Puhr and P. V. Buividovich. 'Chiral Magnetic Effect in finite-size samples of parity-breaking Weyl semimetals'. *PoS(Lattice2015)043* (2015). arXiv: 1512.01405.

[5] M. Puhr and P. Buividovich. 'A numerical method to compute derivatives of functions of large complex matrices and its application to the overlap Dirac operator at finite chemical potential'. *Comput. Phys. Commun.* 208 (2016), pp. 135–148. arXiv: 1604.08057.

[6] M. Puhr and P. Buividovich. 'A method to compute derivatives of functions of large complex matrices'. *PoS(LATTICE2016)257* (2016). arXiv: 1611.00195.

[7] M. Puhr and P. Buividovich. 'A numerical study of non-perturbative corrections to the Chiral Separation Effect in quenched finite-density QCD'. *Submitted to PRL* (2016). arXiv: 1611.07263.

ACKNOWLEDGMENTS

First of all, I want to thank my supervisor Dr. Pavel Buividovich for inviting me to Regensburg, giving me the opportunity to work on interesting research topics, and for his guidance.

I have always enjoyed the pleasant and inspiring working environment in our research group and want to thank all my current and former colleagues for contributing to that atmosphere. I am grateful to Arthur Dromard, Maksim Ulybyshev, and Semen Valgushev for many exciting discussions. I am indebted to Markus Pak for his collaboration on a research project and for many interesting conversations.

For proofreading of this thesis I thank Arthur Dromard, Eva Grünwald, and Darjan Kozic.

I am deeply grateful to my family and especially to my parents for their constant support and encouragement. I would never have come so far without them. Finally, I want to thank my girlfriend Andrea. Her love and support are invaluable to me.

CONTENTS

ACRONYMS

BiCGSTAB Biconjugate Gradient Stabilized

CG Conjugate Gradient

CME Chiral Magnetic Effect

CSE Chiral Separation Effect

QCD Quantum Chromodynamics

QED Quantum Electrodynamics

TSL Two-Sided Lanczos

WSM Weyl Semimetal

Part I

INTRODUCTION

1

PREAMBLE

The development of quantum field theory, the combination of quantum mechanics and special relativity, is one of the biggest triumphs of theoretical physics. In the Standard Model of particle physics all elementary interactions, except gravity, are described by quantum field theory. The Standard Model has proven to be a very accurate and successful description of nature. The applicability of quantum field theoretical concepts is not limited to particle physics. Quantum field theory has also become an important tool in other branches of physics, for example in solid state physics.

Quantum mechanics gives rise to a variety of fascinating new phenomena, which are absent in classical physics. Although most of these effects can only be observed on a microscopic scale, also macroscopic quantum effects exist. Well known examples are superfluidity and superconductivity. Anomalous transport phenomena, which are the topic of this thesis, are also a macroscopic manifestation of a quantum field theoretical effect, namely of the chiral anomaly.

Anomalous transport phenomena in systems with chiral fermions play an important role in many different areas of physics, ranging from high energy physics and heavy ion collision experiments [1–3] over solid state physics [4–6] to astrophysics [7–11]. For free chiral fermions the anomalous transport coefficients are fixed by the anomaly. It has been argued that the transport coefficients are universal and do not achieve any corrections in interacting theories, because of their relation to the anomaly. There are, however, two scenarios where fermion interactions can instigate corrections to the anomalous transport coefficients: In the case of spontaneous chiral symmetry breaking [12–14] and if the electric current is coupled to a dynamical gauge field [15–17].

The goal of this thesis is to investigate possible corrections to the anomalous transport coefficients in theories with strongly interacting fermions. We consider applications in condensed matter physics and high energy physics. In particular, we study the Chiral Magnetic Effect in Weyl Semimetals and the Chiral Separation Effect in dense QCD. For better clarity this work is divided into several parts. The parts dealing with the Chiral Magnetic Effect and the Chiral Separation Effect have their own specific introduction and separate conclusions.

In the remaining chapters of this introductory part we briefly discuss gauge theories and chiral symmetry in the continuum. Moreover, we introduce lattice gauge theory and explain how chiral symmetry can be implemented on the lattice. The final chapter of Part I deals with the chiral anomaly and describes the anomalous transport effects we study in Part II and Part III.

Part II is dedicated to the investigation of the Chiral Magnetic Effect in Weyl Semimetals. We present a model of a parity-breaking Weyl Semimetal and use a mean-field ansatz to calculate the phase diagram of the model. We then compute the chiral magnetic conductivity and try to connect our results to experiments.

The study of the Chiral Separation Effect in dense QCD is the topic of Part III. As a first step we have to develop the necessary numerical tools to compute conserved currents of chiral lattice fermions. Before applying these tools to physical calculations we validate them in a test setup. Finally, we calculate the chiral separation conductivity in quenched lattice QCD and discuss our results.

In Part IV we present an outlook and describe possible future research directions.

2

LATTICE GAUGE THEORY

In this work we are interested in the physics of strongly interacting fermions, where perturbative calculations are not possible and more advanced techniques have to be employed. Lattice gauge theory is a very successful numerical tool to study strongly interacting field theories non-perturbatively. In the following, we briefly review the aspects of lattice gauge theory that will be used throughout this thesis. For this introduction textbooks on quantum field theory [18–20] and lattice gauge theory [21, 22] were consulted.

2.1 CONTINUUM GAUGE THEORY

We start by considering a general gauge theory with N_f different species, or flavours, of fermions in the continuum. The fermion fields Ψ depend on the (4-dimensional) space-time coordinate x and have three indices

$$\Psi = \Psi^f_{\mu,c}(x) \qquad \bar{\Psi} = \bar{\Psi}^f_{\mu,c}(x), \tag{2.1}$$

where μ is the Dirac index, c is a gauge index and the index f numbers the N_f different flavours. The gauge field A also depends on the space-time coordinate x and carries a Dirac index and gauge indices

$$A = A_{\mu,cd}(x). \tag{2.2}$$

To avoid a cluttered notation we switch to a matrix-vector notation from now on and do not show the indices explicitly. The action of the theory is given by

$$S(\psi, \bar{\psi}, A) = \underbrace{\int dx^4\, \bar{\psi}(x)\,(i\gamma_\mu D^\mu - M)\,\psi(x)}_{S_F} - \underbrace{\int dx^4 \frac{1}{2g^2}\,\mathrm{tr}\,(F_{\mu\nu}(x)F^{\mu\nu}(x))}_{S_G}, \tag{2.3}$$

with gauge coupling g and the covariant derivative

$$D_\mu(x) = \partial_\mu + iA_\mu(x) \tag{2.4}$$

and the field strength tensor

$$F_{\mu\nu}(x) = -i[D_\mu(x), D_\nu(x)] = \partial_\mu A_\nu(x) - \partial_\nu A_\mu(x) + i[A_\mu(x), A_\nu(x)]. \tag{2.5}$$

In the action (2.3) we have also introduced the mass matrix $M = \mathrm{diag}(m_1, \cdots, m_{N_f})$ and assumed that every fermion flavour couples to the gauge field in the same way. It will be convenient later on to consider the gauge part S_G containing only contributions from the gauge field and the fermionic part S_F of the action separately.

In the path integral formalism the expectation value of an operator $O(\psi, \bar{\psi}, A)$ is given by

$$\langle O \rangle = \frac{1}{\mathcal{Z}} \int \mathcal{D}\psi \mathcal{D}\bar{\psi} \mathcal{D}A \, O(\psi, \bar{\psi}, A) e^{i\mathcal{S}(\psi, \bar{\psi}, A)}, \qquad \mathcal{Z} = \int \mathcal{D}\psi \mathcal{D}\bar{\psi} \mathcal{D}A \, e^{i\mathcal{S}(\psi, \bar{\psi}, A)}. \tag{2.6}$$

A mathematical trick to render calculations involving the path integral more manageable is to perform a so-called Wick rotation. The Wick rotation amounts to substituting the time coordinate $x^0 = t$ with an imaginary time $t \to -it$. This substitution changes the Minkowski metric to an Euclidean metric. The Euclidean action $\mathcal{S}_E$ reads as

$$\mathcal{S}_E(\psi, \bar{\psi}, A) = \underbrace{\int d^4x \, \bar{\psi}(x) \left(\gamma_\mu^E D_\mu + M \right) \psi(x)}_{\mathcal{S}_F^E} + \underbrace{\int d^4x \frac{1}{2g^2} \operatorname{tr} \left(F(x)_{\mu\nu} F(x)_{\mu\nu} \right)}_{\mathcal{S}_G^E}, \tag{2.7}$$

where γ_μ^E are the Euclidean gamma matrices defined in Appendix A. After the Wick rotation Equation (2.6) becomes

$$\langle O \rangle_E = \frac{1}{\mathcal{Z}_E} \int \mathcal{D}\psi \mathcal{D}\bar{\psi} \mathcal{D}A \, O(\psi, A) e^{-\mathcal{S}_E(\psi, \bar{\psi}, A)}, \qquad \mathcal{Z}_E = \int \mathcal{D}\psi \mathcal{D}\bar{\psi} \mathcal{D}A \, e^{-\mathcal{S}_E(\psi, \bar{\psi}, A)}. \tag{2.8}$$

For many applications of interest the Euclidean action (2.7) turns out to be a real number and by employing a Wick rotation the strongly oscillating integrand $\exp(i\mathcal{S})$ is replaced by the exponentially decaying $\exp(-\mathcal{S}_E)$, greatly improving the convergence properties of the integral. For the rest of this chapter we assume that we are working in the Euclidean space and we suppress the index E.

Equation (2.8) bears a striking resemblance to the computation of expectation values in statistical mechanics. For a given inverse temperature $\beta = 1/T$ and Hamiltonian $\mathcal{H}$ the expectation value of the observable O reads as

$$\langle O \rangle = \frac{1}{\mathcal{Z}_P} \sum_s O(s) e^{-\beta \mathcal{H}(s)}, \qquad \mathcal{Z}_P = \sum_s e^{-\beta \mathcal{H}(s)}, \tag{2.9}$$

where the sum is to be understood as a sum (or integral for systems with continuous degrees of freedom) over all possible states s and $\mathcal{Z}_P$ is the partition function. This equivalence between quantum field theory and statistical mechanics is one of the foundations of lattice gauge theory.

2.1.1 *Chiral Symmetry*

The fermion action $\mathcal{S}_F$ as defined in Equation (2.7) has an interesting feature. For vanishing fermion masses $M = 0$ the action is symmetric under rotations in the flavour space. The corresponding symmetry group for N_f flavours is $U(N_f)$. Let t^a for $a \in \{1, 2, \cdots, N_f^2 - 1\}$ be the generators of $SU(N_f)$. Two types of symmetry transformations, which are commonly named after the transformation properties of the corresponding Noether currents, can be defined. For a real parameter ϑ the N_f^2 vector transformations are given by

$$\psi \to e^{i\vartheta t^a} \psi, \qquad \bar{\psi} \to \bar{\psi} e^{-i\vartheta t^a}, \tag{2.10}$$

$$\psi \to e^{i\vartheta \mathbb{1}} \psi, \qquad \bar{\psi} \to \bar{\psi} e^{-i\vartheta \mathbb{1}}, \tag{2.11}$$

and the associated Noether currents are $j_\mu^{V,t^a} = \bar{\psi}\gamma_\mu t^a \psi$ and $j_\mu^{V,\mathbb{1}} = \bar{\psi}\gamma_\mu\psi$. The axial vector or chiral transformations read as

$$\psi \to e^{i\vartheta\gamma_5 t^a}\psi, \qquad \bar{\psi} \to \bar{\psi}e^{i\vartheta\gamma_5 t^a}, \tag{2.12}$$

$$\psi \to e^{i\vartheta\gamma_5 \mathbb{1}}\psi, \qquad \bar{\psi} \to \bar{\psi}e^{i\vartheta\gamma_5 \mathbb{1}}, \tag{2.13}$$

and the axial Noether currents are given by $j_\mu^{A,t^a} = \bar{\psi}\gamma_\mu\gamma_5 t^a\psi$ and $j_\mu^{A,\mathbb{1}} = \bar{\psi}\gamma_\mu\gamma_5\psi$.

The chiral symmetry got its name because it allows us to decouple the right-handed and left-handed fermions in the mass-less action. This is most easily seen for the case $N_f = 1$, where we can define the operators

$$P_R = \frac{\mathbb{1}+\gamma_5}{2} \quad \text{and} \quad P_L = \frac{\mathbb{1}-\gamma_5}{2}. \tag{2.14}$$

A simple calculation shows that these operators have the properties

$$P_{R/L}^2 = P_{R/L}, \quad P_R P_L = P_L P_R = 0, \quad P_R + P_L = \mathbb{1}, \tag{2.15}$$

and can be interpreted as right-handed and left-handed projector, respectively. Using the projectors we can define right- and left-handed fields as

$$\psi_R = P_R\psi, \quad \psi_L = P_L\psi, \quad \bar{\psi}_R = \bar{\psi}P_L, \quad \bar{\psi}_L = \bar{\psi}P_R. \tag{2.16}$$

With the mass-less Dirac operator $D = \gamma_\mu D_\mu$ the fermion Lagrangian (density) is given by $\mathcal{L}_F = \bar{\psi}(x)D\psi(x)$. Inserting the identity in the form $\mathbb{1} = P_R + P_L$ on both sides of the Dirac operator and using the properties of the projectors (2.15) and the anti-commutator $\{\gamma_5, \gamma_\mu\} = 0$ yields:

$$\bar{\psi}(x)D\psi(x) = \bar{\psi}(x)(P_R+P_L)D(P_R+P_L)\psi(x) = \bar{\psi}_R(x)D\psi_R(x) + \bar{\psi}_L(x)D\psi_L(x). \tag{2.17}$$

Upon closer inspection of the chiral transformations it becomes evident that the chiral symmetry is equivalent to the statement that the mass-less Dirac operator anti-commutes with the matrix γ_5, i.e.:

$$\{D, \gamma_5\} = D\gamma_5 + \gamma_5 D = 0. \tag{2.18}$$

The fermionic mass term M commutes with γ_5 and therefore spoils the chiral symmetry. Note that for degenerate masses $M = \mathrm{diag}(m, \cdots, m)$ the vector symmetries are still intact. For finite, non-degenerate masses only the $U(1)$ symmetry (2.11) survives.

Combining the transformations (2.10) – (2.13) we find that the gauge action for N_f massless fermion flavours has the symmetry $SU(N_f)_V \times SU(N_f)_A \times U(1)_V \times U(1)_A$. This is a classical symmetry of the action and it does not necessarily persist in the quantised theory.

In interacting theories the formation of a so-called chiral condensate $\langle\bar{\psi}\psi\rangle$, which acts as a mass term, can spontaneously break the chiral symmetry. As we will see in Chapter 3, the $U_A(1)$ symmetry is explicitly broken by quantum fluctuations.

2.2 LATTICE GAUGE THEORY

The main idea behind lattice gauge theory is to discretise space-time on a lattice with a finite lattice spacing and a finite volume, while keeping the gauge symmetry of the

theory exact. Going from the continuum to the lattice formulation the continuous space-time variable $x \in \mathbb{R}^4$ is replaced by a discrete multi-index $n = a(n_1, n_2, n_3, n_4)$ where a is the lattice spacing and $n_i \in \{1, \cdots, L_i\}$ is the number of lattice sites in direction i.

Switching to the discrete lattice formulation significantly simplifies the calculation of the partition function $\mathcal{Z}_E$, because the path integral turns into a product of ordinary integrals:

$$\int D\psi \to \int \prod_n d\psi(n). \tag{2.19}$$

Evaluating the large but finite-dimensional integrals numerically makes it possible to compute the expectation values (2.8) on the lattice. In order to draw meaningful conclusions about the continuum theory from lattice results the discretised lattice action has to be constructed in such a way that the continuum action is recovered in the limit $a \to 0$ and $L_i \to \infty$.

As a first step towards the lattice discretisation of the continuum action (2.7) we consider the free fermionic action $S_F^0[\psi, \bar{\psi}] := S_F[\psi, \bar{\psi}, 0]$. The (symmetric) discretisation of the partial derivative is given by

$$\partial_\mu \psi = \frac{\psi(n + \hat{\mu}) - \psi(n - \hat{\mu})}{2a}, \tag{2.20}$$

where $\hat{\mu}$ is the unit vector in μ direction.

At first sight it seems to be straightforward to plug this expression into (2.7) to obtain the lattice action. There is however an issue with Equation (2.20). Let $G(n)$ be an element of the gauge group. Under a lattice gauge transformation the fields transform as

$$\psi(n) \to \psi'(n) = G(n)\psi(n) \qquad \text{and} \qquad \bar{\psi}(n) \to \bar{\psi}'(n) = \bar{\psi}(n)G^\dagger(n). \tag{2.21}$$

The problem is that terms involving the discretised derivative are obviously not gauge invariant, since

$$\bar{\psi}(n)'\psi(n + \hat{\mu})' = \bar{\psi}(n)G^\dagger(n)G(n + \hat{\mu})\psi(n + \hat{\mu}) \tag{2.22}$$

and in general $G^\dagger(n)G(n + \hat{\mu}) \neq \mathbb{1}$. A way out of this dilemma is to introduce an additional field $U_\mu(n)$ which transforms as

$$U_\mu(n) \to U'_\mu(n) = G(n)U_\mu(n)G^\dagger(n + \hat{\mu}). \tag{2.23}$$

The terms $U_\mu(n)$ can be visualised as living on the links connecting the lattice sites n and $n + \hat{\mu}$. For this reason they are commonly called link variables. The link variable $U_\mu(n)$ can be interpreted as the lattice parallel (gauge) transporter [21, 22] and in terms of the (lattice) gauge field $A_\mu(n)$ it is given by

$$U_\mu(n) = \exp(iaA_\mu(n)). \tag{2.24}$$

A gauge invariant discretised derivative can be defined with the help of the link variables $U_\mu(n)$, using terms of the form $\bar{\psi}(n)U_\mu(n)\psi(n + \hat{\mu})$, which are gauge invariant:

$$\begin{aligned} \bar{\psi}(n)'U'_\mu(n)\psi(n + \hat{\mu})' &= \bar{\psi}(n)'G(n)U_\mu(n)G^\dagger(n + \hat{\mu})\psi'(n + \hat{\mu}) \\ &= \bar{\psi}(n)U_\mu(n)\psi(n + \hat{\mu}). \end{aligned} \tag{2.25}$$

Using the link variables we can finally write down an expression for the gauge invariant lattice fermion action:

$$S_F(\psi,\bar{\psi},U) = a^4 \sum_n \bar{\psi}\left(\sum_{\mu=1}^{4}\gamma_\mu \frac{U_\mu(n)\psi(n+\hat{\mu}) - U_{-\mu}(n)\psi(n-\hat{\mu})}{2a} + M\psi(n)\right), \quad (2.26)$$

where the link variable in negative direction is defined as $U_{-\mu}(n) := U_\mu(n-\hat{\mu})^\dagger$. Equation (2.26) is called the naive fermion action and it can be shown that it reduces to the Euclidean continuum action (2.7) in the limit $a \to 0$ (for momenta $p_\mu a \ll 1$).

Having utilised the link variables in the construction of the fermionic action it is natural to also define the gauge action in terms of the fields $U_\mu(n)$. A gauge invariant action can be defined with the plaquette variables

$$U_{\mu\nu}(n) := U_\mu(n)U_\nu(n+\hat{\mu})U_{-\mu}(n+\hat{\mu}+\hat{\nu})U_{-\nu}(n+\hat{\nu}). \quad (2.27)$$

A plaquette is the shortest closed loop on the lattice and the plaquette variable $U_{\mu\nu}$ is the product of the link variables along the loop. Note that $U_{\mu\nu}(n)$ transforms as

$$U_{\mu\nu}(n) \to U'_{\mu\nu}(n) = G(n)U_{\mu\nu}(n)G(n)^\dagger \quad (2.28)$$

and is not gauge invariant. The trace of the plaquette variable, on the other hand, is gauge invariant:

$$\mathrm{tr}(U_{\mu\nu}(n)) \to \mathrm{tr}(U'_{\mu\nu}(n)) = \mathrm{tr}(G(n)U_{\mu\nu}(n)G(n)^\dagger) = \mathrm{tr}(U_{\mu\nu}(n)), \quad (2.29)$$

where we have used the invariance of the trace under cyclic permutations. The gauge invariant trace of the plaquette variable can be employed to define the lattice gauge action. An action with the correct continuum limit is given by

$$S_G(U) = \beta \sum_n \sum_{\nu<\mu}\left(1 - \frac{1}{d_G}\,\mathrm{Re}(\mathrm{tr}[U_{\mu\nu}(n)])\right), \quad (2.30)$$

where $\beta = 2d_G/g^2$ and d_G is the dimension of the representation of the gauge group.

2.2.1 *Fermion Doubling and Wilson Fermions*

Even though the naive fermion action (2.26) is gauge invariant, there is still a subtle problem with it. To get to the bottom of the issue it is convenient to define the lattice Dirac operator for a single fermion flavour with mass $\bar{m}$ as

$$D(n,m) := \sum_{\mu=1}^{4}\gamma_\mu \frac{U_\mu(n)\delta_{n+\hat{\mu},m} - U_{-\mu}(n)\delta_{n-\hat{\mu},m}}{2a} + \bar{m}\delta_{n,m}. \quad (2.31)$$

The corresponding naive fermion action can be written in the compact form

$$S_F(\psi,\bar{\psi},U) = a^4 \sum_{n,m}\bar{\psi}(n)D(n,m)\psi(m). \quad (2.32)$$

For free lattice fermions ($U_\mu(n) = \mathbb{1}$) the lattice Fourier transform can be computed analytically and the Dirac operator in momentum space is given by

$$\tilde{D}(p,q) = \delta(p-q)\tilde{D}(p) \quad \text{with} \quad \tilde{D}(p) = \bar{m}\mathbb{1} + \frac{i}{a}\sum_{\mu=1}^{4}\gamma_\mu \sin(p_\mu a). \quad (2.33)$$

This operator is diagonal and the momentum space fermion propagator can be calculated by inverting $\tilde{D}(p)$:

$$\tilde{D}^{-1}(p) = \frac{\bar{m}\mathbb{1} - ia^{-1}\sum_{\mu=1}^{4}\gamma_\mu \sin(p_\mu a)}{\bar{m}^2 + a^{-2}\sum_{\mu=1}^{4}\sin^2(p_\mu a)}. \tag{2.34}$$

In the limit $\bar{m} \to 0$ this expression becomes

$$\lim_{\bar{m}\to 0}\tilde{D}^{-1}(p) = \frac{-ia^{-1}\sum_{\mu=1}^{4}\gamma_\mu \sin(p_\mu a)}{a^{-2}\sum_{\mu=1}^{4}\sin^2(p_\mu a)}. \tag{2.35}$$

A straightforward calculation shows that it has the correct continuum limit:

$$\lim_{a\to 0}\lim_{\bar{m}\to 0}\tilde{D}^{-1}(p) = \frac{-i\sum_{\mu=1}^{4}\gamma_\mu p_\mu}{p^2}. \tag{2.36}$$

In the continuum theory the momentum space propagator of a free fermion has a single pole at $p_\mu = (0,0,0,0)$, corresponding to a single mass-less fermion. The problem with the naive fermion action is that it gives rise to a propagator which has additional poles whenever $\sum_\mu \sin^2(p_\mu a) = 0$. For the lattice momenta $p_\mu \in (-\pi/a, \pi/a]$ this sum vanishes if every entry of the 4-momentum is either 0 or π/a. Hence the naive lattice propagator has $2^4 = 16$ poles. The additional unpyhsical poles at $p_\mu \neq (0,0,0,0)$ are commonly referred to as doublers.

In summary the issue is that we set out to define a lattice theory with only one fermion flavour but ended up with a theory describing 16. One way to solve the problem, originally suggested by Wilson, is to add the following term to the momentum space propagator:

$$\delta\tilde{D}_W(p) := \mathbb{1}\frac{2r}{a}\sum_{\mu=1}^{4}\sin^2\left(\frac{p_\mu a}{2}\right), \tag{2.37}$$

where $r \in (0,1]$ is a free parameter and is often set to 1 in practice. The so-called Wilson term (2.37) vanishes at the physical pole and has the value $2r\lambda/a$ for the doublers, with λ being the number of non-zero components of p_μ. With the addition of the Wilson term the mass of the doublers is given by

$$\bar{m} + \frac{2r\lambda}{a}. \tag{2.38}$$

In the continuum limit $a \to 0$ the doublers become infinitely heavy and effectively decouple from the theory.

After an inverse Fourier transform we find that the Wilson term in position space reads as

$$\delta D_W(n,m) = -a\sum_{\mu=1}^{4}\frac{U_\mu(n)\delta_{n+\hat{\mu},m} - 2\delta_{n,m} + U_{-\mu}(n)\delta_{n-\hat{\mu},m}}{2a^2}. \tag{2.39}$$

With the Wilson–Dirac operator $D_W = D + \delta D_W$ a doubler free lattice fermion action can be defined:

$$S_F^W(\psi, \bar{\psi}, U) = a^4 \sum_{n,m} \bar{\psi}(n) D_W(n, m) \psi(m). \tag{2.40}$$

An explicit expression for the Wilson–Dirac operator in lattice QCD is given in Appendix D.1.

We emphasise that the lattice gauge action is not uniquely defined and different discretisation schemes than the ones described above are possible.

2.2.2 *Numerical Evaluation of Lattice Expectation Values*

On the lattice the fermion fields are Grassman numbers and the fermionic action is bilinear in the fermion fields. It is therefore possible to evaluate the fermionic part of the expectation value $O(\psi, \bar{\psi}, U)$ analytically and with the definitions

$$\begin{aligned} \langle O \rangle_F &:= \frac{1}{Z_F} \int \prod_{n,m} d\psi(m) d\bar{\psi}(n)\, O(\psi, \bar{\psi}, U) e^{\bar{\psi}(n) D(n,m) \psi(m)}, \\ Z_F &:= \int \prod_{n,m} d\psi(m) d\bar{\psi}(n)\, e^{\bar{\psi}(n) D(n,m) \psi(m)} = \det(D), \end{aligned} \tag{2.41}$$

the expectation value of an observable $O(\psi, \bar{\psi}, U)$ is given by

$$\begin{aligned} \left\langle O(\psi, \bar{\psi}, U) \right\rangle &= \frac{1}{Z} \int \prod_{n,\mu} dU_\mu(n)\, e^{-S_G(U)} \det(D) \langle O \rangle_F \\ Z &:= \int \prod_{n,\mu} dU_\mu(n)\, e^{-S_G(U)} \det(D). \end{aligned} \tag{2.42}$$

The term $\det(D)$ is commonly referred to as fermion determinant. We have suppressed the dependence on the link variables in Equation (2.41), but it is important to keep in mind that the Dirac operator $D = D(U)$ and $\langle O \rangle_F = \langle O \rangle_F (U)$ still depend on the link variables.

Even after integrating out the fermionic degrees of freedom we are still left with a high-dimensional integral over the link variables. Equation (2.42) can not be tackled with the same numerical integration methods as lower dimensional problems. At this point the similarity between the lattice path integral and the partition function (2.9) comes into play: If the term $e^{-S_E} = e^{-S_G} \det(D)$ is positive it can be interpreted as a statistical weight and the path integral can be evaluated using Monte Carlo integration algorithms with importance sampling.

Obviously the exponent of the gauge action (2.30) is positive. The fermion determinant, on the other hand, is not necessarily positive and can even become complex. For γ_5-Hermitian[1] Dirac operators it can be shown that the determinant is real and by using an even number of mass degenerate fermions on can ensure its non-negativity. Not all Dirac operators of interest have this property and in particular the introduction of a finite chemical potential or vacuum angle gives rise to a complex fermion determinant. This is the infamous sign problem or complex action problem. So far a general solution

to the sign problem is not known and it remains a major impediment to lattice simulations of quantum field theories. For recent advances see the review [23] and references therein.

The idea of importance sampling is to approximate the lattice path integral by an average over N samples

$$\left\langle O(\psi,\bar{\psi},U)\right\rangle \approx \frac{1}{N}\sum_{n=1}^{N} O(\mathcal{C}_n), \tag{2.43}$$

where the field configurations $\mathcal{C}_n = \mathcal{C}_n(\psi,\bar{\psi},U)$ are sampled with a probability proportional to their weight factor $e^{-S_G(\mathcal{C}_n)}\det(D(\mathcal{C}_n))$. A set of such configurations can be generated with Markov chain algorithms. For implementation details we refer to the textbooks [21, 22].

In a typical Markov process a large amount of the computer time is spent for the computation of weight factors. In four dimensions the lattice Dirac operator is given by a $(4d_GV)$-dimensional matrix, where V is the number of lattice sites. Even for relatively small lattice sizes it is numerically very costly to calculate the fermion determinant. Many practical simulations therefore apply the so-called quenched approximation, where the value of the fermion determinant is set to one. It can be shown that this amounts to neglecting the contributions from fermionic vacuum loops.

2.2.3 *Finite Temperature and Chemical Potential*

In the continuum theory finite temperature is introduced by performing a Wick rotation, identifying the temperature with the imaginary time extent, compactifying the time direction and choosing the appropriate (anti-)periodic boundary conditions in time for the (fermionic) bosonic fields. In lattice simulations it is customary to choose n_4 as the time index and the total extent of the lattice in time direction is given by $L_T = L_4$. The physical time extent is then aL_T and in analogy to the continuum case we identify the inverse temperature β with

$$\beta = \frac{1}{T} = aL_T. \tag{2.44}$$

Working at finite fermion chemical potential on the lattice turns out to be more of a challenge. The chemical potential couples to the conserved fermion number, which is simply the charge related to the conserved current $\bar{\psi}\gamma_4\psi$ in the continuum theory. Consequently, in the continuum theory a finite chemical potential μ can be implemented by adding the term $\mu\bar{\psi}\gamma_4\psi$ to the action, which amounts to the replacement $\partial_4 \to \partial_4 + \mu$.

Naively adopting the same strategy to implement a finite chemical potential on the lattice gives rise to terms that diverge in the continuum limit [24, 25]. Note that in the continuum the chemical potential enters the action in the same way as the 4-component of a gauge field. On the lattice this is no longer true which is, in essence, the source of the problem [24]. One correct way to introduce a lattice chemical potential is to replace the link variables in 4-direction by [24, 26]

$$\gamma_4 U_4(n) \to \gamma_4 e^{a\mu} U_4(n) \quad , \quad -\gamma_4 U_4^\dagger(n-\hat{4}) \to -\gamma_4 e^{-a\mu} U_4^\dagger(n-\hat{4}). \tag{2.45}$$

1 A Dirac operator D is said to be γ_5-Hermitian if $\gamma_5 D\gamma_5 = D^\dagger$ or equivalently $(\gamma_5 D)^\dagger = \gamma_5 D$.

We have mentioned above that lattice Dirac operators with a finite chemical potential are not γ_5-Hermitian. This can be seen easily by multiplying (2.45) with γ_5 from both sides and taking the Hermitian conjugate. We find that under these operations $\gamma_4 e^{a\mu} U_4(n) \to -\gamma_4 e^{a\mu} U_4^\dagger(n)$ and $-\gamma_4 e^{-a\mu} U_4^\dagger(n-\hat{4}) \to \gamma_4 e^{-a\mu} U_4(n-\hat{4})$. In the fermion action we sum over all lattice sites. A simple renaming of the summation indices reveals that an originally γ_5-Hermitian Dirac operator now obeys the equation

$$\gamma_5 D(\mu)\gamma_5 = D^\dagger(-\mu). \tag{2.46}$$

Therefore, a finite chemical potential in general leads to a sign problem.

2.2.4 *Chiral Symmetry on the Lattice*

The naive fermionic action (2.26) is chirally symmetric for vanishing fermion masses. This property is lost when we add the Wilson term to get rid of the doublers. The Wilson term acts like an momentum dependent mass and explicitly breaks the chiral symmetry even for $M = 0$.

Naively one would expect that it should be possible to get rid of the doublers without breaking chiral symmetry, probably by adding a more complicated function of p_μ to $\tilde{D}(p)$. There is however a famous no-go theorem by Nielsen and Ninomiya [27–29] (see also [30, 31]) that states that it is not possible to construct a lattice Dirac operator with all of the following properties:

1. D is local
2. D has the correct continuum limit
3. D is free of doublers
4. $\gamma_5 D + D\gamma_5 = 0$

In Section 2.1.1 we have argued that a Dirac operator has to have property 4 in order to be invariant under chiral transformations. Thus the Nielsen–Ninomiya theorem seems to forbid a lattice Dirac operator which is simultaneously local, chiral and free of doublers.

However, a loophole was discovered by Ginsparg and Wilson in [32], where they proposed to replace the continuum condition (2.18) by

$$D\gamma_5 + \gamma_5 D = aD\gamma_5 D. \tag{2.47}$$

The Ginsparg–Wilson equation reduces to (2.18) in the continuum limit and makes it possible to implement a lattice version of chiral symmetry [33]. If the Dirac operator D obeys Equation (2.47) a lattice chiral transformation can be defined by

$$\psi \to e^{i\vartheta\gamma_5(\mathbb{1}-\frac{a}{2}D)}\psi, \qquad \bar{\psi} \to \bar{\psi} e^{i\vartheta(\mathbb{1}-\frac{a}{2}D)\gamma_5}, \tag{2.48}$$

which reduces to (2.13)[2] in the limit $a \to 0$. A few lines of algebra show that the lattice action $\bar{\psi}D\psi$ is indeed invariant under (2.48).

The definition of the left- and right-handed field components also has to be modified. Let us again consider a theory with only one fermion flavour. We define the projectors

$$\hat{P}_R = \frac{\mathbb{1}+\hat{\gamma}_5}{2} \quad , \quad \hat{P}_L = \frac{\mathbb{1}-\hat{\gamma}_5}{2} \quad \text{with} \quad \hat{\gamma}_5 = \gamma_5(\mathbb{1} - aD). \tag{2.49}$$

2 The lattice version of (2.12) is defined analogously.

It is easy to see that these projectors have properties analogous to (2.15) and from the Ginsparg–Wilson equation follows that $D\hat{P}_R = P_L D$ and $D\hat{P}_L = P_R D$. With the definitions

$$\psi_R = \hat{P}_R \psi, \quad \psi_L = \hat{P}_L \psi, \quad \bar{\psi}_R = \bar{\psi} P_L, \quad \bar{\psi}_L = \bar{\psi} P_R, \tag{2.50}$$

the fermionic action decouples into a left- and right-handed part, in analogy to (2.17). Note that two different types of projectors are used to define the chiral field components on the lattice.

As in the continuum theory, the addition of a mass term $\bar{\psi}\bar{m}\psi$ to the action should break the chiral symmetry by mixing field components with different chirality:

$$\bar{\psi}\bar{m}\psi = \bar{m}\left(\bar{\psi}_R\psi_L + \bar{\psi}_L\psi_R\right) = \bar{m}\bar{\psi}\left(P_L\hat{P}_L + P_R\hat{P}_R\right)\psi = \bar{m}\bar{\psi}\left(\mathbb{1} - \frac{a}{2}D\right)\psi. \tag{2.51}$$

A Dirac operator describing massive Ginsparg–Wilson fermions is therefore given by

$$D_{\bar{m}} = D + \bar{m}\left(\mathbb{1} - \frac{a}{2}D\right). \tag{2.52}$$

The zero modes of a Dirac operator obeying the Ginsparg–Wilson equation have a very interesting feature. Given that $\gamma_5 D|\psi\rangle = 0$ Equation (2.47) implies $D\gamma_5|\psi\rangle = 0$, i.e. the Dirac operator commutes with γ_5 on its kernel. We can therefore find a basis in which the zero modes of D are also eigenmodes of γ_5. The operator γ_5 is Hermitian and $\gamma_5^2 = \mathbb{1}$, so its eigen values can only be ± 1 and $\gamma_5|\psi\rangle = \pm|\psi\rangle$. A comparison with the projectors (2.49) shows that the zero modes of D therefore have a definite handedness.

This makes it possible to formulate an equivalent to the Atiyah–Singer index theorem for mass-less Ginsparg–Wilson fermions. The index theorem connects the topological charge Q of a gauge field configuration to the number of left- and right-handed zero modes of the Dirac operator. For a Dirac operator respecting Equation (2.47) the topological charge is given by $Q = \frac{a}{2}\operatorname{tr}(\gamma_5 D)$ (cf. [34–37]) and the index theorem takes the form

$$Q = \frac{a}{2}\operatorname{tr}(\gamma_5 D) = n_- - n_+, \tag{2.53}$$

where n_- and n_+ are counting the left- and right-handed zero modes.

2.2.5 *Overlap Fermions*

After the ground-breaking paper [32] it took over a decade before the first solutions to the Ginsparg–Wilson equation were found. Nowadays several solutions and approximate solutions are known and lattice simulations with Ginsparg–Wilson fermions have become routine. In this work we will use the so-called overlap Dirac operator as defined in [38]. The overlap operator is a solution to the Ginsparg–Wilson Equation [39] and can be written as

$$D_{ov} = \frac{1}{a}\left(\mathbb{1} + \gamma_5 \operatorname{sgn}(H)\right), \tag{2.54}$$

where the kernel is given by $H = \gamma_5 D$ and sgn is the matrix sign function. We will use the Wilson–Dirac operator D_W (see Appendix D) to construct the kernel, but in

principle any other doubler-free Dirac operator with the correct continuum limit can be taken instead.

A straight forward calculation shows that the overlap operator indeed obeys Equation (2.47):

$$\begin{aligned} aD_{ov}\gamma_5 D_{ov} &= \frac{1}{a}\big(\mathbb{1}+\gamma_5\,\mathrm{sgn}(H)\big)\gamma_5\big(\mathbb{1}+\gamma_5\,\mathrm{sgn}(H)\big) \\ &= \frac{1}{a}\big(\gamma_5+\gamma_5\,\mathrm{sgn}(H)\gamma_5+\mathrm{sgn}(H)+\gamma_5\,\mathrm{sgn}^2(H)\big) \\ &= \frac{1}{a}\big(\mathbb{1}+\gamma_5\,\mathrm{sgn}(H)\big)\gamma_5+\frac{1}{a}\gamma_5\big(\mathbb{1}+\gamma_5\,\mathrm{sgn}(H)\big) \\ &= D_{ov}\gamma_5+\gamma_5 D_{ov}, \end{aligned} \tag{2.55}$$

where we have used the identity $\mathrm{sgn}^2(H) = \mathbb{1}$. Keep in mind that we have not used any of the properties of the kernel H in this derivation. In the overlap operator the sign function ensures that the Ginsparg–Wilson relation is fulfilled, independent from the form of H. The role of the kernel is solely to provide the proper continuum limit.

It is possible to generalise the definition of the overlap operator to finite chemical potential [40]

$$D_{ov}(\mu) = \frac{1}{a}\big(\mathbb{1}+\gamma_5\,\mathrm{sgn}(H(\mu))\big), \tag{2.56}$$

with the new kernel given by $H(\mu) = \gamma_5 D_W(\mu)$. As we have seen above the operator $D_{ov}(\mu)$ still obeys the Ginsparg–Wilson equation and thus makes it possible to simulate chiral fermions at finite density on the lattice.

The evaluation of the overlap operator is numerically very expensive, because it requires the calculation of the matrix sign function. Moreover, at finite chemical potential $D_{ov}(\mu)$ is not γ_5-Hermitian and calculations with dynamical overlap fermions at finite density suffer from the sign problem. For these two reasons, we will work in the quenched approximation in this thesis. We postpone a detailed discussion of the numerical aspects of overlap fermions at finite chemical potential μ to Chapter 7.

3

ANOMALOUS TRANSPORT

In this chapter we briefly discuss the chiral anomaly, which is the origin of all anomalous transport phenomena. Moreover, we introduce the anomalous transport effects that are studied in this thesis, namely the Chiral Magnetic Effect (CME) [7, 41] and the Chiral Separation Effect (CSE) [8, 9]. The description is mainly qualitative and for a more detailed discussion we refer to the original papers on the subject and the recent reviews [42, 43].

3.1 THE CHIRAL ANOMALY

The chiral anomaly was first encountered in the context of high-energy physics. Originally it was believed that the classical $U_A(1)$ symmetry of the fermionic action is also a symmetry of the quantised theory. It became soon apparent, however, that the existence of such a symmetry leads to a theoretical result for the decay width of $\pi^0 \to 2\gamma$ which is at odds with experimental findings.

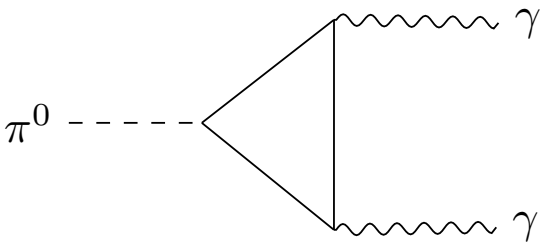

Figure 3.1: The triangle diagram for the decay $\pi \to \gamma\gamma$.

An explanation for this discrepancy was eventually found by Adler [44] and Bell and Jackiw [45]: The triangle diagram depicted schematically in Figure 3.1 is divergent and has to be regularised. A careful analysis reveals that any regularisation breaks the chiral $U_A(1)$ symmetry[1]. Fujikawa later showed that in the path integral formalism the anomaly emerges because the integral measure is not invariant under the chiral transformation [46].

1 Strictly speaking one finds that it is not possible to simultaneously preserve both the $U_A(1)$ and the $U_V(1)$ symmetry.

Because of the explicit breaking of the $U_A(1)$ symmetry by quantum fluctuations the axial current is no longer conserved. For fermions coupling to electromagnetic fields the divergence of the axial current is given by

$$\partial^\mu j^A_\mu = \frac{\mathcal{N}}{(4\pi)^2}\tilde{F}_{\mu\nu}F^{\mu\nu} = \frac{\mathcal{N}}{2\pi^2}\vec{E}\cdot\vec{B}, \tag{3.1}$$

where $\tilde{F}_{\mu\nu} = \epsilon_{\mu\nu\sigma\rho}F^{\sigma\rho}$ is the dual field strength tensor and $\mathcal{N}$ is a number depending on the number of fermion flavours and the charges of the fermions. The anomaly is not subject to perturbative corrections [47] and therefore the relation (3.1) is exact.

3.2 ANOMALOUS TRANSPORT PHENOMENA

For simplicity we discuss the anomalous transport effects for case of a single fermion flavour with electric charge $q = 1$ and set $\mathcal{N} = 1$ in the following. The introduction of more fermion species and different charges is straightforward and in later chapters we simply use the appropriate generalisations of the equations in this section.

In this work we consider the CME and the CSE, but we note that many other anomalous transport effects are known [43].

3.2.1 *The Chiral Magnetic Effect*

The CME is the induction of an electric (vector) current parallel to an external magnetic field B in a medium with an imbalance between left- and right-handed chiral fermions:

$$j_i = \sigma_{CME}B_i. \tag{3.2}$$

It is characterised by the transport coefficient σ_{CME}, the so-called chiral magnetic conductivity. The numerical value of σ_{CME} is related to the anomaly coefficient and is given by

$$\sigma_{CME} = \frac{\mu_A}{2\pi^2}, \tag{3.3}$$

where μ_A is the chiral chemical potential which parametrises the imbalance between right- and left-handed particles. Derivations of this value with different methods and in various setups can be found in the literature, see for example [42, 43] and references therein. Instead of reproducing the calculations from these works, we follow [43] and provide an intuitive, qualitative description of the CME.

To this end we consider the schematic depiction of the CME given in Figure 3.2. A (sufficiently strong) magnetic field leads to a magnetisation and the majority of the fermion spins $\vec{s}$ (dashed arrows) point in the same direction as $\vec{B}$, which implies $\langle\vec{s}\rangle \propto \vec{B}$. For chiral fermions the direction of the momentum $\vec{p}$ (full arrows) is related to the spin, $\vec{p}$ is parallel to $\vec{s}$ for right-handed fermions and parallel to $(-\vec{s})$ for left-handed fermions. At $\mu_A > 0$ the average momentum $\langle\vec{p}\rangle$ vanishes, but for $\mu_A > 0$ there will be a net correlation between average spin and momentum, i.e. $\langle\vec{p}\rangle \propto \mu_A\langle\vec{s}\rangle$. Therefore, $\langle\vec{p}\rangle \propto \mu_A\vec{B}$, which gives rise to a vector current $\vec{j} \propto \langle\vec{p}\rangle \propto \mu_A\vec{B}$. The picture for anti-fermions is essentially the same and it is easy to see that they contribute an equal amount to the total current as the fermions.

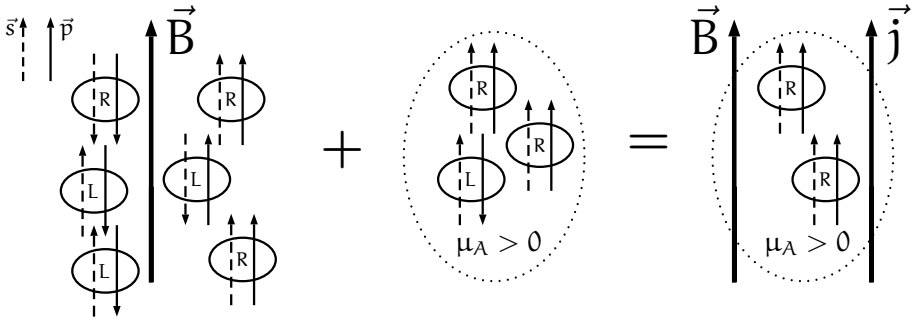

Figure 3.2: Illustration of the Chiral Magnetic Effect. The anti-particles are not shown in the graphic. See text for details.

From the simple argumentation above we can not infer the value of σ_{CME}, but it shows how a current parallel to a magnetic field can emerge.

An interesting observation about the chiral magnetic conductivity (3.2) is that it is time-reversal ($\mathcal{T}$) invariant. A $\mathcal{T}$-even conductivity gives rise to a non-dissipative current [48].

3.2.2 *The Chiral Separation Effect*

The CSE is the complimentary transport phenomenon to the CME, in the sense that it describes the axial current parallel to an external magnetic field in chiral media with a finite (vector) chemical potential μ:

$$j_i^A = \sigma_{CSE} B_i, \tag{3.4}$$

with the chiral separation conductivity σ_{CSE} given by

$$\sigma_{CSE} = \frac{\mu}{2\pi^2}. \tag{3.5}$$

The value of σ_{CSE} is also related to the anomaly. For a derivation of this value we again refer to the literature.

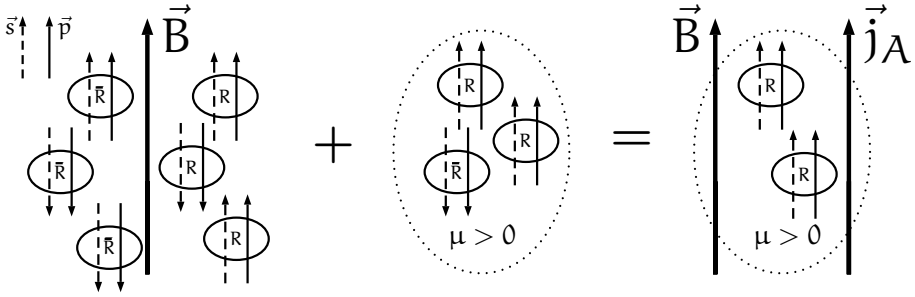

Figure 3.3: Illustration of the Chiral Separation Effect. For simplicity only right-handed particles and anti-particles are shown. See text for details.

We follow [43] and consider Figure 3.3 to gain a qualitative understanding of the CSE. The magnetic field gives rise to a spin polarisation. The momenta $\vec{p}$ (full arrows) of right-handed fermions (and anti-fermions) are parallel to their spin $\vec{s}$ (dashed arrows). Because of their opposite charge fermions and anti-fermions will have opposite average

momentum, $\left\langle \vec{p}_{R/\bar{R}} \right\rangle \propto \pm\vec{B}$, and the total axial current is zero. If $\mu > 0$ there are more fermions than anti-fermions and there is a net current of right-handed fermions $\vec{j}_R \propto \mu\vec{B}$. Analogously the left-handed particles and anti-particles form the current $j_L \propto -\mu\vec{B}$ and together they constitute the axial current $\vec{j}^A = \vec{j}_R - \vec{j}_L \propto \mu\vec{B}$.

If we express the $\vec{j}_{R/L}$ in terms of $\vec{j}$ and $\vec{j}^A$ it becomes evident that the CME and the CSE have the same origin:

$$\vec{j}_{R/L} = \frac{\vec{j} \pm \vec{j}^A}{2} = \pm\sigma_{R/L}\vec{B}, \tag{3.6}$$

where $\sigma_{R/L} = \frac{\mu_{R/L}}{4\pi^2}$ with the chemical potential for left- and right-handed particles given by $\mu_{R/L} = \frac{\mu \pm \mu_A}{2}$. Equation (3.6) is simply the CME relation (3.2) for purely right-handed and purely left-handed fermions. It is therefore not surprising that the same factor $\frac{1}{2\pi^2}$ appears in the transport coefficients (3.3) and (3.5).

3.2.3 *Anomalous Transport Coefficients in Strongly Interacting Theories*

The CME and the CSE are closely related to the chiral anomaly and it is possible to derive non-renormalisation statements for the values of the transport coefficients σ_{CME} and σ_{CSE}. For this reason (3.3) and (3.5) are often called the "universal" values of the transport coefficients.

It is, however, important to keep in mind that these non-renormalisation statements are generally derived in a context where the coupling of the dynamical gauge fields to the anomalous currents is neglected [16, 17]. Moreover, they are often based on additional non-trivial assumptions, like a finite static correlation length and the applicability of a hydrodynamic approximation [16, 49–51].

If dynamic (electromagnetic) gauge fields are taken into account, the correlators of the electric current $\vec{j}$ are subject to perturbative QED corrections. It has been shown that this can lead to a renormalisation of the conductivities σ_{CME} and σ_{CSE} [15–17].

Additionally, in systems with strongly interacting fermions the chiral symmetry can be spontaneously broken by the formation of a chiral condensate. The spontaneous breaking of chiral symmetry is necessarily accompanied by the appearance of massless Goldstone modes. The assumptions that underlie the hydrodynamic approximation are then no longer valid. Moreover, the chiral condensate acts like an effective mass term which mixes particles with left- and right-handed chirality. The concept of a Fermi surface at fixed chiral chemical potential μ_A becomes ill defined in this case [13].

It is therefore reasonable to expect that the anomalous transport coefficients can differ from the universal values in strongly interacting theories. In the following parts of this thesis we further investigate this possibility.

Part II

THE CHIRAL MAGNETIC EFFECT IN WEYL SEMIMETALS

This part of the thesis is mainly concerned with the Chiral Magnetic Effect in Weyl semimetals. Preliminary results for the study of the mean-field phase diagram of the model considered in this part were published in [52]. The main results were derived during the work on the paper [53] and finite-size effects in Weyl semimetal slabs were investigated in [54].

4

MODELLING A WEYL SEMIMETAL

4.1 MOTIVATION AND INTRODUCTION TO WEYL SEMIMETALS

From the viewpoint of electronic band theory all solids can be classified as either metals, semimetals, insulators or semiconductors. In a metal the valence and conduction bands touch at the Fermi level E_f, whereas in semiconductors and insulators the Fermi level lies in a band gap. Semimetals are similar to metals in the sense that there is no gap between the valence and conducting band, but in a semimetal the density of states around the Fermi level is negligible. Figure 4.1 shows a simplified sketch of the band structure in metals, semimetals and insulators.

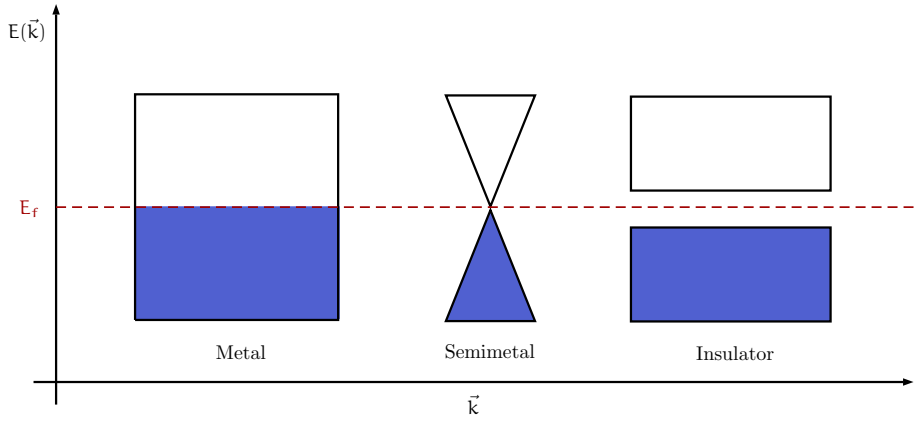

Figure 4.1: Qualitative sketch of the band structure in different types of solids.

An interesting type of semimetals are the Dirac semimetals, see for example the recent reviews [55, 56]. In a Dirac semimetal the valence and conduction bands touch only at discrete points, so-called Dirac points, in the Brillouin zone. Around the Dirac points the dispersion relation is linear in all directions. Thus Dirac semimetals harbour low-energy excitations that behave like massless Dirac fermions.

Each Dirac point can be viewed as consisting of two degenerate Weyl points. By breaking either the time-reversal ($\mathcal{T}$) or the parity ($\mathcal{P}$) symmetry the Weyl points are no longer degenerate and the Dirac semimetal turns into a different topological material, dubbed WSM [57], with Weyl fermions as low-energy excitations.

If the $\mathcal{T}$-symmetry is broken the Weyl nodes are separated in momentum space and if $\mathcal{P}$-symmetry is broken they are shifted in different directions in the energy [58]. A way to break $\mathcal{T}$-symmetry is to dope the material with magnetic impurities and $\mathcal{P}$-symmetry can be broken by introducing a chiral chemical potential.

The Weyl points are (anti-)monopoles of Berry curvature and are topologically protected. The only way to destroy Weyl points is by bringing a monopole and an anti-monopole together.

Another way to understand the stability of the Weyl nodes against perturbations is to look at the Hamiltonian that describes the low energy excitations. This Hamiltonian can be brought in the form of a Weyl Hamiltonian and, up to an irrelevant additive constant and a possible shift in the lattice momentum, reads as

$$H = v_F \vec{\sigma} \cdot \vec{k}, \tag{4.1}$$

where the Fermi velocity v_F plays the role of the speed of light. In three dimensions there are only three Pauli matrices σ_i. Any perturbation is therefore proportional to one of the matrices σ_i and can only shift the Weyl node in momentum space, but can not open up a gap.

The robustness against perturbations makes WSMs ideal candidates to realise Weyl fermions in an experiment and to study anomalous transport properties of chiral fermions in the laboratory with a relatively simple experimental setup, see for example the recent studies [5, 6, 59–62].

A signature of the CME in solids where Weyl modes of different chirality have different energies (i.e. with a finite chiral chemical potential) is the negative magnetoresistivity in the direction of an applied external magnetic field [63]. Observations of a negative magnetoresistivity have recently been reported for the semimetals $Bi_{1-x}Sb_x$ [5], $ZrTe_5$[6], Na_3Bi [60] and TaAs [61]. Numerically a similar dependence of the electric conductivity on the magnetic field was found in $SU(2)$ lattice gauge theory [64] and in holographic model calculations [65, 66].

The well known expression for σ_{CME} for free Dirac fermions in the continuum is [41]

$$\sigma_{CME} = \frac{N_f \mu_A}{2\pi^2}, \tag{4.2}$$

where N_f is the number of Dirac cones in the spectrum and μ_A is the chiral chemical potential. The chiral chemical potential is simply a convenient way to parametrise the difference in the density of left- and right-handed fermions. Strictly speaking because of the chiral anomaly the chiral charge is not conserved and μ_A is thus not a chemical potential in the usual sense. We will discuss this point in more detail later on.

In an experimental setup with parallel electric and magnetic fields a chirality imbalance (and therefore a chiral chemical potential) is created by the axial anomaly. Applying a simple relaxation time approximation gives the following relation for the chiral chemical potential [6]

$$\mu_A = \frac{3v_F^3}{4\pi^2} \frac{\vec{E} \cdot \vec{B}}{T^2 + \frac{\mu^2}{\pi^2}} \tau, \tag{4.3}$$

with the chemical potential μ, the chirality-changing scattering time τ and the temperature T. Combining Equations (3.2), (4.2) and (4.3) it is straight forward to see how the quadratic dependency of the conductivity on the magnetic field ensues.

The expression (4.2) is frequently quoted as the universal value for the chiral magnetic conductivity and was reproduced in several independent model calculations of $\mathcal{P}$-breaking WSMs [4, 67–70]. It was shown, however, that for lattice models the

value (4.2) is only valid in the limit of a spatially homogeneous magnetic field that slowly varies in time [71]. For a static homogeneous magnetic field σ_{CME} vanishes [58]. Using general gauge invariance arguments it can even be shown that in the thermodynamic limit in the ground state the current has to vanish and consequently $\sigma_{\mathrm{CME}} = 0$ [72].

If the static external magnetic field is not homogeneous, however, the chiral magnetic conductivity becomes a non-trivial function of the wave vector $\vec{k}$ of the external field. Furthermore, as long as chiral symmetry is not spontaneously broken, it is possible to relate the asymptotic value of $\sigma_{\mathrm{CME}}(\vec{k})$ for large $\vec{k}$ to the anomaly coefficient [13]. The relation between $\sigma_{\mathrm{CME}}(\vec{k})$ and the axial anomaly is highly non-trivial, but for large $\vec{k}$ the conductivity approaches *minus* the universal value (4.2). The reason for the different results for σ_{CME} lies in the use of different regularisation schemes. If the regularisation conserves the vector current σ_{CME} vanishes for static homogeneous magnetic fields [13, 73], in accordance with the results from [72]. Note that in both regularisations it is possible to relate σ_{CME} to the anomaly coefficient.

In most calculations of the chiral magnetic conductivity the fermion interactions have been neglected. On the one hand this approach is justified by the results of studies within the hydrodynamic, Fermi liquid and kinetic theory approximations, where the anomalous transport coefficients have universal values and do not depend on the inter--fermion interactions [49–51, 74–76]. On the other hand, as discussed in Chapter 3, there are two settings where inter-fermion interactions can lead to corrections to the anomalous transport coefficients: If chiral symmetry is spontaneously broken or if the electric current is coupled to a dynamical gauge field.

As it turns out, both of these scenarios can be relevant for realistic Weyl semimetals. The Fermi velocity v_{F} in Dirac and Weyl semimetals typically lies between $v_{\mathrm{F}} \sim 10^{-3}$ and $v_{\mathrm{F}} \sim 10^{-2}$ (see e.g. [5, 6, 77]) and the effective coupling constant $\alpha_{\mathrm{eff}} = \alpha/v_{\mathrm{F}} \sim \frac{1}{137 v_{\mathrm{F}}}$ is of order one. Hence the electrons in a Weyl semimetal are strongly coupled and can become unstable towards spontaneous chiral symmetry breaking. Moreover, the inter-electron interactions in a solid are mediated by dynamical gauge fields (photons) and perturbative corrections to σ_{CME} are possible even in the absence of spontaneous chiral symmetry breaking .

In view of the potential effects on the chiral magnetic conductivity it is interesting to study a Weyl semimetal with strongly interacting fermions. An important question in this context is whether inter-electron interactions can lead to significant deviations of σ_{CME} from the universal value (4.2). The striking possibility of a drastic increase of the chiral magnetic conductivity due to the inter-electron interactions has recently been observed in a mean-field study with continuum Dirac fermions [14]. Now that more and more anomalous transport experiments with WSMs are being performed, a better theoretical understanding of the influence of inter-electron interactions on the chiral magnetic effect in solids is certainly desirable.

4.2 THE MODEL

In this work we are not interested in the properties of a specific material, but in general qualitative (anomalous) transport properties of WSMs. To this end it is not necessary to consider a realistic material with a complicated band structure. It is sufficient to work in a model that reproduces all the features of realistic WSMs.

In experiments one typically works with static and homogeneous magnetic fields and a static or low-frequency electric field [5, 6, 60, 61]. In such a setup it is a good approximation to assume that the current induced by the static magnetic field is also static. The calculation of the current can then be performed assuming that the whole system is in thermodynamic equilibrium, which greatly simplifies the computation.

The defining property of a WSM is the emergent chiral symmetry at small energies and the existence of low energy excitations that behave like Weyl fermions. A $\mathcal{P}$-breaking WSM in thermodynamic equilibrium can be modelled by a time-independent Dirac-type Hamiltonian with finite chiral chemical potential μ_A. As we have mentioned above, the chiral charge is not conserved due to the anomaly and the notion of a chiral chemical potential is problematic. Moreover, calculations in the framework of chiral kinetic theory [78, 79], magnetostatics [80, 81] and magnetohydrodynamics [82] point to the existence of the so-called chiral plasma instability: In a plasma of chiral fermions that is coupled to an electromagnetic field the chiral chemical potential decays at the expense of increasing the magnetic helicity. The origin of the chiral plasma instability is the coupling of the chiral fermions to the magnetic field. In solid state systems the interaction with the magnetic field is suppressed by a factor of $1/v_F$, which is quite large in WSMs. It is therefore reasonable to assume that the timescale of the decay of the chiral imbalance in a WSM is much larger than the timescale for the dynamics due to the inter-electron interactions, like for example the spontaneous breaking of chiral symmetry and the formation of a chiral condensate. Real-time simulations of the chiral plasma instability support this assumption [83]. Furthermore, the decay of the chiral chemical potential can be compensated by "chirality pumping" in parallel electric and magnetic fields, as described by Equation (4.3). We conclude that the concept of a chiral chemical potential, albeit ill defined in general, can be quite useful as an approximation if either the timescale of the dynamics one is interested in is much smaller than the decay time of the chiral imbalance or if the decay is counterbalanced by the generation of chiral charge in parallel or circularly polarised electromagnetic fields.

Since the magnetic interactions are suppressed by a factor of v_F/c compared to the electric interactions, we neglect the magnetic part of the electromagnetic inter-electron interactions in our model. In this first, exploratory study we keep the model as simple as possible and only include spontaneous on-site inter-electron interactions. In general, mean-field phase diagrams with only on-site interactions qualitatively reproduce the most important features of phase diagrams obtained with more realistic interaction potentials. Moreover, as we will see later on, this approximation significantly reduces the complexity of the calculations in the mean-field approximation. The instantaneous approximation, on the other hand, is justified by the smallness of the Fermi velocity v_F in realistic WSMs.

In any realistic WSM the chiral symmetry around the Weyl points in the spectrum is just a low-energy effective symmetry and it is explicitly broken for high energies. The possible patterns of spontaneous symmetry breaking in a WSM are therefore quite different than for continuum Dirac fermions.

It is therefore important to go beyond a simple Dirac cone approximation and take the explicit breaking of chiral symmetry into account. The ansatz [58, 84–87] for our tight-binding lattice model of a WSM is the Wilson–Dirac Hamiltonian with finite bare

chiral chemical potential μ_A^0 and a repulsive on-site inter-electron interaction potential $U > 0$:

$$\hat{H} = \sum_{x,y} \hat{\psi}_x^\dagger h_{xy}^{(0)} \hat{\psi}_y + U \sum_x \left(\hat{\psi}_x^\dagger \hat{\psi}_x - 2 \right)^2 , \tag{4.4}$$

where the sums run over all the lattice sites, $h_{xy}^{(0)}$ is the single-particle Wilson–Dirac Hamiltonian on the isotropic three-dimensional cubic lattice and $\hat{\psi}_x^\dagger$ and $\hat{\psi}_y$ are the fermionic creation and annihilation operators at the lattice sites x and y. In the absence of external gauge fields the momentum space single-particle Hamiltonian is given by

$$h^{(0)}(\vec{k}) = \sum_{i=1}^{3} \alpha_i v_F \sin(k_i) + 2r\gamma_0 \sum_{i=1}^{3} \sin^2(k_i/2) + \gamma_0 m^0 + \gamma_5 \mu_A^0, \tag{4.5}$$

with the Dirac mass term m^0, the Fermi velocity v_F and the Wilson coefficient r. The explicit form of the Dirac matrices α_k and the gamma matrices is given in Appendix A. In Equation (4.5) we have applied a convention from lattice QCD, where the lattice spacing a is set to $a = 1$ and all dimensionful quantities are measured in units of the lattice spacing a. If necessary the explicit dependence on the lattice spacing can be restored by dimensional analysis.

In momentum space the single-particle Hamiltonian is given by

$$h_{xy}^{(0)} = \sum_{k=1}^{3} -i\alpha_k v_F \nabla_{k,xy} + \frac{r\gamma_0}{2} \Delta_{xy} + \gamma_0 m^0 + \gamma_5 \mu_A^0 \tag{4.6}$$

and the dependence of the Hamiltonian (4.4) on external gauge fields $\vec{A}(\vec{x})$ can be incorporated by applying a Peierls substitution of the link phases $A_{x,k} = \int_x^{x+\hat{k}} A_{x,k}(z)\,dz$, where $\hat{k}$ is the lattice unit vector in direction k, to the finite difference operators [88–90]. After the Peierls substitution the lattice discretisations of the covariant derivative operator ∇_k and the Laplacian $\Delta = -\nabla_k^2$ are given by

$$\begin{aligned} \nabla_{k,xy} &= \frac{1}{2} \left(e^{iA_{x,k}} \delta_{x+\hat{k},y} - e^{-iA_{x-\hat{k},k}} \delta_{x-\hat{k},y} \right) \quad \text{and} \\ \Delta_{xy} &= \sum_{k=1}^{3} \left(2\delta_{x,y} - e^{iA_{x,k}} \delta_{x+\hat{k},y} - e^{-iA_{x-\hat{k},k}} \delta_{x-\hat{k},y} \right). \end{aligned} \tag{4.7}$$

Note that in the Hamiltonian (4.4) we ignore back-reactions and treat the vector potential $A_k(x)$ as a non-dynamical external field, which acts as the source of the static electric current.

Altogether there are five free parameters in our model: The bare mass m^0 and bare chiral chemical potential μ_A^0, the strength of the inter-electron interaction U, the Wilson parameter r and the Fermi velocity v_F.

In Appendix B we show that the dependence on the Fermi velocity is trivial and changing v_F simply amounts to a rescaling of the model parameters and observables. We can therefore set $v_F = 1$ in all our calculations and the dependence of our results on v_F can be restored with the help of the expressions given in Appendix B.

The dependence of the single-particle Hamiltonians (4.5) and (4.6) on the Wilson parameter is non-trivial. Changing r amounts to rescaling the phase diagram in the

m^0-direction and an additional squeezing/stretching. Nevertheless, as we show in Appendix B, qualitatively the phase structure of our model looks the same for different values of r. In order to further reduce the number of free parameters we thus also set the Wilson parameter to $r = 1$.

4.3 THE PARTITION FUNCTION

In thermodynamic equilibrium all physical properties of a system can be derived from the partition function and its derivatives. The partition function at temperature T is given by

$$\mathcal{Z} = \operatorname{tr} \exp\left(-\beta \hat{H}\right); \quad \beta = T^{-1}. \tag{4.8}$$

Even for the simple model Hamiltonian (4.4) it is not possible to calculate the partition function analytically. In this work we follow [14] and use a mean-field ansatz as a starting point for numerical calculations. As a first step we have to bring the partition function of our model in a form suitable for performing a mean-field approximation.

We begin by splitting the Hamiltonian (4.4) in a free part $\hat{H}_0$ and the inter-electron interaction term $\hat{H}_I$. Applying a Suzuki–Trotter decomposition and introducing the notation $\Delta\tau = \beta/N$ the exponent in the partition function can be rewritten as

$$e^{-\beta \hat{H}} = e^{-\beta(\hat{H}_0 + \hat{H}_I)} = \lim_{N\to\infty} \left(e^{-\Delta\tau \hat{H}_0} e^{-\Delta\tau \hat{H}_I}\right)^N. \tag{4.9}$$

In terms of the charge operator $\hat{q}_x = \sum_\alpha \hat{\psi}^\dagger_{x,\alpha}\hat{\psi}_{x,\alpha} - 2$, where the sum runs over the Dirac indices α, the interaction term is given by $\hat{H}_I = U \sum_x \hat{q}_x^2$. What makes the evaluation of the partition function challenging is the term with a product of four fermionic operators, which appears if we square the charge operator:

$$\begin{aligned} \hat{q}_x^2 &= \left(\hat{\psi}^\dagger_{x,\alpha}\hat{\psi}_{x,\alpha} - 2\right)\left(\hat{\psi}^\dagger_{x,\beta}\hat{\psi}_{x,\beta} - 2\right) \\ &= -\hat{\psi}^\dagger_{x,\alpha}\hat{\psi}_{x,\beta}\hat{\psi}^\dagger_{x,\beta}\hat{\psi}_{x,\alpha} + \hat{\psi}^\dagger_{x,\alpha}\hat{\psi}_{x,\alpha}, \end{aligned} \tag{4.10}$$

In Equation (4.10) and for the rest of this chapter we assume an implicit summation over repeated Dirac indices to avoid a cluttered notation. Note that the charge operators $\hat{q}_x$ and $\hat{q}_y$ at different lattice sites x and y commute and we can write

$$\exp\left(-\Delta\tau \hat{H}_I\right) = \prod_x \exp\left(-U\,\hat{q}_x^2\right). \tag{4.11}$$

Inserting (4.10) into Equation (4.11) gives terms of the form

$$\exp\left(-\Delta\tau\, U\,(\hat{\psi}^\dagger_{x,\alpha}\hat{\psi}_{x,\beta}\hat{\psi}^\dagger_{x,\beta}\hat{\psi}_{x,\alpha} + \hat{\psi}^\dagger_{x,\alpha}\hat{\psi}_{x,\alpha})\right) \tag{4.12}$$

and we can use the Baker–Campbell–Hausdorff formula to replace (4.12) by a product of exponents:

$$\exp\left(-\Delta\tau\, U\, \hat{\psi}^\dagger_{x,\alpha}\hat{\psi}_{x,\beta}\hat{\psi}^\dagger_{x,\beta}\hat{\psi}_{x,\alpha}\right) \exp\left(-\Delta\tau\, U\, \hat{\psi}^\dagger_{x,\alpha}\hat{\psi}_{x,\alpha})\right). \tag{4.13}$$

In doing so we make an error of $\mathcal{O}(\Delta\tau^2)$, which vanishes in the limit $\Delta\tau \to 0$ ($N \to \infty$).

What we have achieved so far is to rewrite an exponential function of a sum of operators as an product of exponential functions. The exponents containing products of at most two fermionic operators will lead to simple Gaussian integrals, but the term with a product of four fermionic operators cannot be treated analytically.

The next task is to rewrite the exponential function of a product of four fermionic operators in a more manageable form and to this end we perform a Hubbard–Stratonovich transformation [91, 92]. The Hubbard–Stratonovich transformation is a generalisation of the Gaussian integral identity

$$\exp\left(-\kappa x^2\right) = \frac{1}{\sqrt{\kappa\pi}} \int_{-\infty}^{\infty} \exp\left(-\frac{y^2}{4\kappa} - ixy\right) dy \quad \kappa \in \mathbb{R}^+ \tag{4.14}$$

and allows us to rewrite the first exponential function in (4.13) in terms of a Gaussian integral over an auxiliary Hubbard–Stratonovich field Φ_x containing only products of at most two fermionic operators. In principle, the Hubbard–Stratonovich field is just a dummy integration variable and the specific form of the field does not matter. This is true if the integration over the field is performed exactly, but later on we want to apply a mean-field approximation. As we will see, the choice of the field then has an effect on the possible mean-field condensates. Keeping this in mind we choose a general form for the Hubbard–Stratonovich field where $\Phi_x = \Phi_{x,\alpha\beta}(\tau)$ can be any Hermitian matrix in spinor space and can have an explicit Euclidean time dependence:

$$\exp\left(-\Delta\tau\, U\, \hat{\psi}^\dagger_{x,\alpha}\hat{\psi}_{x,\beta}\hat{\psi}^\dagger_{x,\beta}\hat{\psi}_{x,\alpha}\right) = \int d\Phi_{x,\alpha\beta} \exp\left(-\frac{\Delta\tau}{4U}\Phi_{x,\alpha\beta}\Phi_{x,\beta\alpha} - \Delta\tau\Phi_{x,\alpha\beta}\hat{\psi}^\dagger_{x,\alpha}\hat{\psi}_{x,\beta}\right), \tag{4.15}$$

where we have suppressed the explicit τ dependence of the field $\Phi_{x,\alpha\beta}$ in our notation and absorbed the constant $1/\sqrt{\pi U}$ in the definition of the integral measure $d\Phi_{x,\alpha\beta}$.

Inserting our results (4.11),(4.13) and (4.15) into (4.9) and taking the limit $\Delta\tau \to 0$ we can express the partition function (4.8) in terms of the partition function $\mathcal{Z}_0[\Phi_x(\tau)]$ of a free fermion gas in the background of the Hubbard–Stratonovich field $\Phi_x(\tau)$. Using the time ordering operator $\mathcal{T}$ and switching to a matrix-vector notation in spinor space we arrive at

$$\mathcal{Z} = \int \mathcal{D}\Phi_{x,\alpha\beta}(\tau)\mathcal{Z}_0[\Phi_x(\tau)] \exp\left(-\frac{1}{4U}\int_0^\beta \operatorname{tr}\Phi_x^2(\tau)d\tau\right), \tag{4.16}$$

where the partition function $\mathcal{Z}_o$ is given by

$$\mathcal{Z}_0[\Phi_x(\tau)] = \operatorname{tr}\mathcal{T}\exp\left(-\int_0^\beta \left(\hat{H}_0 + \sum_x \hat{\psi}^\dagger_x \Phi_x(\tau)\hat{\psi}_x\right) d\tau\right). \tag{4.17}$$

It is important to stress that so far we have not used any approximations. The partition function (4.16) is still exact. What we have achieved by using the Hubbard–Stratonovich transformation to rewrite the partition function is to bring it to a form that is well suited for a mean-field approximation.

4.4 THE FREE ENERGY IN THE MEAN-FIELD APPROXIMATION

Starting from the partition function in the form (4.16) we can compute the free energy of the model in the mean-field approximation. The mean-field approximation amounts to replacing the integral over the field $\Phi_x(\tau)$ by a saddle-point approximation. It is at this point of our calculation that the type of the field $\Phi_x(\tau)$ becomes important. In general, the saddle-point of a matrix valued field will be different than, for example, the saddle-point of a scalar field.

Let $\Phi^\star(\tau)$ be the value of the Hubbard–Stratonovich field at the saddle-point. Under the additional assumption that $\Phi^\star(\tau) = \Phi^\star$ does not depend on the Euclidean time τ, the free energy $\mathcal{F} = -T\ln(\mathcal{Z})$ in the mean-field approximation is given by

$$\mathcal{F}[\Phi_x^\star] = \mathcal{F}_0[\Phi_x^\star] + \sum_x \frac{\operatorname{tr}\Phi_x^{\star 2}}{4U}, \tag{4.18}$$

where $\mathcal{F}_0[\Phi_x]$ is the free energy of the free single-particle Hamiltonian

$$\hat{h}_{xy} = h_{xy}^{(0)} + U\delta_{xy} + \Phi_x\delta_{xy}. \tag{4.19}$$

Explicitly $\mathcal{F}_0[\Phi_x]$ reads as

$$\begin{aligned}\mathcal{F}_0[\Phi_x] &= -T\ln\left[\operatorname{tr}\exp\left(-\beta\sum_{x,y}\hat{\psi}_x^\dagger\hat{h}_{xy}\hat{\psi}_y\right)\right] \\ &= -T\sum_i \ln\left(1+e^{-\beta\varepsilon_i}\right)\end{aligned} \tag{4.20}$$

and the sum in the second line is over all energy levels ε_i of the single particle Hamiltonian (4.19).

Experiments with WSMs are typically performed at very low temperatures of order $\sim$ 10K [5, 6, 60, 61]. We will thus perform most of our calculations in the limit of vanishing temperature. The effects of finite temperature on our results are discussed in Sections 4.5.3 and 5.2.1.

In the limit $T \to 0$ the terms $-T\ln\left(1+e^{-\beta\varepsilon_i}\right)$ in (4.20) become $\Theta(-\varepsilon_i)$, where

$$\Theta(x) = \begin{cases} 0 & x < 0 \\ 1 & x \geqslant 0 \end{cases} \tag{4.21}$$

is the Heaviside step function. The free energy is then given by

$$\mathcal{F} = \sum_{\varepsilon_i<0}\varepsilon_i + \sum_x \frac{\operatorname{tr}\Phi_x^{\star 2}}{4U}. \tag{4.22}$$

The first sum in (4.22) is the fermionic contribution to the free energy and has an intuitive physical interpretation: In the ground state all the negative energy states of the Dirac sea are filled and all the positive energy states are empty. Therefore, the fermionic free energy is simply the sum over all the negative energy levels.

If we restore the spin indices in the single-particle Hamiltonian, we find that it contains a term, $U\delta_{\alpha\beta}\delta_{xy}$, which is diagonal in spinor space and therefore acts as an effective chemical potential. A finite chemical potential induces a finite electric charge in the

system. Our initial Hamiltonian describes an electrically neutral system and this would lead to a violation of charge conservation. Note that the Hubbard–Stratonovich field $\Phi_{x,\alpha\beta}$ also contains terms that can introduce an effective chemical potential. We can explicitly rewrite the Hubbard–Stratonovich field $\Phi_{x,\alpha\beta} = \mu_{\text{eff}}\delta_{\alpha\beta} + \widetilde{\Phi}_{x,\alpha\beta}$ as the sum of an effective chemical potential term and a traceless Hermitian matrix $\widetilde{\Phi}_{x,\alpha\beta}$. In [14] it was shown that in a self-consistent mean-field approximation the term $U\delta_{\alpha\beta}\delta_{xy}$ will be exactly cancelled by the contribution $\mu_{\text{eff}}\delta_{\alpha\beta}$ from the Hubbard–Stratonovich field and that the total chemical potential is zero. This means that we can simplify our model by considering only trace-less Hubbard–Stratonovich fields Φ_x from now on and by simultaneously replacing the effective single-particle Hamiltonian (4.19) by

$$\hat{h}_{xy} = h^{(0)}_{xy} + \Phi_x \delta_{xy}. \tag{4.23}$$

Additionally, we introduce a "physical basis" for the Hubbard–Stratonovich fields and write Φ_x as a sum over a basis set of 15 traceless Hermitian matrices:

$$\begin{aligned} &\Phi_x = \sum_{A=1}^{15} \Gamma_A \Phi_{x,A}\ , \\ &\Gamma_A \in \{\gamma_5\alpha_k, \gamma_0, \gamma_0\gamma_5\alpha_k, -i\gamma_5\gamma_0, i\gamma_0\alpha_k, \gamma_5, \alpha_k\}\ , \end{aligned} \tag{4.24}$$

where the index $k \in \{1,2,3\}$ labels the spatial directions. It is straightforward to check that the basis matrices are normalised such that $\operatorname{tr}(\Gamma_A\Gamma_B) = 4\delta_{AB}$ and the trace of the squared Hubbard–Stratonovich field is given by $\operatorname{tr}\Phi_x^2 = 4\sum_{A=1}^{15}\Phi_{x,A}^2$. In the mean-field approximation a non-zero value of $\Phi_{x,\alpha\beta} = \Phi^\star_{x,\alpha\beta}$ corresponds to a finite value of the fermionic condensate, i.e. $\Phi_{x,\alpha\beta} \propto \langle\hat{\psi}^\dagger_{x,\alpha}\hat{\psi}_{x,\beta}\rangle$. The basis (4.24) is very convenient if we are interested in the properties of the condensates under symmetry transformations.

4.5 MEAN-FIELD PHASE DIAGRAM

A priori there are no physical constraints for the saddle-point Hubbard–Stratonovich $\Phi^\star_x$ field and it can depend on the lattice site x. To make the computation of the phase diagram and the transport properties of the model significantly simpler, we assume that $\Phi^\star = \Phi^\star_x$ is homogeneous and isotropic. Under this assumption, whose validity will be discussed in more detail later on, all possible saddle-point values can be written in the form

$$\Phi^\star = (m_r - m^0)\gamma_0 + i m_i \gamma_0\gamma_5 + (\mu_A - \mu_A^0)\gamma_5, \tag{4.25}$$

where we introduced the renormalised mass m_r, the renormalised chiral chemical potential μ_A and the $\mathcal{CP}$-breaking mass term m_i, which corresponds to the "pion" (or "axion") condensate $\langle\hat{\psi}^\dagger\gamma_0\gamma_5\hat{\psi}\rangle$. Remember that the chiral chemical potential is not coupled to a conserved charge and is not protected from renormalisation.

Using the ansatz (4.25) the mean-field free energy for a lattice with spatial extend L_s has the simple form

$$\frac{\mathcal{F}[\Phi^\star]}{L_s^3} = \frac{1}{L_s^3}\sum_{\varepsilon<0}\varepsilon + \frac{(m_r - m^0)^2 + m_i^2 + (\mu_A - \mu_A^0)^2}{U}. \tag{4.26}$$

In the absence of external fields (i.e. $A_{x,k} = 0$) the energy levels of the effective single-particle Hamiltonian (4.23) can be evaluated analytically and are given by

$$\varepsilon = \varepsilon_{s,\sigma}(\vec{k}) = s\sqrt{(S - \sigma\mu_A)^2 + m_i^2 + (m_r + W)^2}, \tag{4.27}$$

where $s \pm 1$, $\sigma \pm 1$ and we define the abbreviations $S = \sqrt{\sum_{k_i} \sin^2(k_i)}$ and $W = \sum_{k_i} 2\sin^2(k_i/2)$ for the sake of better readability.

The parameter space of our model is quite large and it is not feasible to scan over all possible values of the free parameters. Ultimately we are only interested in regions in parameter space where our model reproduces the features of a WSM. In particular, this means that we can discard parts of the parameter space where the renormalised mass is large and chiral symmetry is broken explicitly even at small energies.

To better understand the effect of mass renormalisation in our model let us look at the Wilson–Dirac Hamiltonian (4.4) again. As we have seen in Section 2.2.1, in lattice QCD Wilson introduced the term proportional to Δ_{xy} to get rid of the doublers. Here, however, Wilson–Dirac fermions are used to model the band structure of a crystal, where the lattice spacing has a fixed and finite value. In our model the Wilson term is added to take into account the fact that the continuum chiral symmetry in realistic WSMs is only an emergent symmetry at low energies and is explicitly broken away from the Weyl points.

In a crystal the doublers are observable physical excitations. Their mass is given by the poles of the propagator in momentum-space. It is sufficient to consider the first Brillouin zone, i.e. crystal momenta $k_i \in (-\pi, \pi]$, and the poles are located at positions where $\sum_{ki} \sin^2(k_i) = 0$, see Equation (2.35). In the notation of this chapter the mass of the doublers is given by

$$m_d = m_r + 2\lambda, \tag{4.28}$$

where λ is the number of components of $\vec{k}$ with $k_i \neq 0$. In three dimensions λ can take four values: $\lambda = 0, 1, 2, 3$. The values $\lambda = 0$ and $\lambda = 3$ can only be achieved in one way, all components of $\vec{k}$ have to be the same. For $\lambda = 1$ there are three possibilities to place the entry π in a three-dimensional vector

$$\vec{k} = (\pi, 0, 0)^T, \quad \vec{k} = (0, \pi, 0)^T \quad \text{and} \quad \vec{k} = (0, 0, \pi)^T. \tag{4.29}$$

By the same argument there are three ways to place the 0 for $\lambda = 2$. Hence for a mass of $m_r = 0$ and -6 there is $N_f = 1$ Dirac cone in the spectrum of our model, whereas there are $N_f = 3$ Dirac cones for $m_r = -2$ and -4. In the limit $U \to 0$ the renormalised mass $m_r = m^0$ and from Equation (4.28) it is easy to see that non-trivial phases with massless excitations can only exist for $-6 \leqslant m^0 \leqslant 0$. Thus we restrict m^0 to this parameter range in our study of the phase diagram.

Remember that we have set $v_F = r = 1$ and expressed all dimensionful quantities in units of the lattice spacing a. There are now only three free parameters left in our model, namely the bare mass m^0, the bare chiral chemical potential μ_A^0 and the inter-electron interaction potential U. We scan over these free parameters to compute the phase diagram. The value of the mean-field parameters can be found by minimising the free energy (4.22) with respect to m_r,μ_A and m_i. A variant of the differential evolution algorithm [93] is used to find the global minimum of the free energy numerically.

The mean-field phase diagram of our model features two distinct phases – an "Aoki" phase [94] where the $\mathcal{CP}$-symmetry is spontaneously broken by a non-zero $\mathcal{CP}$-breaking mass term $m_i \neq 0$ and a $\mathcal{CP}$-symmetric phase where $m_i = 0$. The spontaneous breaking of the discrete $\mathcal{CP}$ symmetry in the lattice model (4.4) is a remnant of the spontaneous breaking of the continuous chiral symmetry, which is only a emergent low-energy symmetry for Wilson–Dirac fermions.

In condensed matter and solid state physics terminology the Aoki phase is known as "axionic insulator" phase with an non-zero condensate of an effective axion field. (For some recent examples of effective axion fields in condensed matter systems see e.g. [86, 95–97].)

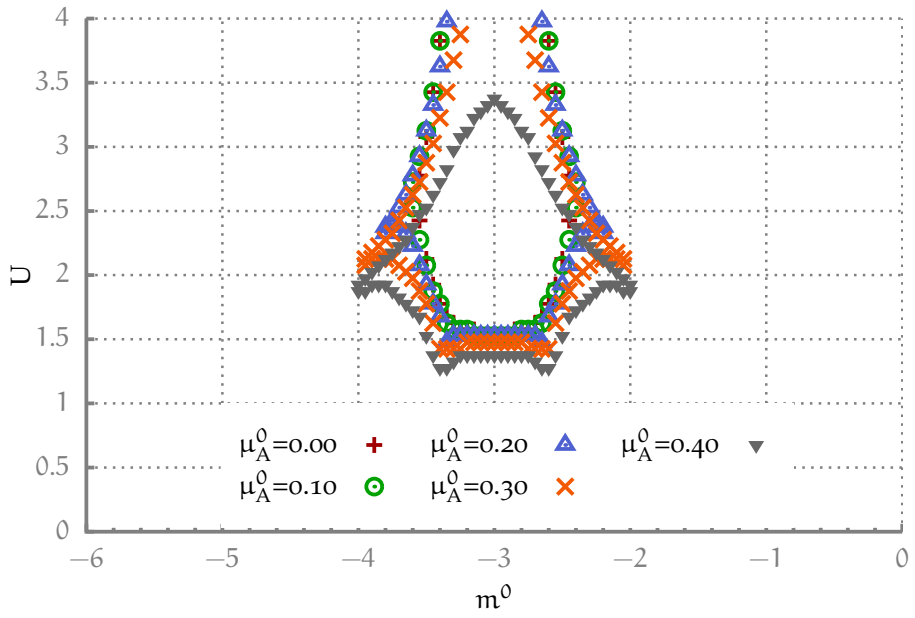

Figure 4.2: Mean-field phase diagram for the model (4.4) in the m^0-U–plane for different values of the bare chiral chemical potential. The symbols mark the boundary of the Aoki phase. The $\mathcal{CP}$-breaking mass term $m_i \neq 0$ in the region enclosed by the symbols.

The mean-field phase diagram of our model in the m^0-U-plane for different values of the bare chiral chemical potential μ_A^0 is depicted in Figure 4.2. We find that the phase diagram is symmetric around the line where $m^0 = -3$. Increasing the value of μ_A^0 shifts the critical inter-electron interaction potential for the onset of the Aoki phase to smaller values. An analogous effect was observed in a model of interacting continuum Dirac fermions, where the chiral chemical potential decreases the critical interaction strength for spontaneous chiral symmetry breaking [14].

In Figure 4.3a the mean-field value of the $\mathcal{CP}$-breaking mass term m_i is plotted as a function of U for different values of the bare chiral chemical potential and m^0. The transition between the normal insulator/semimetal phase and the Aoki phase with $m_i \neq 0$ appears to be a sharp second-order phase transition for all values of μ_A^0.

The chiral chemical potential is subject to a strong multiplicative renormalisation. Figure 4.3b shows the renormalised chiral chemical potential as a function of U for different values of μ_A^0 and m^0. If the initial bare chiral chemical potential is zero, the renormalised chiral chemical potential stays zero up to the highest values of U investigated in

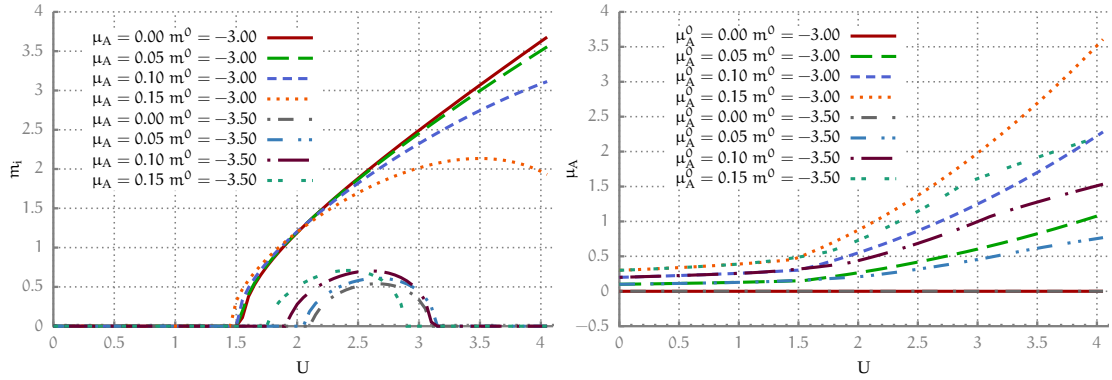

(a) (b)

Figure 4.3: (a) The $\mathcal{CP}-$breaking mass term m_i as a function of the interaction potential U for different values of the bare mass m^0 and bare chiral chemical potential μ_A^0. (b) The renormalised chiral chemical potential μ_A as a function of the interaction potential U at fixed values of m^0 and μ_A^0.

this study. For every finite value of μ_A^0, on the other hand, a strong renormalisation of the chiral chemical potential is observed in both phases of our model. The increase of μ_A^0 with U is a bit stronger in the phase with broken $\mathcal{CP}$-symmetry. This can be seen, for example, in the plot for μ_A with $\mu_A^0 = 0.15$ and $m^0 = -3.50$, where a small kink is visible around $U = 3$. Comparing with the plots for m_i in Figure 4.3a it becomes clear that this kink coincides with a change from the Aoki phase to the $\mathcal{CP}$-symmetric phase. Again the results are in good qualitative agreement with [14].

4.5.1 *Finite Volume Effects*

All results presented so far were achieved with a lattice of spacial extend $L_s = 50$. Possible finite size effects on the phase diagram were addressed in [52]. There it was found numerically for $L_s = 8, 10, 12$ that finite size effects have little influence on the mean-field phase diagram. In general, our results for $L_s = 50$ confirm these findings, but we observe that the so called "Aoki fingers", the thin structures which point to the values of $m^0 = 0, -1, -3, -6$, get thinner as L_s is increased. As is shown in Figure 4.4, for $L_s = 50$ we are no longer able to resolve the fingers numerically.

Even for small lattice sizes the Aoki fingers vanish (or are too small to be resolved) as soon as we introduce a finite bare chiral chemical potential μ_A^0. To study the anomalous transport properties of our model we are working with values $0 < \mu_A^0 < 0.3$ of the bare chiral chemical potential. The volume dependence of the Aoki fingers is thus of minor importance for the main points of this work and we will use $L_s = 50$ in all our calculations.

4.5.2 *Fate of the Aoki Fingers*

The Aoki fingers are an interesting feature of our model and for completeness we briefly discuss their finite volume dependence for $\mu_A^0 = 0$. In [94] Aoki has published a conjecture for the phase diagram of lattice QCD with Wilson fermions. A phase diagram with

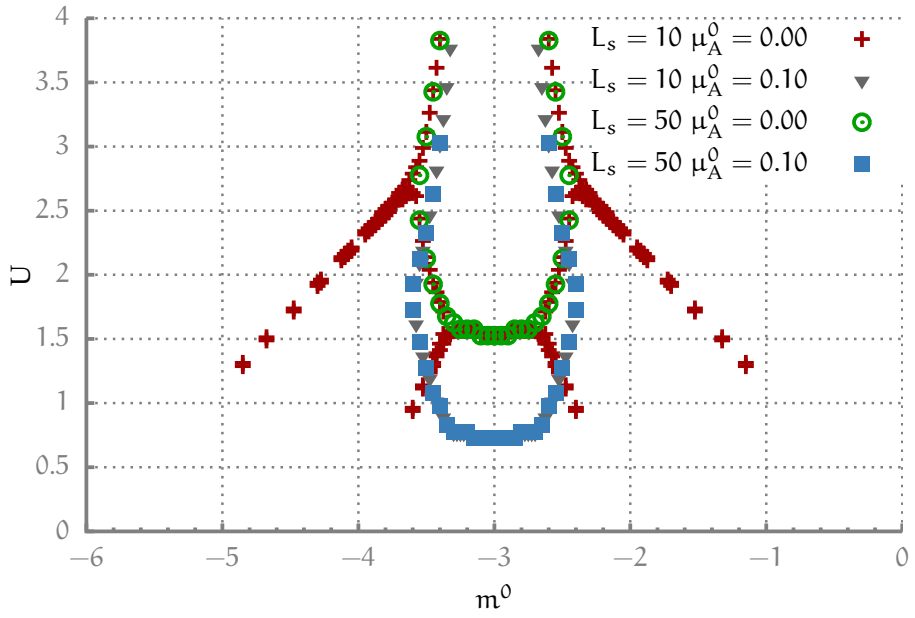

Figure 4.4: Dependence of the mean-field phase diagram on L_s. The Aoki fingers are volume dependent and seem to vanish in the limit $L_s \to \infty$. For finite values of μ_A^0 the fingers are not present and the phase diagrams for different lattice sizes L_s overlap within numerical precision. The phase boundaries for $\mu_A^0 = 0.10$ are shifted by -0.8 in U-direction for better visibility.

two phases was suggested, based on calculations in the two-dimensional Gross–Neveu model and in an effective model of lattice QCD. In the context of our model the order parameter for the phase transition is the $\mathcal{CP}$-breaking term m_i, which becomes finite in one phase (Aoki phase, axionic insulator phase) and vanishes in the other phase. In the Hamiltonian formalism time is not discretised and is treated as a continuous variable. Thus in the conjectured phase diagram in D dimensions the Aoki phase forms D fingers, which touch the bare mass axis at characteristic points as the coupling U goes to zero.

A simple heuristic argument shows that in our model, in general, the fingers will not extend all the way down to touch the bare mass axis. The "pion" mass, which is given by $m_\pi^2 = \frac{\partial^2 \mathcal{F}}{\partial m_i^2}$, has to vanish at the border of the Aoki phase. In $D = d + 1$ dimensions the second derivative of the mean-field free energy (4.26) is given by

$$\frac{\partial^2 \mathcal{F}}{\partial m_i^2} = \frac{1}{2L_s^d} \sum_{\vec{k},\sigma} \left(\frac{1}{\varepsilon_{-1,\sigma}(\vec{k})} - \frac{m_i^2}{\varepsilon_{-1,\sigma}(\vec{k})^3} \right) - \frac{2}{U}, \tag{4.30}$$

where $\vec{k}$ is now a d-dimensional vector and we sum over all vectors $\vec{k}$ in the Brillouin zone. If we take the limit $L_s \to \infty$ the sum in (4.30) becomes an integral:

$$\frac{1}{L_s^d} \sum_{\vec{k}} \to \frac{1}{(2\pi)^d} \int d\vec{k} \propto \int dk\, k^{(d-1)}. \tag{4.31}$$

In the last integral we have switched to d-dimensional spherical coordinates. If $\mu_A^0 = 0$ the energy levels become degenerate[1] and we define $\varepsilon_{-1} := \varepsilon_{-1,1} = \varepsilon_{-1,-1}$. The phase

1 The d-dimensional energy levels are simply a generalisation of (4.27).

transition is not of first order and therefore m_i is continuous across the phase boundary. Consequently close to the phase boundary $m_i \ll 1$ and around points of constant $W + m_r = 0$ the integral is dominated by the contributions from $k \ll 1$ approximated by

$$\frac{\partial^2 \mathcal{F}}{\partial m_i^2} \approx \frac{2}{U} - \gamma \int dk\, k^{(d-1)} \left(\frac{1}{\sqrt{k^2 + m_i^2}} - \frac{m_i^2}{\sqrt{(k^2 + m_i^2)^3}} \right), \tag{4.32}$$

where the normalisation factors $1/(2\pi)$ and the contribution from the solid angle integral are combined in the positive constant γ. For the following argument the exact numerical value of γ is not important.

Obviously the term $2/U$ diverges as we approach the bare mass axis. For the pion mass $m_\pi^2 = \frac{\partial^2 \mathcal{F}}{\partial m_i^2}$ to vanish, this divergence has to be cancelled by the integral in (4.32).

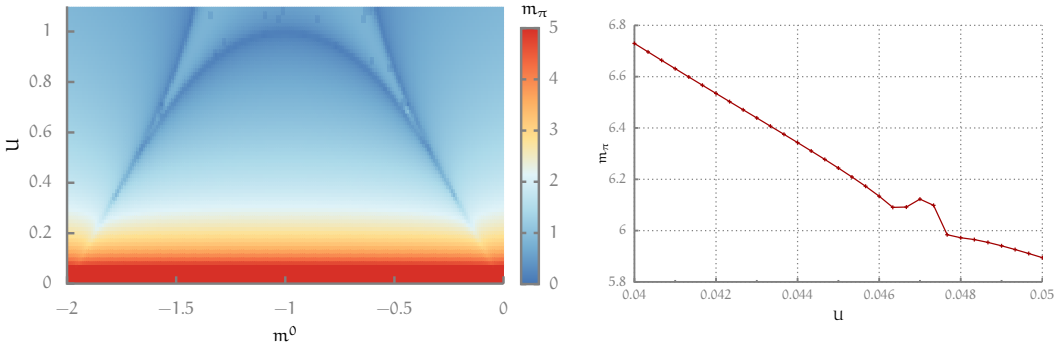

Figure 4.5: Pion mass in 2D in the limit $L_S \to \infty$. Left: Pion mass in the m^0-U–plane. At the border of the Aoki phase $m_{pi} = 0$ and the Aoki fingers are clearly visible up to very small values of U. Right: The small peak in the pion mass around $U = 0.047$ at $m^0 = -1.97$ is a sign for the existence of the Aoki phase. The vanishing of the pion mass at the phase boundaries is hard to resolve in numerical calculations.

If we fix the dimension to $D = 1 + 1$, the integral of the first term will diverge as $\ln(m_i)$ and the integral of the second term will not be divergent as $m_i \to 0$. It is then possible to cancel the divergence and the Aoki fingers can reach all the way down to the bare mass axis. Results of numerical calculations in our model in the limit $L_S \to \infty$ in $D = 1 + 1$ dimensions are shown in Figure 4.5. The results strongly support our heuristic reasoning and are consistent with the statement that the Aoki fingers touch the bare mass axis.

Let us now turn to the case $D = 3 + 1$. Here the first integral is not divergent as $m_i \to 0$ and neither is the second integral. Thus the Equation (4.32) does no longer have roots for small values of U and the Aoki phase cannot persist all the way down to the bare mass axis.

The same argument can explain why the Aoki fingers depend on the lattice size L_S. For small L_S the sum in Equation (4.30) diverges as $1/\sqrt{k^2}$ for vanishing m_i and a solution for $\frac{\partial^2 \mathcal{F}}{\partial m_i^2} = 0$ can be found even for small U. As L_S is increased, the sum becomes an ever better approximation of a (non-diverging) integral and hence (4.30) does no longer have roots for $U \ll 1$.

4.5.3 *Finite Temperature*

Although we will mostly work in the limit of $T \to 0$ it is interesting to check how the mean-field phase diagram depends on the temperature. Numerically this does not pose any difficulties, all we have to do is to replace the fermionic part of the free energy (4.26) by the more general expression (4.20).

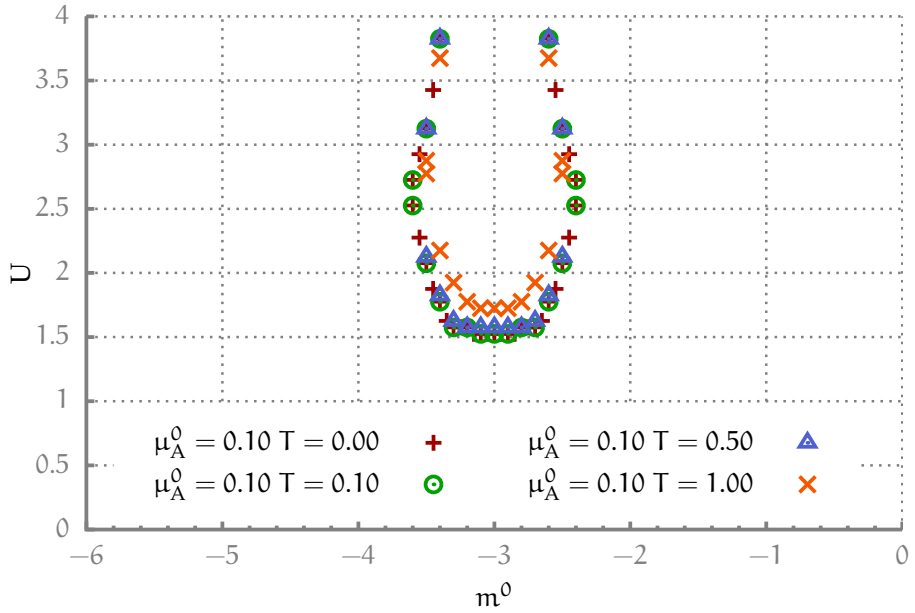

Figure 4.6: Phase diagram in the m^0-U-plane for different temperatures at fixed $\mu_A^0 = 0.10$.

In Figure 4.6 the phase diagram for different temperatures at fixed $\mu_A^0 = 0.10$ is shown. In general, finite temperature tends to "melt" the fermionic condensates and one expects that the onset of the Aoki phase is shifted to higher values of the inter-electron interaction potential U as T is increased. In our model this shift turns out to be quite small, even for a temperature $T = 1$, which is of the order of the bandwidth in our model.

5

STATIC CHIRAL MAGNETIC CONDUCTIVITY

In the lattice model (4.4) current can only flow along the links between adjacent lattice points. We denote the electric current in direction k at lattice site x by $j_{x,k}$. The expectation value of the current $j_{x,k}$ is given by the derivative of the free energy over the link phase factor $A_{x,k}$:

$$\langle j_{x,k} \rangle = \frac{\delta \mathcal{F}[A_{x,k}]}{\delta A_{x,k}}. \tag{5.1}$$

For the derivations in this chapter it is important to keep in mind that the free energy $\mathcal{F} = \mathcal{F}[A_{x,k}]$ depends on the link phases and we reflect this in our notation.

The linearised response of the current density to small external fields can be found by expanding Equation (7.17) around $A = 0$. In thermodynamic equilibrium the electric current vanishes in the absence of external gauge fields and therefore in the linear response approximation the current is given by

$$\langle j_{x,k} \rangle = \sum_{y,l} \frac{\delta^2 \mathcal{F}[A_{x,k}]}{\delta A_{x,k} \delta A_{y,l}} \bigg|_{A=0} A_{y,l}. \tag{5.2}$$

Ultimately we are not interested in the current itself, but in the static chiral magnetic conductivity σ_{CME}. The chiral magnetic conductivity is the proportionality constant that relates the external magnetic field to the induced current. In this work we consider static magnetic fields with a spacial modulation. We assume that the vector gauge potential is parallel to the second coordinate axis and that the wave vector of the magnetic field is parallel to the third axis. The magnetic field $B_i(x) = \epsilon_{ijk} \partial x_j A_k(x)$ and the current are then both parallel to the first coordinate axis. In momentum space the Kubo formula for σ_{CME} is given by [98–100]:

$$\begin{aligned} \sigma_{\text{CME}}(k_3) &= -\frac{i}{k_3} \frac{1}{L_S^3} \sum_{x,y} e^{ik_3(x_3 - y_3)} \langle j_{x,1} j_{y,2} \rangle \\ &= -\frac{i}{k_3} \frac{1}{L_S^3} \sum_{x,y} e^{ik_3(x_3 - y_3)} \frac{\delta \mathcal{F}[A_{x,k}]}{\delta A_{x,1} \delta A_{y,2}} \bigg|_{A=0}, \end{aligned} \tag{5.3}$$

where the (double) sum in the lattice Fourier transformation runs over all lattice sites.

5.1 SECOND VARIATION OF THE MEAN-FIELD FREE ENERGY

Equation (5.3) relates the chiral magnetic conductivity to the second variations of the free energy with respect to the link phases $A_{x,k}$. The mean field free energy $\mathcal{F} = \mathcal{F}[\Phi^\star]$

is given by minimising Equation (4.18) with respect to the Hubbard–Stratonovich field. In general, the free energy as well as the value $\Phi^\star$ of the Hubbard–Stratonovich at the minimum will depend on the external fields, i.e. $\mathcal{F}[\Phi^\star] = \mathcal{F}[\Phi^\star(A_{x,k}), A_{x,k}]$.

In this section, following the arguments in [14], we derive a formula for the second variation of the mean-field free energy, taking into account the explicit external field dependence of $\Phi^\star$. For the sake of a compact notation and to improve the readability of the formulas we switch to a multi-index notation. Uppercase letters with a bar are used as multi-index for Hubbard–Stratonovich fields and lowercase letters with a bar for the link phases. Moreover, we assume summation over multi-indices if they appear twice in an equation. In this notation the variation with respect to a link phase reads as

$$\frac{\delta}{\delta A_{\bar{a}}} = \frac{\partial}{\partial A_{\bar{a}}} + \frac{\delta \Phi_{\bar{A}}}{\delta A_{\bar{a}}} \frac{\partial}{\partial \Phi_{\bar{A}}}. \tag{5.4}$$

Using Equation (5.4) the second variation of the mean-field free energy is given by

$$\begin{aligned} \frac{\delta^2 \mathcal{F}}{\delta A_{\bar{a}} \delta A_{\bar{b}}}\bigg|_{\Phi^\star} &= \frac{\delta}{\delta A_{\bar{a}}} \left(\frac{\partial \mathcal{F}}{\partial A_{\bar{b}}} + \frac{\delta \Phi_{\bar{B}}}{\delta \partial A_{\bar{b}}} \frac{\partial \mathcal{F}}{\partial \Phi_{\bar{B}}} \right)\bigg|_{\Phi^\star} \\ &= \left(\frac{\partial^2 \mathcal{F}}{\partial A_{\bar{a}} \partial A_{\bar{b}}} + \frac{\delta \Phi_{\bar{A}}}{\delta A_{\bar{a}}} \frac{\partial^2 F}{\partial \Phi_{\bar{A}} \partial A_{\bar{b}}} + \right. \\ &\quad \left. + \frac{\delta \Phi_{\bar{B}}}{\delta A_{\bar{b}}} \frac{\partial^2 F}{\partial A_{\bar{a}} \partial \Phi_{\bar{B}}} + \frac{\delta \Phi_{\bar{B}}}{\delta A_{\bar{b}}} \frac{\delta \Phi_{\bar{A}}}{\delta A_{\bar{a}}} \frac{\partial^2 \mathcal{F}}{\partial \Phi_{\bar{A}} \partial \Phi_{\bar{B}}} \right)\bigg|_{\Phi^\star}, \end{aligned} \tag{5.5}$$

where we used the mean-field equation

$$\frac{\partial \mathcal{F}}{\partial \Phi_{\bar{A}}}\bigg|_{\Phi^\star} = 0 \tag{5.6}$$

to get rid of all the terms containing a first order derivative of the free energy with respect to the Hubbard–Stratonovich field.

It is clear how to compute the second order partial derivatives of the free energy in Equation (5.5), but we still need to find an explicit expression for the variation of the Hubbard–Stratonovich field with respect to the link phases. An implicit equation for this quantity can be found by computing the variation of Equation (5.6):

$$\frac{\delta}{\delta A_{\bar{a}}} \left(\frac{\partial \mathcal{F}}{\partial \Phi_{\bar{A}}} \right)\bigg|_{\Phi^\star} = \frac{\partial^2 \mathcal{F}}{\partial \Phi_{\bar{A}} \partial A_{\bar{a}}}\bigg|_{\Phi^\star} + \frac{\delta \Phi_{\bar{B}}}{\delta A_{\bar{a}}} \frac{\partial^2 \mathcal{F}}{\partial \Phi_{\bar{A}} \partial \Phi_{\bar{B}}}\bigg|_{\Phi^\star} = 0 \tag{5.7}$$

If we define the propagator $G_{\bar{A}\bar{B}}$ of the Hubbard–Stratonovich field $\Phi_{\bar{A}}$ via

$$G_{\bar{A}\bar{B}} \frac{\partial^2 \mathcal{F}}{\partial \Phi_{\bar{A}} \partial \Phi_{\bar{B}}}\bigg|_{\Phi^\star} = \delta_{\bar{A}\bar{B}} \tag{5.8}$$

the variation is given by

$$\frac{\delta \Phi_{\bar{B}}}{\delta A_{\bar{a}}}\bigg|_{\Phi^\star} = -G_{\bar{A}\bar{B}} \frac{\partial^2 \mathcal{F}}{\partial \Phi_{\bar{A}} \partial A_{\bar{a}}}\bigg|_{\Phi^\star}. \tag{5.9}$$

Using Equation (5.7) it is straightforward to see that the sum in the last line of Equation (5.5) is equal to zero. Exchanging the remaining variation term with the right hand side of Equation (5.9), the second variation of the mean-field free energy reads as

$$\frac{\delta^2 \mathcal{F}}{\delta A_{\bar{a}} \delta A_{\bar{b}}}\bigg|_{\Phi^\star} = \frac{\partial^2 \mathcal{F}}{\partial A_{\bar{a}} \partial A_{\bar{b}}}\bigg|_{\Phi^\star} - G_{\bar{A}\bar{B}} \frac{\partial^2 \mathcal{F}}{\partial \Phi_{\bar{A}} \partial A_{\bar{a}}} \frac{\partial^2 F}{\partial \Phi_{\bar{A}} \partial A_{\bar{b}}}\bigg|_{\Phi^\star}. \tag{5.10}$$

The last equation contains only partial derivatives with respect to the link phases and Hubbard–Stratonovich fields. Computing the partial derivatives of the contribution of the Hubbard–Stratonovich fields to the free energy (4.18) is trivial, but taking the derivatives of $\mathcal{F}_0$ is quite involved.

In Equation (4.17) we have expressed the free energy $\mathcal{F}_0$ as a sum of simple functions $f(\varepsilon_i)$ of the energy levels ε_i of the effective singe-particle Hamiltonian (4.23). In the following we use the finite temperature version of the free energy, where $f(\varepsilon_i) = -T \ln(1 + e^{-\beta \varepsilon_i})$.

The second derivatives of $\mathcal{F}_0$ with respect to some arbitrary parameters ϑ and ζ can be rewritten in terms of derivatives of $\mathcal{F}_0$ with respect to ε_i and derivatives of ε_i with respect to these parameters:

$$\frac{\partial^2 \mathcal{F}_0}{\partial \vartheta \partial \zeta} = \sum_{\varepsilon_i} \left(\frac{\partial^2 f(\varepsilon_i)}{\partial \varepsilon_i^2} \frac{\partial \varepsilon_i}{\partial \vartheta} \frac{\partial \varepsilon_i}{\partial \zeta} + \frac{\partial f(\varepsilon_i)}{\partial \varepsilon_i} \frac{\partial^2 \varepsilon_i}{\partial \vartheta \partial \zeta} \right) \tag{5.11}$$

It is a simple exercise to compute the derivatives of the function f, which are given by

$$\frac{\partial f(\varepsilon_i)}{\partial \varepsilon_i} = \frac{1}{e^{\varepsilon_i \beta} + 1} \quad \text{and} \quad \frac{\partial^2 f(\varepsilon_i)}{\partial \varepsilon_i^2} = \frac{-\beta}{4 \cosh^2(\frac{\beta \varepsilon_i}{2})}. \tag{5.12}$$

However, in the presence of external gauge fields there is no longer a closed analytical expression for the energy levels ε_i. In general, it will not be possible to compute the derivatives of the energy levels analytically.

We are interested in the case where the parameters ϑ and ζ are either link phases or Hubbard–Stratonovich fields. In our approximation the Hubbard–Stratonovich fields and the external gauge fields are static. Hence we can use time independent perturbation theory to approximate the derivatives of the energy levels:

$$\begin{aligned}
\frac{\partial \varepsilon_i}{\partial \vartheta} &\approx \langle \psi_i | \frac{\partial \hat{h}}{\partial \vartheta} | \psi_i \rangle \\
\frac{\partial^2 \varepsilon_i}{\partial \vartheta \partial \zeta} &\approx \langle \psi_i | \frac{\partial^2 \hat{h}}{\partial \vartheta \partial \zeta} | \psi_i \rangle + \sum_{j \neq i} \frac{\langle \psi_i | \frac{\partial \hat{h}}{\partial \vartheta} | \psi_j \rangle \langle \psi_j | \frac{\partial \hat{h}}{\partial \zeta} | \psi_i \rangle}{\varepsilon_i - \varepsilon_j} \\
&\quad + \sum_{j \neq i} \frac{\langle \psi_i | \frac{\partial \hat{h}}{\partial \zeta} | \psi_j \rangle \langle \psi_j | \frac{\partial \hat{h}}{\partial \vartheta} | \psi_i \rangle}{\varepsilon_i - \varepsilon_j},
\end{aligned} \tag{5.13}$$

where $\hat{h}$ is the single-particle Hamiltonian (4.23) and $|\psi_i\rangle$ is the single-particle wave function corresponding to the energy level ε_i. The first line in Equation (5.13) is simply the first order perturbation theory result for the change in the energy ε_i. Taking the derivative of the first line and using first order perturbation theory for the derivatives of the eigenstates gives the second line[1].

1 Compare also Equations (C.5) and (C.9) in Appendix C.

Inserting the expressions (5.13) into Equation (5.11) yields

$$\begin{aligned}\frac{\partial^2 \mathcal{F}_0}{\partial\vartheta\partial\zeta} \approx \sum_i \frac{-\beta}{4\cosh^2(\frac{\varepsilon_i\beta}{2})} \langle\psi_i| \frac{\partial\hat{h}}{\partial\vartheta} |\psi_i\rangle \langle\psi_i| \frac{\partial\hat{h}}{\partial\zeta} |\psi_i\rangle \\ + \sum_i n(\varepsilon_i) \langle\psi_i| \frac{\partial^2\hat{h}}{\partial\vartheta\partial\zeta} |\psi_i\rangle + \sum_{i,j\neq i} n(\varepsilon_i) \frac{\langle\psi_i| \frac{\partial\hat{h}}{\partial\zeta} |\psi_j\rangle \langle\psi_j| \frac{\partial\hat{h}}{\partial\vartheta} |\psi_i\rangle}{\varepsilon_i - \varepsilon_j} \\ + \sum_{i,j\neq i} n(\varepsilon_i) \frac{\langle\psi_i| \frac{\partial\hat{h}}{\partial\vartheta} |\psi_j\rangle \langle\psi_j| \frac{\partial\hat{h}}{\partial\zeta} |\psi_i\rangle}{\varepsilon_i - \varepsilon_j},\end{aligned} \tag{5.14}$$

where $n(\varepsilon_i) := \partial f(\varepsilon_i)/\partial\varepsilon_i$ is the Fermi–Dirac distribution.

We stress again that we are calculating σ_{CME} in the linear response approximation. When we use Equation (5.14) to compute the variation of the free energy in the Kubo formula (5.3), we should therefore work in the limit of vanishing external fields and set all link phases $A_{x,k}$ to zero and the Hubbard–Stratonovich field to its mean-field value $\Phi^\star$. In this work we consider only the case of a homogeneous and isotropic Hubbard–Stratonovich field. Under this assumption the eigenstates of the effective single-particle Hamiltonian (4.23) can be found analytically and the calculation of the partial derivatives of the free energy in Equation (5.10) (5.14) is straightforward.

5.1.1 *Explicit Expressions for the Second Variations of the Free Energy*

For completeness we derive analytical expressions for the eigenstates of the effective-single particle Hamiltonian and briefly discuss the numerical implementation of the second derivatives of the free energy.

In the absence of external gauge fields the momentum-space form of the Hamiltonian (4.23) is given by

$$\hat{h}(k) = \sum_{i=1}^{3} \alpha_i \sin(k_i) + 2\gamma_0 \sum_{i=1}^{3} \sin^2(k_i/2) + \gamma_0 m_r + i\gamma_0\gamma_5 m_i + \gamma_5\mu_A. \tag{5.15}$$

The eigenvalues of this Hamiltonian are given by Equation (4.27) and have already been used to find the mean-field values of m_r, m_i and μ_A. The eigenstates are given by

$$\varphi_{s,\sigma}(\vec{k}) = \begin{pmatrix} \sqrt{\frac{1}{2} + \frac{\sigma S - \mu_A}{2\varepsilon_{s,\sigma}}}\,\eta_\sigma \\ s\frac{W + m_r - i m_i}{|W + m_r + i m_i|}\sqrt{\frac{1}{2} - \frac{\sigma S - \mu_A}{2\varepsilon_{s,\sigma}}}\,\eta_\sigma \end{pmatrix}, \tag{5.16}$$

where W and S are the short-hand notations defined after Equation (4.27) and η_σ is the eigenstate of the operator $\sigma_i \sin(k_i)$ corresponding to the eigenvalue σS. The normalised Bloch functions have the form

$$\Psi_x^{s,\sigma}(\vec{k}) = \varphi_{s,\sigma}(\vec{k}) \frac{e^{i\vec{k}\cdot\vec{x}}}{\sqrt{L_S^3}}. \tag{5.17}$$

If we restore the explicit dependence of the free energy on all indices Equation (5.14) reads as

$$\begin{aligned}\frac{\partial^2 \mathcal{F}_0}{\partial\vartheta\partial\zeta} \approx &\sum_{s,\sigma,\vec{p}} n(\varepsilon_{s,\sigma}(\vec{p}))\,\langle s,\sigma,\vec{p}|\,\frac{\partial^2\hat{h}}{\partial\vartheta\partial\zeta}\,|s,\sigma,\vec{p}\rangle \\ &- \sum_{\substack{s,\sigma,\vec{p}\\ \bar{s},\bar{\sigma},\vec{q}}} \frac{\beta}{4\cosh^2\left(\frac{\varepsilon_{s,\sigma}(\vec{p})\beta}{2}\right)}\,\langle s,\sigma,\vec{p}|\,\frac{\partial\hat{h}}{\partial\vartheta}\,|s,\sigma,\vec{p}\rangle\,\langle s,\sigma,\vec{p}|\,\frac{\partial\hat{h}}{\partial\zeta}\,|s,\sigma,\vec{p}\rangle \\ &+ \sum_{\substack{s,\sigma,\vec{p}\\ \bar{s},\bar{\sigma},\vec{q}}} (n(\varepsilon_{s,\sigma}(\vec{p}) - n(\varepsilon_{\bar{s},\bar{\sigma}}(\vec{q})) \\ &\qquad \times \frac{\langle s,\sigma,\vec{p}|\,\frac{\partial\hat{h}}{\partial\zeta}\,|\bar{s},\bar{\sigma},\vec{q}\rangle\,\langle\bar{s},\bar{\sigma},\vec{q}|\,\frac{\partial\hat{h}}{\partial\vartheta}\,|s,\sigma,\vec{p}\rangle}{\varepsilon_{s,\sigma}(\vec{p}) - \varepsilon_{\bar{s},\bar{\sigma}}(\vec{q})},\end{aligned} \tag{5.18}$$

where the sum is over $s,\bar{s} = \pm 1$, $\sigma,\bar{\sigma} = \pm 1$ and over all vectors $\vec{p},\vec{q}$ in the Brillouin zone and we have introduced the bra-ket–notation

$$\langle s,\sigma,\vec{p}|\,\hat{O}\,|\bar{s},\bar{\sigma},\vec{q}\rangle = \sum_{x,y} \Psi^{\dagger\,s,\sigma}_x(\vec{p})\hat{O}_{xy}\Psi^{\bar{s},\bar{\sigma}}_y(\vec{q}). \tag{5.19}$$

The first derivatives of the position-space single-particle Hamiltonian (4.23) with respect to the link phases and Hubbard–Stratonovich field components are given by

$$\begin{aligned}\left.\frac{\partial\hat{h}_{xy}}{\partial A_{z,i}}\right|_{A=0} &= P_+\delta_{z+\hat{i},x}\delta_{z,y} + P_-\delta_{z,x}\delta_{z+\hat{i},y} \qquad \text{and} \\ \left.\frac{\partial\hat{h}_{xy}}{\partial\Phi_{z,A}}\right|_{\Phi=\Phi^\star} &= \delta_{z,x}\delta_{z,y}\Gamma_A,\end{aligned} \tag{5.20}$$

with the definition $P_\pm = \frac{\alpha_i \pm i\gamma_0}{2}$. The mixed second derivatives with respect to one link phase and one Hubbard–Stratonovich field component are zero. The Hamiltonian depends linearly on Φ_x and thus the second derivatives with respect to the Hubbard–Stratonovich field components are also zero. The only second derivative that does not vanish is

$$\left.\frac{\partial^2\hat{h}_{xy}}{\partial A_{z,i}\partial A_{\bar{z},j}}\right|_{A=0} = i\delta_{z,\bar{z}}\delta_{i,j}(P_-\delta_{z,x}\delta_{z+\hat{i},y} - P_+\delta_{z+\hat{i},x}\delta_{z,y}). \tag{5.21}$$

With the explicit formulae for the derivatives (5.20) and (5.21) to rewrite the matrix elements in Equation (5.18) as

$$\langle s,\sigma,\vec{p}|\,\frac{\partial\hat{h}}{\partial A_{z,i}}\,|\bar{s},\bar{\sigma},\vec{q}\rangle = \bar{\varphi}_{s,\sigma}(\vec{p})\hat{j}_i\varphi_{\bar{s},\bar{\sigma}}(\vec{q})\frac{e^{-i(\vec{p}-\vec{q})\cdot\vec{z}}}{L_S^3}, \tag{5.22}$$

$$\langle s,\sigma,\vec{p}|\,\frac{\partial\hat{h}}{\partial\Phi_{z,A}}\,|\bar{s},\bar{\sigma},\vec{q}\rangle = \bar{\varphi}_{s,\sigma}(\vec{p})\Gamma_A\varphi_{\bar{s},\bar{\sigma}}(\vec{q})\frac{e^{-i(\vec{p}-\vec{q})\cdot\vec{z}}}{L_S^3}, \tag{5.23}$$

$$\langle s,\sigma,\vec{p}|\,\frac{\partial\hat{h}}{\partial A_{z,i}\partial A_{\bar{z},j}}\,|s,\sigma,\vec{p}\rangle = \bar{\varphi}_{s,\sigma}(\vec{p})\frac{\partial\hat{j}_i}{\partial A_j}\varphi_{s,\sigma}(\vec{p})\frac{\delta_{z,\bar{z}}}{L_S^3}, \tag{5.24}$$

where we define

$$\hat{j}_i\big|_{A=0} := P_+ e^{-ip_i} + P_- e^{iq_i}, \tag{5.25}$$

$$\frac{\partial \hat{j}_i}{\partial A_j}\Big|_{A=0} := i\delta_{i,j}(P_- e^{ip_i} - P_+ e^{-ip_i}). \tag{5.26}$$

Let us consider the partial derivative $\partial^2\mathcal{F}_0/\partial A_i \partial A_j$ as an example of how the terms in Equation (5.10) can be evaluated numerically. By plugging the expressions (5.22) and (5.24) into Equation (5.18) and performing the lattice Fourier transformation with respect to z and $\bar{z}$, i.e.

$$\frac{\partial^2\mathcal{F}_0}{\partial A_i \partial A_j}(\vec{k}) = \frac{1}{L_S^3}\sum_{z,\bar{z}} e^{i\vec{k}(\vec{z}-\vec{\bar{z}})}\frac{\partial^2\mathcal{F}_0}{\partial A_i \partial A_j}(z,\bar{z}), \tag{5.27}$$

we finally arrive at an expression that can be summed up numerically in a straightforward way:

$$\begin{aligned} L_S^3\frac{\partial^2\mathcal{F}_0}{\partial A_i \partial A_j}(\vec{k}) = \sum_{s,\sigma}\sum_{\vec{p}}\Bigg[& n(\varepsilon_{s,\sigma}(\vec{p}))\bar{\varphi}_{s,\sigma}(\vec{p})\frac{\partial j_i}{\partial A_j}\varphi_{s,\sigma}(\vec{p}) \\ & - \delta_{\vec{k},0}\beta\frac{\bar{\varphi}_{s,\sigma}(\vec{p})j_i\varphi_{s,\sigma}(\vec{p})\bar{\varphi}_{s,\sigma}(\vec{p})j_j\varphi_{s,\sigma}(\vec{p})}{4\cosh^2(\frac{\beta\varepsilon_{s,\sigma}}{2})} \\ & + \sum_{\bar{s},\bar{\sigma}}\frac{\bar{\varphi}_{s,\sigma}(\vec{p})j_i\varphi_{\bar{s},\bar{\sigma}}(\vec{q})\bar{\varphi}_{\bar{s},\bar{\sigma}}(\vec{q})j_j\varphi_{s,\sigma}(\vec{p})}{\varepsilon_{s,\sigma}(\vec{p}-\varepsilon_{\bar{s},\bar{\sigma}}(\vec{q})} \\ & \times (n(\varepsilon_{s,\sigma}(\vec{p}) - n(\varepsilon_{\bar{s},\bar{\sigma}}(\vec{q}))\Bigg], \end{aligned} \tag{5.28}$$

where we have already performed the lattice Fourier transform, $\vec{q}$ is fixed to $\vec{q} = \vec{p} + \vec{k}$ and we sum over all momenta $\vec{p}$ in the Brillouin zone. Analogous expressions can be derived for the partial derivatives $\partial^2\mathcal{F}_0/\partial A_i \partial \Phi_A$ and $\partial^2\mathcal{F}_0/\partial\Phi_A\partial\Phi_B$.

5.2 MEAN-FIELD RESULTS FOR THE STATIC CHRIAL MAGNETIC CONDUCTIVITY

After finding the renormalised values of m_r, m_i and μ_A by minimising the mean-field free energy (4.26), the chiral magnetic conductivity $\sigma_{CME}(\vec{k})$ can be computed with the Kubo formula (5.3) by using the approach outlined in the last section to evaluate the second variation of the free energy given by Equation (5.10).

In Figure 5.1 σ_{CME} is plotted as a function of the wave vector $\vec{k}$ of the external magnetic field. The wave vector $\vec{k}$ of the modulation of the external magnetic field is chosen to be parallel to the third coordinate axis, i.e. $\vec{k} = k\vec{e}_3$. The bare chiral chemical potential is fixed to $\mu_A^0 = 0.05$ and $L_S = 50$ for all the plots in Figure 5.1. As we have discussed in Section 4.5, gapless modes in our model can only exist along lines with constant renormalised mass $m_r = 0, -2, -4, -6$. Strictly speaking it is only for these characteristic values of m_r that our model describes a Weyl semimetal. In Figure 5.1 we thus focus on the values $m_r = 0.00, -2.00, -4.00$. To study the effects of a finite Fermion mass we also include the value $m_r = -2.20$. Remember that for $m_r = 0, -6$ the spectrum of our model contains one Dirac cone and $N_f = 3$ Dirac cones for $m_r = -2, -4$. This can be seen by comparing the plots for $m_r = 0.0$ and $m_r = -4.0$, where the linear scaling of $\sigma_{CME}(\vec{k})$ with N_f is obvious.

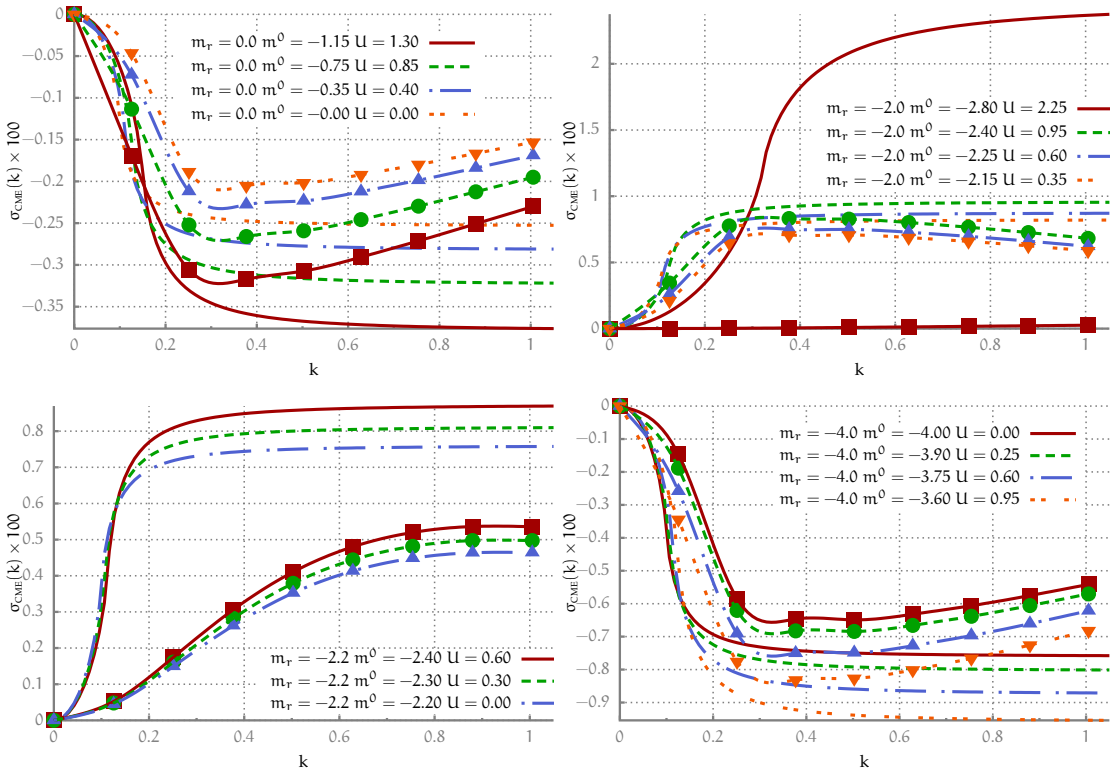

Figure 5.1: Numerical results for the chiral magnetic conductivity σ_{CME} at fixed, characteristic values of the renormalised mass m_r for different values of the inter-fermion interaction potential U (lines with symbols). $L_S = 50$ and $\mu_A^0 = 0.05$ in all plots. Clockwise from top left: $m_r = 0.00$,$m_r = -2.00$, $m_r = -4.00$ and $m_r = -2.20$. The lines without symbols mark the result (5.29) for free continuum fermions with Pauli–Villars regularisation evaluated at the renormalised chiral chemical potential μ_A. Within each plot corresponding curves for the continuum result and our model are plotted in the same style.

Additionally, we find that in our model the renormalised masses m_r and $-6 - m_r$ are equivalent, but the roles of the left- and right-handed spinor components are interchanged for the two renormalised mass values: Changing the mass from m_r to $-6 - m_r$ in our model is effectively equivalent to changing the sign of the chiral chemical potential. A clear signature of this behaviour can be seen in our plots, where the chiral magnetic conductivity for $m_r = -2.0$ and $m_r = -4.0$ at the same U differs only by a minus sign. Consequently the chiral magnetic conductivity exactly vanishes for any value of the wave vector $\vec{k}$ on the line of fixed $m_r = -3$, which is the symmetry axis of the phase diagram of our model.

Taking the phase structure of our model and the number of Dirac cones in the spectrum into account, we find a qualitative agreement between our data outside the Aoki phase at small wave vectors $\vec{k}$ and the continuum results for $\sigma_{CME}(\vec{k})$ obtained with Pauli–Villars regularisation [13, 73]:

$$\sigma_{CME}^{PV} = \frac{N_r}{(2\pi)^2}\left(\mu_A + \frac{\mu_A^2 - k^2/4}{k}\ln\left|\frac{2\mu_A - k}{2\mu_A + k}\right|\right) \tag{5.29}$$

The sudden growth of the chiral magnetic conductivity around $k = 2\mu_A$, a characteristic feature of Equation (5.29), is also clearly visible for the lattice model results.

Furthermore, we find that at some value of $k > 2\mu_A$ our results come close to the asymptotic value $\pm\frac{\mu_A}{2\pi^2}$ of the continuum result. At large values of k our data shows a decrease of $\sigma_{CME}(k)$ and not a saturation like in the continuum. This is to be expected, because in our model chiral symmetry is explicitly broken for large k by the Wilson term.

We emphasise that $\sigma_{CME}(k)$ depends on the renormalised chiral chemical potential μ_A, which is measurable in experiments and not on the bare value μ_A^0. The chiral chemical potential in WSMs can be measured, for example, in angular resolved photoemission spectroscopy (ARPES) experiments [101] and such experiments will yield the renormalised value of μ_A. To compare our data with the continuum result (5.29) we therefore use the renormalised chiral chemical potential.

For all the plots in Figure 5.1 the lattice result for $\sigma_{CME}(k)$ is smaller than the continuum result (5.29) evaluated at the renormalised chiral chemical potential. We therefore conclude that the observed enhancement of $\sigma_{CME}(k)$ with increased interaction potential U is mainly caused by the strong renormalisation of the chiral chemical potential.

In the Aoki phase, where the effective single-particle Hamiltonian is gapped because the $\mathcal{CP}$-breaking mass term m_i becomes finite, $\sigma_{CME}(k)$ is suppressed for all values of k. This is illustrated by the plot in the top right of Figure 5.1. At $U = 2.25$ we are deep in the Aoki phase for a bare mass of $m^0 = -2.80$ (compare Figure 4.2) and $\sigma_{CME}(k)$ is approximately zero. Note that this is not caused by a small renormalised chemical potential. On the contrary, μ_A as a function of U in general grows faster in the Aoki phase as is evident from Figure 4.3b and also from the continuum result in Figure 5.1.

Away from the characteristic mass values $m_r = 0, -2, -4, -6$ the single-particle Hamiltonian is also gapped outside of the Aoki phase. In the top left of Figure 5.1 we show results for $\sigma_{CME}(k)$ at fixed $m_r = -2.20$. In qualitative agreement with expectations from continuum calculations [13, 73] the chiral magnetic conductivity is strongly suppressed.

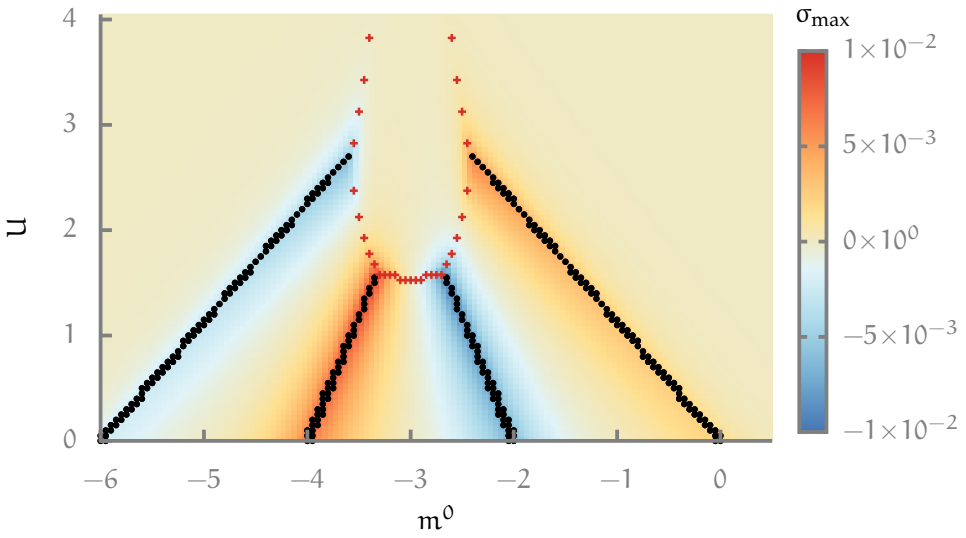

Figure 5.2: Estimate σ_{max} of the asymptotic value of $\sigma_{CME}(k)$ at $\mu_A \ll k \ll 1$ in the m^0-U–plane at fixed bare chiral chemical potential $\mu_A^0 = 0.05$. The red crosses mark the boarder of the Aoki phase and the black dots denote the lines of constant $m_r = 0, -2, -4, -6$.

So far we have only presented results for some specific points in the phase diagram. To study the behaviour of the chiral magnetic conductivity throughout the whole phase diagram it is convenient to characterise $\sigma_{\mathrm{CME}}(k)$ by a single value. A choice that suggests itself is the asymptotic value of $\sigma_{\mathrm{CME}}(k)$ at $\mu_A \ll k \ll 1$. For this range of momenta the lattice value of $\sigma_{\mathrm{CME}}(k)$ should be a good approximation to the continuum value, which approaches the asymptotic value $\frac{N_f \mu_A}{2\pi^2}$ for $k \ll \mu_A$ (compare Figure 5.1). This asymptotic value is – in a highly non-trivial way [13] – related to the anomaly coefficient and is therefore universal.

On a lattice with finite spacial extend the number of (quantised) momenta in the range $\mu_A \ll k \ll 1$ is finite. In particular, for $L_s = 50$ the number of lattice momenta for which it is reasonable to compare $\sigma_{\mathrm{CME}}(k)$ with the universal value $\frac{N_f \mu_A}{2\pi^2}$ is quite small. The numerical cost of our calculation scales like L_s^3 and it is not feasible to increase L_s in order to have more lattice momenta in a given range. Thus we decided to estimate the asymptotic value at $\mu_A \ll k \ll 1$ simply as the one where the absolute value of $\sigma_{\mathrm{CME}}(k)$ among all lattice momenta is maximal. We define this estimate as

$$\sigma_{\mathrm{max}} := \pm \max_k |\sigma_{\mathrm{CME}}(k)|, \tag{5.30}$$

where the appropriate sign has to be chosen.

Characterising the chiral magnetic conductivity by a single scalar value makes it much simpler to visualise its qualitative behaviour. In Figure 5.2 we plot σ_{max} as a function of the bare mass m^0 and the interaction potential U at fixed $\mu_A^0 = 0.05$. We find that σ_{max} is peaked around the lines of constant bare mass $m_r = 0, -2, -4, -6$, where our model harbours massless excitations. In the Aoki phase with broken $\mathcal{CP}$-symmetry σ_{max} is strongly suppressed and quickly decreases away from the phase boundary. The dependence on σ_{max} on U and m^0 is non-trivial and depending on the value of m^0 increasing U can lead to an increase or decrease of σ_{max}.

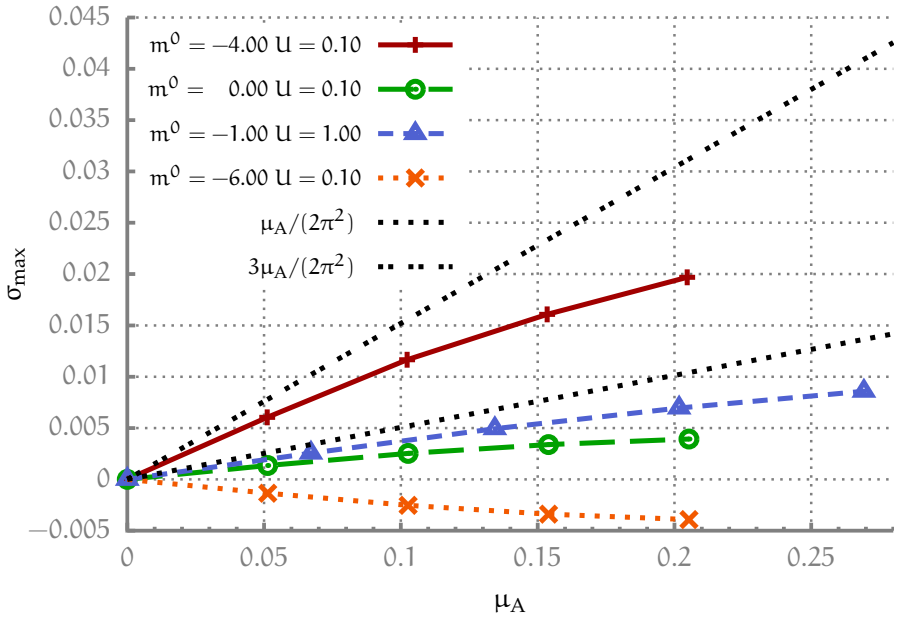

Figure 5.3: Dependence of σ_{max} on the renormalised chiral chemical potential μ_A for different points in the m^0-U–plane. The points are connected with straight lines to guide the eye.

To compare the results for σ_{max} with the universal value $\frac{\mu_A}{2\pi^2}$ in the result for free continuum fermions (4.2), we assume that σ_{max} is a linear function of the renormalised chiral chemical potential μ_A. Figure 5.3, where σ_{max} is plotted as a function of μ_A for different sets of parameters, supports this assumption.

We can therefore estimate the ratio of the asymptotic value σ_{max} over the renormalised chiral chemical potential μ_A by fitting $\sigma_{max}(\mu_A)$ to a one parameter linear function:

$$\sigma_{CME}(\mu_A) = \kappa\mu_A. \tag{5.31}$$

The fit parameter κ is precisely the ratio we are interested in. Figure 5.4 shows the results for the fit parameter $\kappa = \sigma_{CME}/\mu_A$ fitting as a function of the bare mass m^0 and the inter-electron interaction potential U. For the fits we used three data points at bare chiral chemical potential $\mu_A^0 = 0.05, 0.10, 0.15$, where $\sigma_{max}(\mu_A)$ is well approximated by a linear function. Like σ_{max} itself the ratio σ_{CME}/μ_A has peaks along the lines of constant renormalised mass $m_r = 0.0, -2-0, -4.0-6.0$ and is very small in the Aoki phase. Even the peak value of σ_{CME}/μ_A in the vicinity of the lines with $N_f = 3$ or $N_f = 1$ Dirac cones in the energy spectrum never exceeds the universal value $N_f\mu_A/(2\pi^2)$. In stark contrast to the results for model calculations with interacting continuum Dirac fermions, where a strong enhancement of σ_{CME} has been observed in the phase with broken chiral symmetry [14], we find that σ_{CME} becomes very small in the Aoki phase.

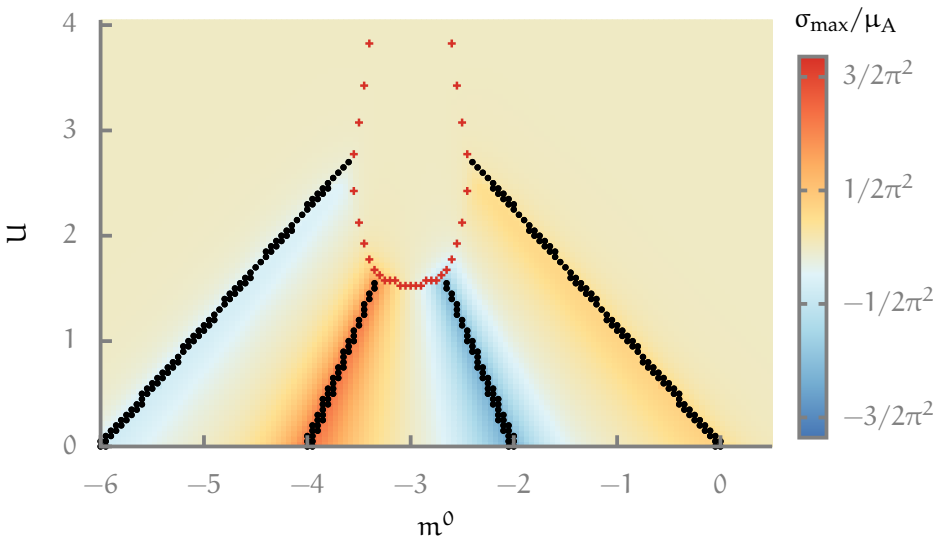

Figure 5.4: Ratio of the estimated asymptotic value σ_{max} of $\sigma_{CME}(k)$ at $\mu_A \ll k \ll 1$ to the renormalised chiral chemical potential μ_A. The black dots mark the lines of constant renormalised mass $m_r = -6, -4, -2, 0$ and the red crosses indicate the border of the Aoki phase for $\mu_A = 0.0$.

To better understand the influence of inter-electron interactions on the chiral magnetic conductivity let us have a closer look at the second variation of the free energy (5.10), which enters the Kubo formula (5.3). The first term on the right hand side of Equation (5.10) is given by the partial derivatives of $\mathcal{F}$ with respect to the link phases and describes the electromagnetic response of the non-interacting system with the renormalised singe-particle Hamiltonian (4.23). In an experiment the renormalised and not the

bare parameters are the physical observables. The first term does therefore not really capture the effects of inter-electron interactions. The second term in Equation (5.10), on the other hand, describes the non-trivial contributions to the variation of the free energy due to the interactions. It has been shown in [14] that this term can be interpreted as an infinite sum of ladder diagrams in the weak-coupling regime.

In summary the first (tree-level) term in the variation of the free energy includes the change of the linear electromagnetic response due to a renormalisation of the model parameters m_r,m_i, μ_A^0 and the second term describes non-trivial loop corrections corresponding to ladder diagrams with an arbitrary number of fermionic loops.

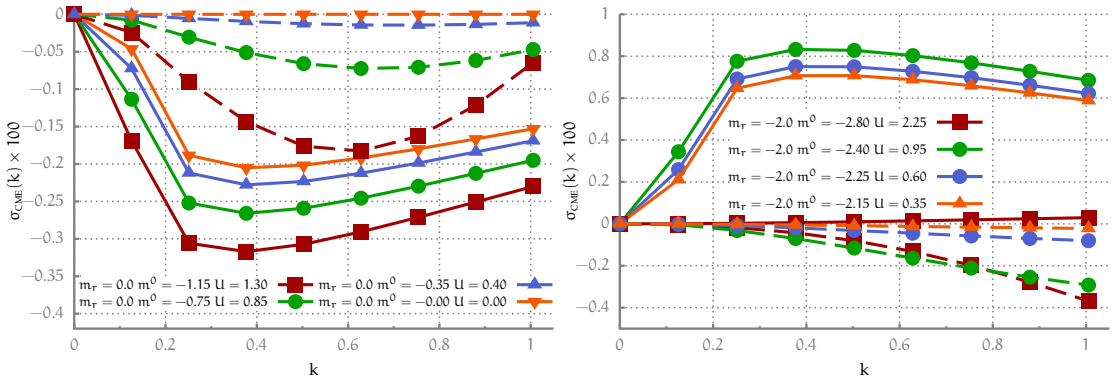

Figure 5.5: Relative importance of the two contributions to the chiral magnetic conductivity. Solid lines with symbols mark the tree-level contributions to $\sigma_{CME}(k)$ (first term in (5.10)) and dashed lines the contribution of the loop diagrams (second term in (5.10)). Curves with the same symbol are evaluated for the same set of parameters. To fit both contributions on the same plot the (very small) contributions of loop diagrams are multiplied by a factor 10^4 ($m_r = 0.0$) or 10^2 ($m_r = -2, 0$). The bare chiral chemical potential is fixed to $\mu_A^0 = 0.15$ in all plots.

In Figure 5.5 we separately plot the tree-level and the loop-diagram contributions to the chiral magnetic conductivity $\sigma_{CME}(k)$ for fixed bare chiral chemical potential $\mu_A^0 = 0.15$. The loop contributions turn out to be orders of magnitude smaller than the tree-level contributions in the $\mathcal{CP}$-symmetric phase. For a bare mass $m^0 = -2.0$ the loop corrections are approximately 100 times smaller and for $m^0 = -0.0$ they are even 10^4 times smaller than the tree-level contributions. In the Aoki phase the situation is different. As we have seen $\sigma_{CME}(k)$ is strongly suppressed if $m_i \neq 0$. The point with $m_r = -2.0$ and $U = 2.25$ lies deep in the Aoki phase and the tree-level contribution becomes very small. The contribution from the loop-diagrams on the other hand has roughly the same value it had outside of the Aoki phase and hence the two contributions now have roughly the same magnitude.

It is interesting to check if the results for the few specific points in Figure 5.5 are representative and hold for all points in the phase diagram. To this end we look at the absolute value of the ratio of the tree-level and the loop contributions to the chiral magnetic conductivity. In Figure 5.6 we plot this ratio for different fixed lattice momenta k and fixed $\mu_A^0 = 0.05$ as a function of m^0 and U.

While there clearly is a strong k dependence in the plots, the general qualitative features are independent of the lattice momentum k. Outside of the Aoki phase the loop contributions are in general very small. In particular, close to the lines of fixed renor-

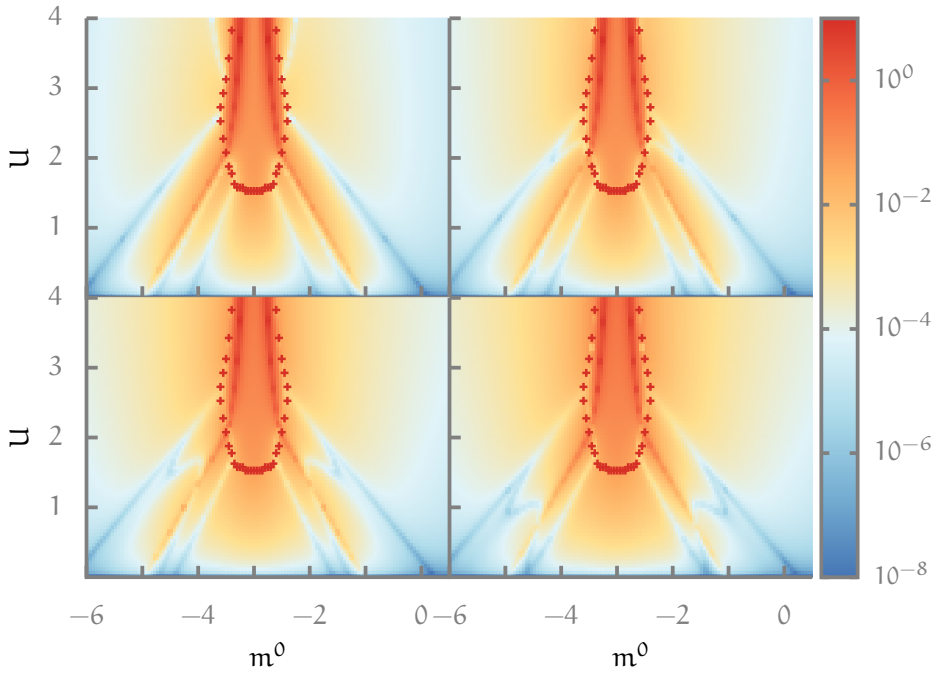

Figure 5.6: Absolute value of the ratio of the loop over the tree-level contributions to the chiral magnetic conductivity. The ratio is ploted in the m^0-U–plane for fixed values of the lattice momentum k. Clockwise from top left $k = 2, 4, 8, 6 \times 2\pi/L_s$. Red crosses mark the boarder of the Aoki phase. In all plots $\mu_A^0 = 0.05$.

malised mass $m_r = 0, -2, -4, -6$ the loop contributions are negligible compared to the tree-level contributions. The exception are the lines of renormalised mass $m_r = -1, -5$, where the loop contributions are comparable to the tree-level contributions. In the Aoki phase however, the two contributions to σ_{CME} are roughly of the same order of magnitude. We emphasise that the reason for this is the strong suppression of the tree-level contribution in the Aoki phase and not a growth of the loop contribution.

In general, we observe that the relative importance of the tree-level and loop contributions has a highly non-trivial dependence on m^0 and U. Moreover, the ratio strongly depends on the wave vector $\vec{k}$ of the modulation of the external magnetic field.

5.2.1 *Chiral Magnetic Conductivity at Finite Temperature*

In the derivation of the equation for the second variation of the free energy we have not used the limit $T \to 0$ and it is straight forward to compute $\sigma_{CME}(k)$ at finite temperatures. We observe that finite temperature suppresses the chiral magnetic conductivity for all points in the parameter space. As an example Figure 5.7 shows the temperature dependence of $\sigma_{CME}(k)$ for points with renormalised mass $m_r = -2, 2.2$ and fixed bare chiral chemical potential $\mu_A^0 = 0.15$.

The suppression of $\sigma_{CME}(k)$ is relatively small as long as the temperature is smaller than or comparable to the chiral chemical potential μ_A. At higher temperatures, on the other hand, $\sigma_{CME}(k)$ is strongly suppressed and vanishes for $T \gg \mu_A$. This temperature dependence can be explained with a simple physical argument: A temperature that is large compared to the chiral chemical potential tends to reduce the difference in the occupation numbers of left- and right-handed fermions with a given momentum. It is

also easy to see that the fermionic free energy (4.20) (and therefore also the second variation (5.14) of the free energy) becomes independent of μ_A in the limit $T \to \infty$. Consequently the chiral magnetic conductivity $\sigma_{CME}(k)$ has to vanish in the infinite temperature limit.

As was mentioned above, transport experiments with WSMs are typically performed at temperatures below or around 10K. A temperature of 10K correspond to an energy of approximately 1meV. From our results we conclude that in order to be able to measure σ_{CME} in a experiment the (renormalised) chiral chemical potential in the sample WSM should not be smaller than 1meV.

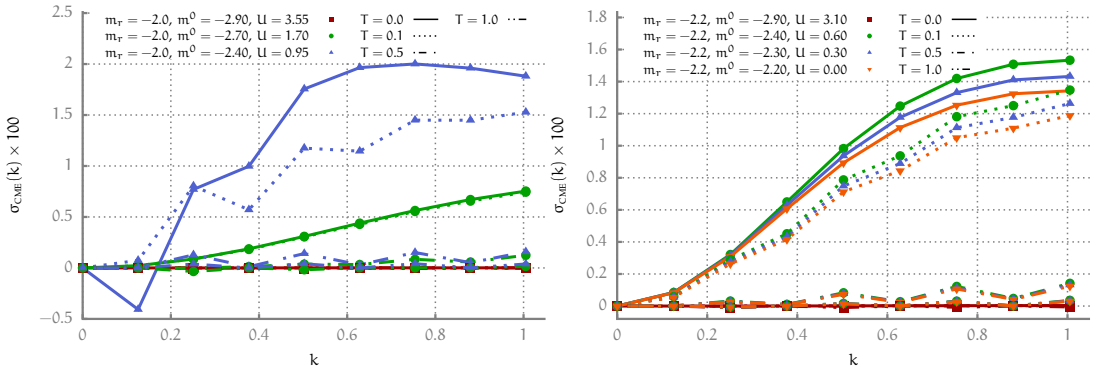

Figure 5.7: Finite temperature results for $\sigma_{CME}(k)$. Different symbols mark different sets of the model parameters U and m_r and line styles denote different values of the temperature. The bare chiral chemical potential is $\mu_A^0 = 0.15$ in both plots.

5.3 CONNECTION TO EXPERIMENT

From a theoretical viewpoint spatially modulated magnetic fields are a convenient approach to study the chiral magnetic effect. The use of spatially inhomogeneous magnetic fields allows, for example, to relate the chiral magnetic conductivity to the anomaly coefficient in the limit of large k [13]. In experiments, on the other hand, one typically works with static and homogeneous magnetic fields. All our calculations clearly show that $\sigma_{CME}(k)$ vanishes in the limit $k \to 0$, in agreement with [72]. The vanishing of the chiral magnetic conductivity for $k \to 0$ raises the question how the chiral magnetic effect can be observed in a realistic experimental setup with a constant magnetic field.

The WSM samples that are used in experiments have a finite size and the smallest side length is of order 1 mm [6, 60–62]. One can expect that the magnetic fields in an experiment have a spatial modulation with a characteristic wavelength of the same order, or even smaller if the inhomogeneities and defects in real crystals are taken into account.

So far all our calculations have been performed for a finite crystal lattice with periodic boundary conditions. In this section we study the possible effects of boundaries on the chiral magnetic conductivity in WSM.

5.3.1 *Linear Response Analysis*

The static Kubo Equation (5.3) is based on approximations and idealisations and will in general not take into account all the relevant details of realistic experiments. Neverthe-

less, we will argue in the following that our results can provide a reasonable order of magnitude estimate for the effect sizes one can expect in an experiment.

We have found that outside of the Aoki phase and for small momenta our results are in good agreement with the expression (5.29), which has been derived for continuum Dirac fermions in infinite space using Pauli–Villars regularisation. To model the spatial inhomogeneities of the magnetic field related to the finite sample size in a way that is consistent with the approximations we have used in this work, we consider the case of a magnetic field that is static and constant inside a finite region of space and vanishes outside of this region. To simplify the calculations we assume that the field has the form of the magnetic field of an infinitely long solenoid with radius R that points in the x_3 direction. The magnetic field is then constant inside the solenoid, parallel to the x_3 axis and vanishes outside of the solenoid, i.e.:

$$\vec{B}(x_1, x_2, x_3) = B^0 \Theta\left(R - \sqrt{x_1^2 + x_2^2}\right) \vec{e}_3, \tag{5.32}$$

with the magnetic field strength B^0, the unit vector parallel to the third coordinate axis $\vec{e}_3$ and the Heaviside step function (4.21). The Fourier transform of the magnetic field (5.32) can be evaluated analytically and its third component reads as

$$\tilde{B}_3(\vec{k}) = B^0 R^2 \sqrt{\frac{\pi}{2}} \delta(k_3)\ {}_0F_1\left(2; -\frac{1}{4}(k_1^2 + k_2^2)R^2\right), \tag{5.33}$$

where ${}_0F_1$ is a generalised hypergeometric function [102].

Using the linear response relation (5.2) and the Kubo formula (5.3), we find that the Fourier transform of the third component of the electric current is given by

$$\tilde{j}_3(\vec{k}) = \sigma_{\text{CME}}(\vec{k}) \tilde{B}_3(\vec{k}). \tag{5.34}$$

To compute a qualitative estimate of the electric current, we simply use the continuum expression (5.29) for $\sigma_{\text{CME}}(\vec{k})$, since it describes our numerical data in the $\mathcal{CP}$-symmetric phase quite well (compare Figure 5.1).

For a comparison with experimental results it is advantageous to calculate the coordinate space current $j_3(\vec{x})$. There is no analytic expression for the inverse Fourier transform of (5.34), but it is straightforward to calculate it numerically. The magnetic field configuration (5.32) has a cylindrical symmetry and the current $j_3(\vec{x}) = j_3(\rho)$ depends only on the radial coordinate $\rho = \sqrt{x_1^2 + x_2^2}$ and the free parameters R,μ_A and B^0. The magnetic field strength simply enters the final result as multiplicative factor, but $j_3(\rho)$ is a non-trivial function of the parameters R and μ. The current $j_3(\rho)$ at fixed μ_A for different values of the dimensionless product $R\mu_A$ is plotted in Figure 5.8. If $R\mu_A$ is small the current inside the solenoid is almost constant and its magnitude is close to $\frac{\mu_A B^0}{2\pi^2}$ and in agreement with the universal value (4.2). As $R\mu_A$ is increased the current develops a stronger dependence on the coordinate ρ and assumes its maximum close to the boundary of the solenoid. The total current through the plane perpendicular to the solenoid axis is proportional to $\sigma_{\text{CME}}(\vec{k} \to 0)$, which follows immediately if we sum over x_1 and x_2 in the inverse Fourier transform of (5.34). Consequently the total current through the x_1-x_2-plane vanishes identically and the current inside the solenoid is compensated by a current density of opposite sign outside of the solenoid.

We can use experimental data to find an estimate for μ_A in typical experiments. In [6] a good description of the experimental data has been achieved under the assumption

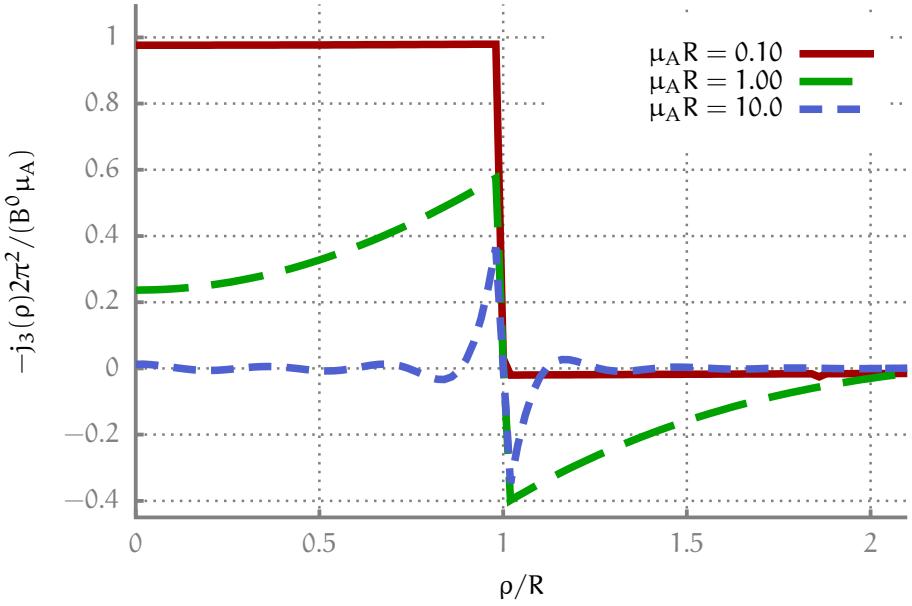

Figure 5.8: Electric current density $j_3(\rho)$ parallel to the magnetic field as a function of the radial coordinate ρ for different values of the dimensionless quantity $R\mu_A$. To make a comparison with the universal value (4.2) easier, we divide the current density by $\frac{\mu_A B^0}{2\pi^2}$.

$\mu_A \ll \mu$ and the chemical potential has been found to be roughly $\mu \sim 100\text{meV}$. We can hence assume that the chiral chemical potential is not bigger than $\mu_A \sim 10\text{meV}$. The results plotted in Figure 5.8 suggest that one should have $R\mu_A \lesssim 1$ in order to observe a strong chiral magnetic current inside the sample. This means that the sample size (in the directions perpendicular to the magnetic field) has to be of order $R \sim 10^2\ \text{meV}^{-1}$. If we translate this to MKS units we find $R \sim 10^{-2}$ mm. Considering that characteristic sample sizes for WSMs are of order 1 mm and that there are possible inhomogeneities and crystal defects, this seems to be a reasonable estimate. A direct comparison of our results with the experimental data in [6] is unfortunately not possible. The electric field strength inside the sample has not been reported and we cannot use Equation (4.3) to find an estimate for the stationary value of μ_A.

An interesting consequence of the dependence of $j_3(\rho)$ on the product $R\mu_A$ is that the chiral magnetic current gets a non-linear dependence on the electric field via Equation (4.3). For small electric fields the stationary value of μ_A and therefore the product $R\mu_A$ are small and $j_3(\rho)$ should be close to the universal value given by (4.2). As the electric field strength and therefore μ_A is increased, the chiral magnetic current is no longer homogeneous inside the sample and moreover the conductivity parallel to the magnetic field should decrease.

5.3.2 *Finite Size Samples of a Non-Interacting Weyl Semimetal*

The simple analysis in the previous subsection clearly shows that finite size effects can have a huge influence on the chiral magnetic conductivity in Weyl semimetals. Moreover, the role of boundaries has been investigated recently in [103], where it has been demon-

strated that in a WSM sample with slab geometry σ_{CME} vanishes for an external magnetic field that is perpendicular to the slab boundaries.

In the following we will study the other limiting case and consider a non-interacting WSM slab subjected to a magnetic field *parallel* to the slab boundaries. To this end we again consider the lattice Wilson-Dirac Hamiltonian. We choose open boundary conditions at $x_3 = 0$ and $x_3 = L_3$. In x_1 and x_2 direction the sample is infinite. The single-particle Hamiltonian is again given by Equation (4.6), but we have to modify the lattice discretisations (4.7) of the derivative and the Laplace operator to take the boundary into account:

$$\begin{aligned}\nabla_{k,xy} &= \frac{1}{2}\left(\Theta(L_3 - x_3 - 1)e^{iA_{x,k}}\delta_{x+\hat{k},y} - \Theta(x_3)e^{-iA_{x-\hat{k},k}}\delta_{x-\hat{k},y}\right) \quad \text{and} \\ \Delta_{xy} &= \sum_{k=1}^{3}\left(2\delta_{x,y} - \Theta(L_3 - x_3 - 1)e^{iA_{x,k}}\delta_{x+\hat{k},y} - \Theta(x_3)e^{-iA_{x-\hat{k},k}}\delta_{x-\hat{k},y}\right).\end{aligned} \tag{5.35}$$

The external magnetic field is chosen to be parallel to the x_1 direction. We use a gauge that preserves the translation symmetry in x_1 and x_2, such that the vector potential is given by $\vec{A} = (0, -Bx_3, 0)^T$. The current density operator is also modified because of the boundaries and reads as

$$j_{x_i}(z) = \frac{\partial \hat{h}_{xy}}{\partial A_{z,i}} = P_+\Theta(z_3)e^{-iA_{z,i}}\delta_{z+\hat{i},x}\delta_{z,y} + P_-\Theta(L_3 - z_3 - 1)e^{iA_{z,i}}\delta_{z,x}\delta_{z+\hat{i},y}, \tag{5.36}$$

where $P_\pm = \frac{\alpha_i \pm i\gamma_0}{2}$. Since we have constructed the Hamiltonian in such a way that it preserves translation invariance in x_1 and x_2 it can be partially diagonalised by using a plane wave basis in these directions:

$$\begin{aligned}h_{zz'}(k_1, k_2) = -i\alpha_3\nabla_{3,zz'} + \frac{\gamma_0}{2}\Delta_{zz'} + \delta_{zz'}\Big\{&\alpha_1 \sin(k_1) + \alpha_2 \sin(k_2 - Bx_3) \\ &+ 2\gamma_0 \sin^2(k_1/2) + 2\gamma_0 \sin^2((k_2 - bx_3)/2) + \gamma_0 m + \gamma_0 \mu_A\Big\}\end{aligned} \tag{5.37}$$

The partially diagonalised current in x_1 direction is then given by

$$j_{x_1,zz'}(k_1, k_2) = \delta_{zz'}\{\alpha_1 \cos(k_1) + \gamma_0 \sin(k_1)\}. \tag{5.38}$$

In the zero temperature limit the expectation value of the current (5.38) can be computed by summing over all the contributions from eigenstates of the single particle Hamiltonian (5.37) with negative energy values[2]:

$$\langle j_{x_1}(z)\rangle = \sum_i \int_{-\pi}^{\pi} \frac{dk_1}{2\pi}\frac{dk_2}{2\pi}\Theta(-\varepsilon_i(k_1, k_2))\bar{\psi}_{i,z}(k_1, k_2)j_{x_1,zz}(k_1, k_2)\psi_{i,z}(k_1, k_2), \tag{5.39}$$

where the energy levels $\varepsilon_i(k_1, k_2)$ and the eigenstates $\psi_{i,z}(k_1, k_2)$ are determined by the equation

$$\sum_{z'} h_{zz'}(k_1, k_2)\psi_{i,z'}(k_1, k_2) = \varepsilon_i(k_1, k_2)\psi_{i,z}(k_1, k_2). \tag{5.40}$$

To calculate the profile of the j_1 current in the slab Equation (5.39) is evaluated numerically. The `Cubature` [104] package is used for the numerical integration over the

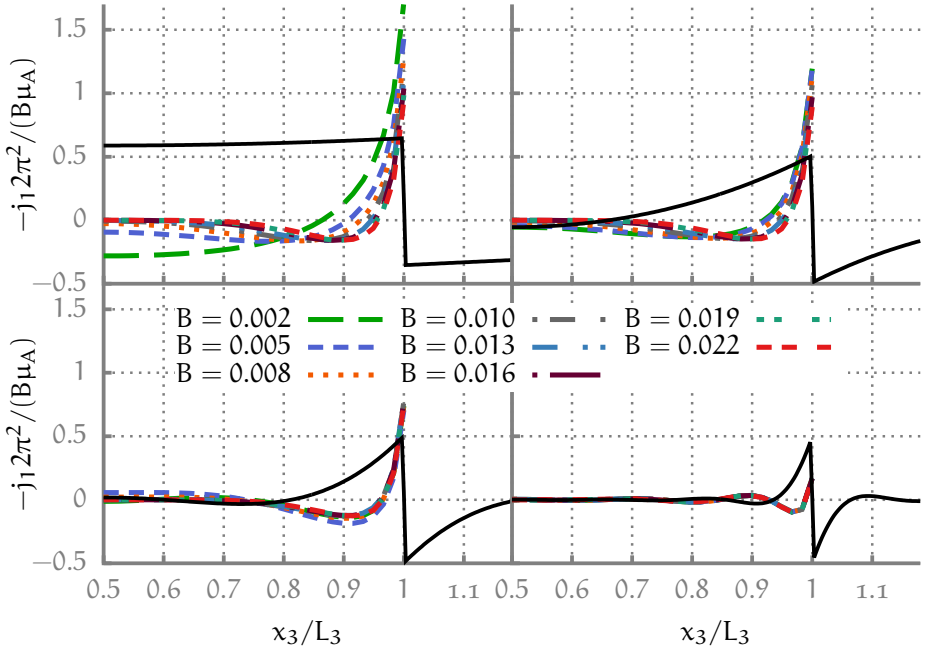

Figure 5.9: Spatial profiles of the current density j_1 at fixed μ_A for different values of B. From left to right and from top to bottom: $\mu_A = 0.01$, $\mu_A = 0.05$, $\mu_A = 0.1$ and $\mu_A = 0.3$. The solid black lines marks the result of a linear response calculation with σ_{CME} from Equation (4.2).

momenta k_1 and k_2. The spatial profiles of the current density j_1 for different values of the chiral chemical potential μ_A and a slab width $L_3 = 60$ are shown in Figure 5.9. The current density is symmetric with respect to the centre of the slab and therefore only half of the full profile is plotted. For all values of μ_A and B the current density is largest (in absolute value) close to the boundary of the slab and can show oscillations of comparatively small amplitude in the bulk. Directly at the boundary the magnitude of current density is close to the universal value and depending on the parameters it can be slightly smaller or bigger than (4.2). Summing up the total current over the cross-section of the slab numerically, we find that it vanishes within the precision of the numerical integration over the Brillouin zone.

The plot in Figure 5.10 depicts the dependence of the current profile on the slab with L_3 for small values of B and μ_A. Interestingly the current distribution near the boundary seems to be independent of the slab width. For large L_3 our numerical data shows that the current deep inside the bulk almost vanishes. This suggests that in the limit of very large slab widths all non-trivial behaviour of the current density is localised near the boundaries and does only depend on the magnetic field strength B and the chiral chemical potential μ_A and no longer on L_3. Moreover, for all the parameter values we have considered the absolute value of the current density assumes its maximum at the slab boundaries.

To study the dependence of the current density on the magnetic field strength and the chiral chemical potential we will therefore simply consider the current density at the slab boundaries. Figure 5.11 shows the current density on the boundary as a function of the magnetic field strength for different values of μ_A. As long as B and μ_A are small we

2 At zero temperature only the states in the Fermi sea are occupied. Compare also the derivation of the zero temperature limit of the free energy in Section 4.4

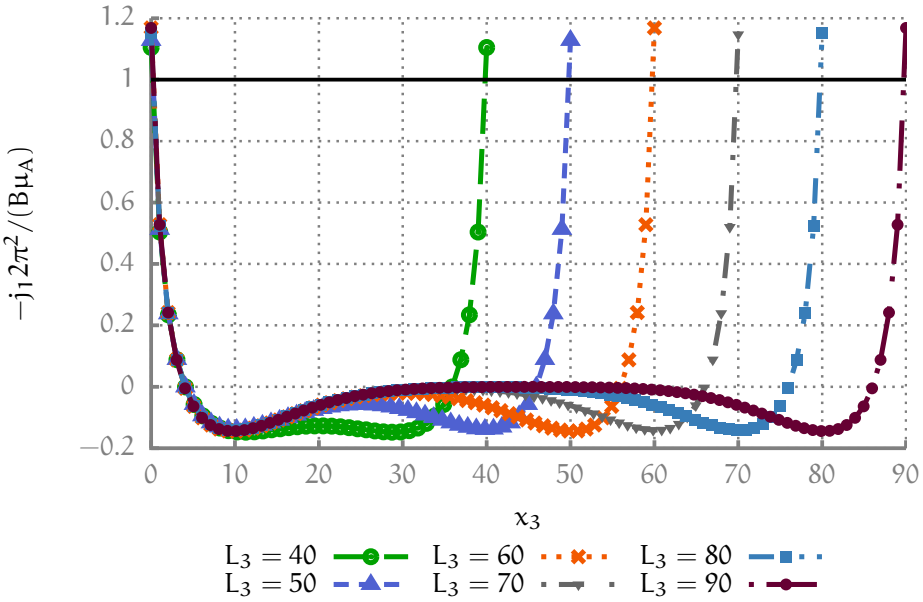

Figure 5.10: The current density in slabs with different width L_3 at fixed magnetic field $B = 0.007$ and chiral chemical potential $\mu_A = 0.05$. The solid black lines denotes the universal value (4.2).

observe a linear scaling of the current density with a slope that is close to the universal conductivity value (4.2). At larger values of B we see a saturation effect and in some cases the current density even decreases as B increases.

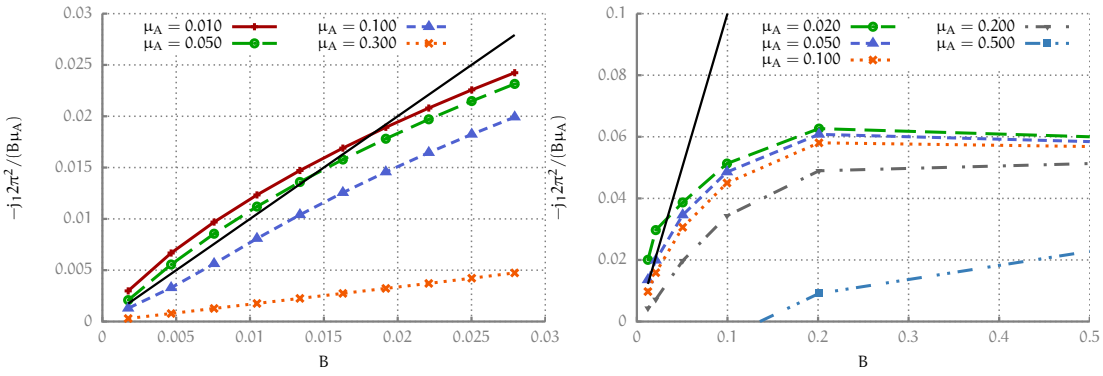

Figure 5.11: The current density at the boundaries of the slab as a function of the magnetic field strength B for different values of μ_A. The solid black line corresponds to (4.2). Left: For small magnetic fields the current dependence on B is approximately linear. Right: At large magnetic fields we observe a saturation of the current.

We now introduce the localisation width l_0 to further investigate the localisation of the current density near the slab boundaries. To this end we define l_0 as the distance from the slab boundary to the nearest extremum of the current density, i.e. l_0 is the (smallest) value for which

$$\frac{dj_1(x_3)}{d(x_3)}\bigg|_{x_3=l_0} = 0. \tag{5.41}$$

Numerical estimates for l_0 for different points in the parameter space are plotted in Figure 5.12. If the magnetic field strength $\sqrt{B} \gg \mu_A$ is very large compared to the chiral chemical potential the localisation with l_0 seems to depend only on B and is approximately equal to the magnetic length $l_B = 1/\sqrt{B}$ as long as $l_b < L_3/2$. On the other hand, if $\mu_A \gtrsim \sqrt{B}$, the dependence of l_0 on B is saturated and consequently l_0 depends only on μ_A.

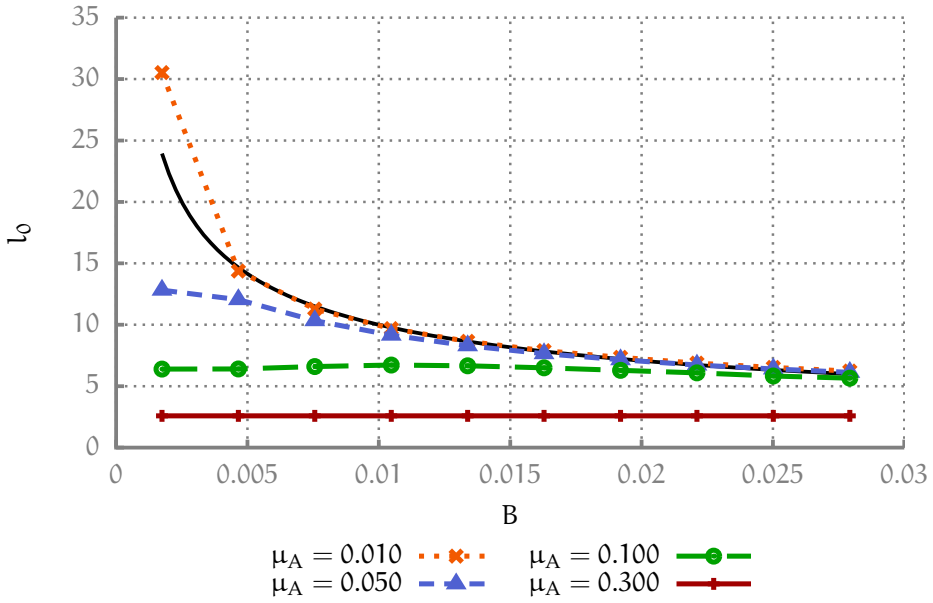

Figure 5.12: The localisation width l_0 as a function of the magnetic field strength B at different values of the chiral chemical potential μ_A. The solid black curve is the magnetic length $l_B = 1/\sqrt{B}$. For this plot the slab with is set ti $L_3 = 60$. As long as $l_B < L_3/2$ the localisation width l_0 is independent of L_3.

There is a conceptional difference between the linear response calculation of the last subsection and the model calculations with finite slab width. In one case we are dealing with a infinitely large WSM sample and a magnetic field that vanishes outside of a given region. In the other case we have a slab of finite width with open boundary conditions.

To estimate the effect of the open boundaries of the slab we repeat the linear response calculation of the last subsection with a magnetic field that vanishes everywhere except for a finite region of size L_3, where it is constant. The Fourier transform of this magnetic field configuration is then multiplied by $\sigma_{CME}(\vec{k})$ as given by Equation (5.29) and the current density is transformed back into coordinate space. The results of this calculation is depicted with solid black lines in Figure 5.9.

Like for the magnetic field of a solenoid we find that the qualitative behaviour of the linear response current density depends on the dimensionless product $L_3\mu_A$, where length scale is now given by the slab with L_3 instead of the solenoid radius R. In qualitative agreement with the results of subsection 5.3.1, the current density inside the slab is constant and its magnitude is close to the value (4.2) for $L_3\mu_A \lesssim 1$. In the regime where $L_3\mu_A \gg 1$ the current density is localised near the slab boundary. The localisation width is comparable to the l_0 found for the lattice calculation in the setup with $\mu_A \gg \sqrt{B}$ and does not depend on L_3. Figure 5.13 shows exemplary results for the linear response current density.

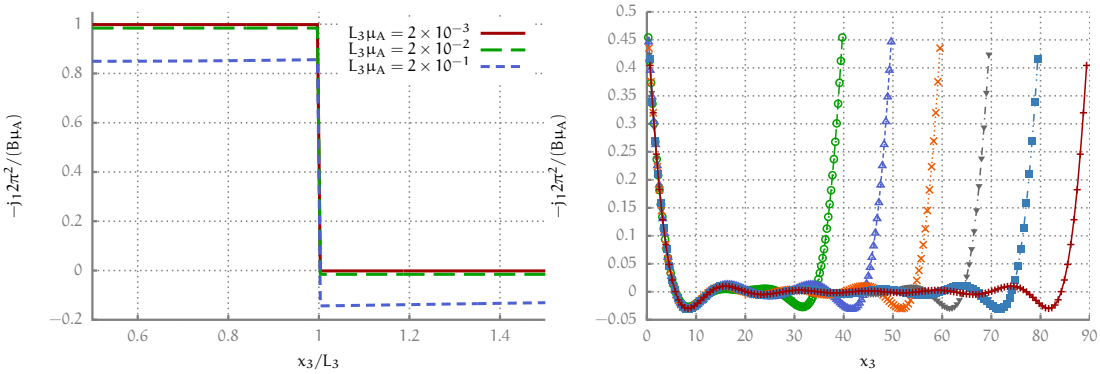

Figure 5.13: Profile of the linear response current density. Left: For $L_3\mu_A \lesssim 1$ the current density inside the slab is constant. Right: The current density is localised near the slab boundary if $L_3\mu_A \gg 1$. The localisation width l_0 does not depend on L_3. The current density outside of the slab is not shown.

In the linear response framework the total current summed over the whole space vanishes, but the current through a cross-section of the slab is not zero. The reason for this is that in the linear response calculations the sample is infinite and also extends into the region where the magnetic field vanishes.

We have identified two regimes with a qualitatively different behaviour of the chiral magnetic conductivity as a function of the magnetic field strength B in Figure 5.11. If $B \ll \mu_A^2$ the absolute value of the current density at the slab boundary is close to the universal value (4.2) and the current depends linearly on the magnetic field. In the regime where $\mu_A \ll \sqrt{B}$ calculations within our non-interacting WSM model show that higher order effects in B become important and the current is no longer a linear function of B.

This raises the question which of the two scenarios is realised in realistic experimental setups. Above we have argued that the chiral chemical potential inside a WSM is of order $\mu_A \sim 10$ meV. Typical magnetic field strengths in experiments are on the order of $B \sim 1$T. In natural units one Tesla is approximately $1\text{T} \approx (26\text{eV})^2$, which suggests that experiments are performed deep in the non-linear regime. This is a reminder that the results of the linear response analysis should be taken with a grain of salt.

Additionally, we emphasise that all the calculations in this section are performed in a highly idealised setup. Possible complications that can occur in realistic experiments have simply been neglected. We have made the assumption that the system is in a state of dynamical equilibrium due to chirality pumping and that this state can be approximated by a ground state of a many-body Hamiltonian with finite chiral chemical potential. Any dynamical processes have been disregarded. We have also ignored the fact that the magnetic field inside a crystal can depend on many different parameters and can in general be a complicated function of the applied external field. Moreover, possible contributions from boundary states have not been taken into account and we did not consider the effect of grain boundaries inside the sample.

Even so, the naive model calculations show that it is in principle possible to observe the chiral magnetic effect also in the case of static and homogeneous magnetic fields and our results can be used to make educated order-of-magnitude estimates that can offer some guidance in the design of new experiments.

6

DISCUSSION AND CONCLUSION

In the last two chapters we studied the CME in an interacting, $\mathcal{P}$-breaking WSM. To this end we considered a lattice model with on-site inter-electron interactions. In our model we used the Wilson–Dirac operator and therefore the chiral symmetry is explicitly broken and is only an emergent symmetry at low energies. By taking the inter-electron interaction *and* the explicit breaking of chiral symmetry into account, we have gone beyond some of the limitations of previous model calculations.

Using a mean-field approximation we investigated the phase diagram of our model in the parameter space of bare mass, interaction strength and bare chiral chemical potential. For every set of parameters that we considered in our scan over the parameter space we additionally computed the static chiral magnetic conductivity with a linear response ansatz.

In our mean-field calculations we made the assumption that the mean-field Hubbard–Stratonovich field is isotropic and homogeneous. In this case the mean-field value of the Hubbard–Stratonovich field can be parametrised by Equation (4.25), which significantly simplifies the mean-field calculations and in particular the numerical minimisation of the mean-field free energy. In view of the results of [78–82], which suggest that the chiral chemical potential is unstable and can decay by creating helical magnetic field configurations, this assumption seems to be highly questionable. The Hubbard–Stratonovich field can mimic external gauge fields, since the condensates can take the form $\Phi \sim \alpha_i A_i$. If a configuration with finite chiral chemical potential is indeed unstable, one can therefore expect that a spatially inhomogeneous Hubbard–Stratonovich field has a lower energy than a homogeneous field configuration and constitutes the true ground state of our model. Studies of the holographic Sakai–Sugimoto model [105–107] lend some credence to the possibility of a non-homogeneous ground in a system with finite chiral chemical potential, at least for sufficiently large values of μ_A of the order of the vector meson masses in the model.

To compute the static conductivity $\sigma_{\mathrm{CME}}(k)$ with the Kubo formula (5.3) we have to evaluate the second variation of the free energy. As part of this evaluation the Hessian matrix $\frac{\partial^2 \mathcal{F}[\Phi_x, A_{x,k}]}{\partial \Phi_{x,A} \partial \Phi_{y,B}}$ containing the second derivatives of the mean-field free energy with respect to the Hubbard–Stratonovich field components $\Phi_{x,A}$ has to be computed and evaluated at $\Phi_x = \Phi^\star$. If the homogeneous field configuration $\Phi^\star$ is a local minimum in the space of all possible Hubbard–Stratonovich fields all the eigenvalues of this matrix should be positive. Owing to the spatial homogeneity of $\Phi^\star$, the entries of the Hessian matrix can only depend on the relative coordinate $x - y$ and we can calculate its eigenvalues by performing a Fourier transformation with respect to $x - y$. For each wave vector in the Brillouin zone one then has to diagonalise only a matrix of size 15×15,

corresponding to the 15 different spinor structures that we chose as a basis for Φ_x in Equation (4.24). We calculated the eigenvalues of the Hessian for every point in our scan over the parameter space and for the wave vectors $k_3 = 2\pi m/L_s$ with $m \in \{0, \cdots, 8\}$ and found that they are always positive. An exemplary plot of the eigenvalues of the Hessian as a function of the interaction strength U for the parameter values $m^0 = -2.6$, $\mu_A^0 = 0$ and $k_3 = 0$ is shown in Figure 6.1. An interesting feature of this plot is the behaviour of the eigenvalue corresponding to the pion mass. At the phase boundaries of the Aoki phase the pion mass vanishes, and we can clearly see the two dips of the eigenvalue close to the phase transitions (compare with the phase diagram in Figure 4.2). From

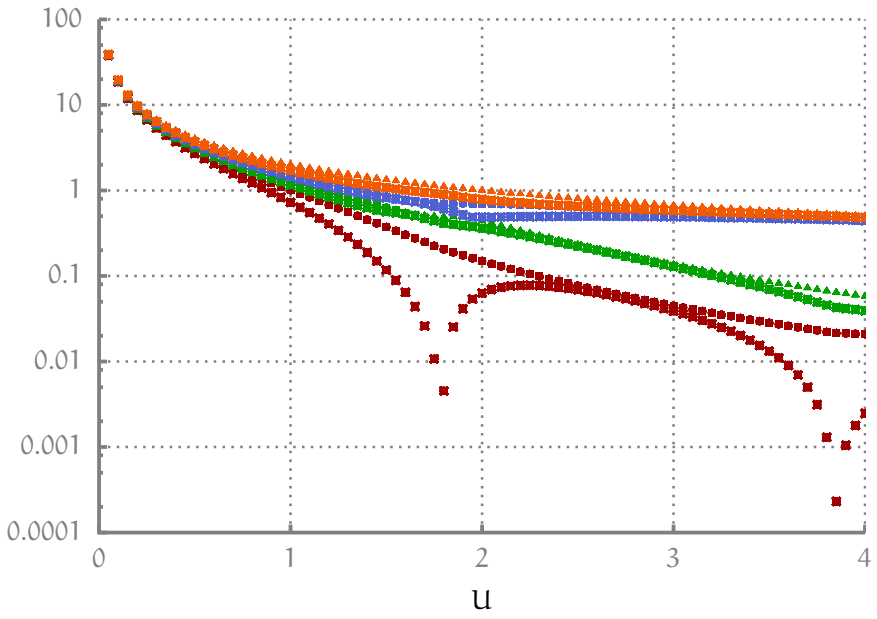

Figure 6.1: Eigenvalues of the Hessian matrix as a function of U for $m^0 = -2.6$, $\mu_A^0 = 0$ and $k_3 = 0$. The spectrum of the Hessian is highly degenerate, reflecting the symmetries of the free energy. All eigenvalues are positive, except at the second order phase transition where the pion mass vanishes.

the positivity of all the eigenvalues of the Hessian matrix it follows that the homogeneous and isotropic Hubbard–Stratonovich field $\Phi^\star$ is a local minimum in the space of all possible Hubbard–Stratonovich fields Φ_x. If a non-homogeneous field configuration which further decreases the mean-field free energy exists it is separated from $\Phi^\star$ by a potential barrier in the field space. In hindsight, this result to some extend justifies the assumptions we made for the mean-field value of $\Phi^\star$. The decay of the chirality imbalance was also investigated in the framework of classical statistical field theory in [83]. In this study no sign for the formation of a non-trivial spatially inhomogeneous gauge field configuration was found. Combining the evidence from all these numerical studies it seems reasonable to assume that the ground state in an interacting, $\mathcal{P}$-breaking WSM is homogeneous and isotropic, at least for small values of the chiral chemical potential.

The mean-field phase diagram of the model exhibits two different phases: A $\mathcal{CP}$-symmetric phase and the Aoki phase (or axionic insulator phase) where the $\mathcal{CP}$-symmetry is spontaneously broken. Our numerical results suggest that the phase transition to the Aoki phase is of second order. The Aoki phase is still present at finite temperature and finite chiral chemical potential. Naively, one would expect that a finite

temperature acts against the formation of the fermionic condensates $\langle \hat{\psi}^{\dagger}_{x,\alpha} \hat{\psi}_{x,\beta} \rangle \neq 0$. Indeed we find that for $T > 0$ the critical interaction strength for the onset of the Aoki phase is shifted to slightly larger values, see Figure 4.6. Increasing the bare chiral chemical potential, on the other hand, leads to a decrease of the critical interaction strength, as is evident from Figure 4.2.

In both phases we observe a strong multiplicative renormalisation of the chiral chemical potential. The slope of the renormalised chiral chemical potential as a function of the interaction strength changes at the phase boundary and its growth is even more pronounced in the Aoki phase. This is consistent with the results of a previous study of a model with continuum Dirac fermions with on-site inter-fermion interactions [14].

In our model the static chiral magnetic conductivity is strongly enhanced compared to a system with non-interacting fermions. This enhancement is however almost entirely a result of the strong renormalisation of the chiral chemical potential. The numerical estimates for σ_{max} are plotted in Figure 5.4 and the absolute value of σ_{max} is never larger than the canonical value $\frac{N_f \mu_A}{2\pi^2}$, provided that we use the renormalised value μ_A of the chiral chemical potential in Equation (4.2) and take into account the number N_f of Dirac cones in the spectrum. From a field-theoretical point of view one could therefore argue that the inter-electron interactions do not lead to a enhancement of the chiral magnetic conductivity, since only the renormalised μ_A is physically observable. In the context of experiments with WSMs, on the other hand, the situation might be different. The "bare" value of the chiral chemical potential could in principle be measurable, for example if it is generated dynamically by chirality pumping via Equation (4.3). In the tight-binding model in [108] the chiral chemical potential is related to the mechanical strain. As we have mentioned above, the renormalised chiral chemical potential in a WSM sample can be measured in ARPES experiments [101]. It is an interesting open question how and if the multiplicative renormalisation of μ_A is realised in the case of a dynamically generated chiral chemical potential and how this affects the chiral magnetic conductivity.

Interestingly in our model the chiral magnetic conductivity is strongly suppressed as soon as the $\mathcal{CP}$-symmetry is spontaneously broken. This is in stark contrast to the findings of the study with continuum Dirac fermions in [14], where – on the contrary – σ_{CME} takes its largest values inside the phase with spontaneously broken chiral symmetry. We conclude that the exact chiral symmetry in the continuum is important for the strong enhancement of σ_{CME} in [14].

In principle, one could also perform calculations with lattice fermions with an exact chiral symmetry. One possibility are staggered fermions [109], but in this case there are $N_f = 4$ species of fermions and only a $U(1)$ symmetry. A direct comparison with the results for continuum fermions is hence not possible. Using the Hamiltonian for overlap fermions [110] $N_f = 1$ and an exact $U(1)$ chiral symmetry can be achieved. The overlap Hamiltonian as well as the chiral symmetry transformations for overlap fermions are however non-local and therefore the overlap chiral symmetry is not compatible with local on-site interactions. Apart from conceptional difficulties and the fact that a non-local Hamiltonian looks rather unrealistic and artificial in the context of solid state physics, it is important to keep in mind that chiral symmetry is explicitly broken at high energies in a WSM. Any model aiming for a realistic description of a WSM should therefore take the explicit symmetry breaking into account.

Considering the two contributions to the variation of the free energy in Equation (5.10) individually allows us to disentangle the effects of the renormalisation of the parameters

of the Hamiltonian from non-trivial corrections to the σ_{CME} caused by the inter-electron interactions. The ratio of the absolute value of the two contributions is an intricate function of the model parameters and depends also on the wave vector k, see Figure 5.6. Nevertheless, it is possible to make some general statements. First of all it is remarkable that in the region where the gap in the energy spectrum is small the conductivity is basically saturated by the tree-level contributions. Especially close to the lines with constant renormalised mass $m_r = -6, -4, -2, 0$ the only relevant effect of the interactions is the renormalisation of the chiral chemical potential and the relative magnitude of the loop corrections is significantly below the percent level.

In the Aoki phase, where the gap size is large, the loop corrections to σ_{CME} become more important and can have the same magnitude as the tree-level contributions. The chiral magnetic conductivity is, however, strongly suppressed in this phase. The loop contributions become relevant because the tree-level contributions are orders of magnitude smaller inside the Aoki phase than outside, whereas the magnitude of the loop contributions does not change much.

In our lattice model the $\mathcal{CP}$-symmetry is a remnant of the continuum chiral symmetry. Theoretical arguments suggest that σ_{CME} is no longer related to the anomaly coefficient if the chiral symmetry is spontaneously broken [14, 111] and our results support this expectation.

For completeness we also investigated the temperature dependence of σ_{CME}. While a finite temperature does not have a huge effect for the phase diagram of or model (Figure 4.6), we found that σ_{CME} strongly decreases with temperature. The underlying physical reason is that a temperature comparable to or larger than the chiral chemical potential tends to smooth out the differences in the occupation numbers of left- and right-handed fermions. Exemplary results at finite temperature are plotted in Figure 5.7.

The main aim of our calculations within a lattice model of an interacting, $\mathcal{P}$-breaking WSM has been to attempt a first, qualitative description of experiments with Dirac semimetals [5, 6, 60, 61], where a chirality imbalance is dynamically generated by chirality pumping in parallel electric and magnetic fields. The chirality imbalance breaks parity, turning the Dirac semimetal into a WSM. The signature of the CME in these experiments is a negative magnetoresistivity in the direction of the applied magnetic field.

To keep the model as simple as possible we worked in a strongly idealised setup and introduced several approximations. The most important one is the parametrisation of the chiral imbalance by a chiral chemical potential. In an experiment chirality pumping is a dynamical process and for a more realistic description this should be taken into account. A possible improvement would be to adapt the mean-field approximation to use the real-time linear-response theory. Moreover, in most of our calculations we used a lattice with periodic boundary conditions and completely neglected possible boundary effects. The results of [103] and of Section 5.3 clearly show that such effects can be important.

Nevertheless, we can draw some general conclusions from our calculations. In particular, it is interesting to see the difference between our model with an explicitly broken chiral symmetry compared to the chirally symmetric continuum model [14]. While both models give similar qualitative results as long as the (remaining) symmetry is intact, there are huge differences in the phase with spontaneously broken symmetry. The continuum model predicts an interaction induced enhancement of the static chiral magnetic conductivity throughout the phase diagram and in particular in the phase with spontan-

eously broken chiral symmetry. In the lattice model the enhancement of σ_{CME} due to the interactions seems to come solely from the strong renormalisation of the chiral chemical potential. In the Aoki phase σ_{CME} is strongly suppressed, even though the renormalisation of μ_{A} is strongest in this phase. The clear message here is that it is important to take the explicit breaking of chiral symmetry away from the Weyl points in the spectrum into account to model a WSM.

Part III

THE CHIRAL SEPARATION EFFECT IN QCD

The following part deals with the Chiral Separation Effect in QCD at finite temperature and density. To study the Chiral Separation Effect in the framework of lattice QCD it was necessary to develop and implement a new numerical method for the calculation of conserved lattice currents for chiral overlap fermions. The numerical method was developed and tested in [112, 113], but first results were already presented in [114]. Some of the more technical parts of Sections 7.2 – 7.4 and the descriptions of the plots in the Figures 7.3 – 7.7 are taken (almost) verbatim from [112]. The first application of this new method to a physical problem was the study of the Chiral Separation Effect in quenched QCD [115].

7

ANOMALOUS TRANSPORT ON THE LATTICE

7.1 MOTIVATION

In heavy-ion collision experiments it is possible to create temperatures and densities similar to the conditions in the early universe shortly after the big bang. They are an essential experimental tool to address important open questions in high-energy physics, astrophysics and cosmology. The plasma generated in such collisions is dominated by quarks and gluons and rapidly cools to form particles. Conclusions about the underlying elementary interactions can be drawn from the type and distribution of the particles generated in a collision.

At high temperatures the chiral condensate of QCD "melts" and the chiral symmetry of the theory is restored. QCD is asymptotically free and it is therefore generally believed that at high temperatures and densities a chirally symmetric phase with deconfined quarks and gluons, the so-called quark-gluon plasma, emerges. Moreover, in off-centre heavy-ion collisions large magnetic fields can be generated [2, 116]. For all these reasons, it is sensible to assume that anomalous transport effects can play a role in heavy-ion collision experiments. For a discussion of possible experimental signatures of anomalous transport effects in heavy-ion collisions see for example [43, 117].

It is therefore of great interest to study anomalous transport phenomena in QCD and in particular possible corrections to the anomalous transport coefficients due to the strong interactions. In principle, lattice simulations provide a framework for non-perturbative, ab-initio calculations in QCD. However, as we have already discussed in Chapter 2, the introduction of a finite quark chemical potential as well as the implementation of chiral symmetry on the lattice pose technical difficulties.

For Wilson–Dirac fermions it is possible to introduce a chiral chemical potential without causing a sign problem. The anomalous transport coefficient for the CME was measured in [118, 119] with quenched and dynamical Wilson-Dirac fermions for a range of different temperatures. In these simulations it was found that the numerical value of the transport coefficient differs significantly from theoretical predictions. The reason for this deviation and the systematic error of the calculations due to a renormalisation of the vector current for Wilson–Dirac fermions were not further investigated. For chiral lattice fermions it can be shown that the axial as well as the vector current are not renormalised and in [13] it was suggested to use overlap fermions to study anomalous transport phenomena on the lattice.

Constructing a chiral chemical potential for overlap fermions is quite involved [120] and for a first anomalous transport study with strongly interacting overlap fermions we consider the CSE on the lattice, which only requires a (vector) chemical potential. In heavy-ion collisions the CSE can potentially generate a chirality imbalance, acting as

a trigger for the CME. In combination these effects can give rise to a Chiral Magnetic Wave [121–123].

The overlap Dirac operator at finite quark chemical potential is given by Equation (2.56) and for the kernel we use the Wilson–Dirac operator (D.1). To avoid the sign problem we work in the quenched approximation.

The form of the conserved currents depends on the action and can be derived using Noether's theorem. Conserved currents for Ginsparg–Wilson fermions that also have the correct transformation properties under the lattice chiral symmetry (2.48) were constructed in [124, 125]. The overlap version of the continuum current densities $j_\mu = \bar{\psi}\gamma_\mu\bar{\psi}$ and $j^A_\mu = \bar{\psi}\gamma_5\gamma_\mu\bar{\psi}$ is given by

$$j_{x,\mu} = \frac{1}{2}\bar{\psi}\big(K_{x,\mu} - \gamma_5 K_{x,\mu}\gamma_5(1 - D_{ov})\big)\psi, \tag{7.1}$$

$$j^A_{x,\mu} = \frac{1}{2}\bar{\psi}\big(-\gamma_5 K_{x,\mu} + K_{x,\mu}\gamma_5(1 - D_{ov})\big)\psi, \tag{7.2}$$

where $K_{x,\mu} = \frac{\partial D_{ov}}{\partial \Theta_{x,\mu}}$ is the derivative of the overlap operator D_{ov} over the $U(1)$ lattice gauge field $\Theta_{x,\mu}$. Computing the overlap operator and its derivative at finite chemical potential is numerically very demanding. The following sections are dedicated to a discussion of the numerical aspects of overlap fermions and the implementation of an efficient numerical algorithm to evaluate derivatives of matrix functions. Physical results will be presented in the next chapter.

7.2 MATRIX FUNCTIONS

The matrix sign function, as used to define the overlap Dirac operator, maps a matrix to a matrix. Functions of this type have become an essential tool in many different sub-fields of science and engineering [126, Chapter 2]. While we are mainly interested in the matrix sign function, we emphasise that the theoretical and numerical methods introduced in this chapter are very general and can in principle be applied to arbitrary matrix functions.

Let $f : \mathbb{C} \to \mathbb{C}$ be a function that is well defined on the spectrum of some general complex matrix $A \in \mathbb{C}^{n\times n}$. There exist several equivalent ways to generalise the definition of f to a matrix function $f : \mathbb{C}^{n\times n} \to \mathbb{C}^{n\times n}$, for an in-depth discussion see for example [126, 127]. The definition best suited to our purpose is the one employing the Jordan canonical form. A well known linear algebra theorem [128] states that any matrix $A \in \mathbb{C}^{n\times n}$ can be written in the Jordan canonical form

$$X^{-1}AX = J = \mathrm{diag}(J_1, J_2, \cdots, J_k) \tag{7.3}$$

where every Jordan block J_i corresponds to an eigenvalue λ_i of the matrix A and is given by

$$J_i = J_i(\lambda_i) = \begin{pmatrix} \lambda_i & 1 & 0 & \cdots & 0 \\ 0 & \lambda_i & 1 & \ddots & \vdots \\ 0 & \ddots & \ddots & \ddots & 0 \\ \vdots & \ddots & \ddots & \lambda_i & 1 \\ 0 & \cdots & 0 & 0 & \lambda_i \end{pmatrix} \in \mathbb{C}^{m_i\times m_i}, \tag{7.4}$$

with $m_1 + m_2 + \cdots + m_k = n$. The Jordan matrix J is unique up to permutations of the Jordan blocks, but the transformation matrix X is not. With the help of the Jordan canonical form the function of a matrix can be defined as [126, 127]

$$f(A) := Xf(J)X^{-1} = X\,\mathrm{diag}(f(J_i))X^{-1}. \tag{7.5}$$

The function of the Jordan block J_l is given by the upper triangular matrix

$$f(J_l) := \begin{pmatrix} f(\lambda_l) & f'(\lambda_l) & \dots & \frac{f^{(m_l-1)}(\lambda_l)}{(m_l-1)!} \\ 0 & f(\lambda_l) & \ddots & \vdots \\ \vdots & \ddots & \ddots & f'(\lambda_l) \\ 0 & \cdots & 0 & f(\lambda_l) \end{pmatrix} \in \mathbb{C}^{m_l \times m_l}, \tag{7.6}$$

where $f^{(m_l-1)}$ stands for the (m_l-1)-th derivative of the function f. Notice that the existence of the derivatives $f^{(m_l-1)}(\lambda_l)$ for $l = 1, \cdots, k$ is required to define the matrix function $f(A)$. If A is diagonalisable every Jordan block has size one and Equation (7.6) simplifies to the so-called spectral form

$$f(A) = X\,\mathrm{diag}(f(\lambda_1), f(\lambda_2), \dots, f(\lambda_n))X^{-1}, \tag{7.7}$$

which does not depend on the derivatives of f.

To evaluate the overlap Dirac operator at finite chemical potential one has to compute the matrix sign function of a non-Hermitian matrix. A non-Hermitian matrix has complex eigenvalues and in the light of equations (7.5) and (7.7) this means that we need a generalisation of the sign function to complex arguments. It is important to ensure that the generalised sign function still squares to unity, i.e. $\mathrm{sgn}(z)^2 = 1$, for any complex number z. This feature of the sign function ensures that the overlap operator obeys the Ginsparg–Wilson equation. Additionally, the complex sign function should reduce to the standard definition $\mathrm{sgn}(x) = \pm 1$ for $x \in \mathbb{R}^{\pm}$. A possible definition which fulfils all the requirements is

$$\mathrm{sgn}(z) := \frac{z}{\sqrt{z^2}} = \mathrm{sgn}(\mathrm{Re}(z)), \tag{7.8}$$

where the cut of the square root is chosen along $z \in \mathbb{R}^-$, such that the cut of the sign function is along the imaginary axis where $\mathrm{Re}(z) = 0$.

Another possibility to define the matrix sign function is to use the so-called Roberts iteration. This iterative method is based on applying Newton's method to the matrix equation $S^2 - 1 = 0$ and is defined by

$$S_{k+1} := \frac{1}{2}\left(S_k + S_k^{-1}\right) \quad \text{with} \quad S_0 := A, \tag{7.9}$$

where the iteration is stopped once the desired accuracy has been reached. It can be shown that the Roberts iteration converges quadratically to $\mathrm{sgn}(A)$, provided that A has no purely imaginary eigenvalue [126].

The Jordan (or spectral) decomposition [129] as well as the Roberts iteration[1] are computationally expensive task and require $\mathcal{O}(n^3)$ floating point operations. In lattice

1 The complexity of the Roberts iteration is given by the complexity of matrix multiplication. Algorithms for matrix multiplication with a complexity $\mathcal{O}(n^\omega)$ with $\omega < 3$ are known. At the time of writing the optimum is $\omega = 2.3728639$ [130]. In practical implementations of matrix multiplication algorithms, however, a value of $\omega \approx 3$ is typical.

calculations the dimension of the matrix is given by $12V$, where V is the lattice volume and the factor 12 appears because the fermionic field at every lattice site has 4 Dirac and 3 colour components. The numerical cost for an evaluation of the overlap operator increases drastically with the lattice size and even for relatively small lattice volumes it is not feasible to compute the matrix sign function exactly.

Additionally, the memory required to store the result of a matrix function can also become an issue. The kernel H of the overlap operator is a sparse matrix and the memory needed to store it grows as the lattice size V. The result of the function of a sparse matrix is not necessarily a sparse matrix itself and the memory needed to store it is proportional to V^2.

7.2.1 *Numerical Approximation of Matrix Functions*

The numerical cost and the memory requirements for the evaluation of functions of large matrices seem daunting at first. Fortunately for a large class of applications it is sufficient to compute the result $|y\rangle = f(A)\,|x\rangle$ of the matrix $f(A)$ acting on a vector $|x\rangle$ and the knowledge of the explicit form of $f(A)$ is not necessary.

A variety of algorithms to efficiently compute an approximation of $|y\rangle = f(A)\,|x\rangle$ were developed, see for example [126, Chapter 13] and [127, Chapter 9].

For Hermitian matrices A the sign function can be efficiently approximated by a polynomial or a rational function (see for example [131–134]), for non-Hermitian matrices these algorithms generally become inefficient. A method that works well for non-Hermitian matrices is the so-called Two-Sided Lanczos (TSL) algorithm. The TSL algorithm belongs to the class of Krylov subspace algorithms. The Krylov subspace of order k for a matrix A and a vector $|x\rangle$ is defined as

$$\mathcal{K}_k(A, |x\rangle) := \text{span}(|x\rangle, A\,|x\rangle, \cdots, A^{k-1}\,|x\rangle). \tag{7.10}$$

The idea of the TSL algorithm is to construct biorthogonal bases $V_k = (|v_1\rangle, \cdots, |v_k\rangle)$ and $W_k = (|w_1\rangle, \cdots, |w_k\rangle)$ of the right $(\mathcal{K}_k(A, |x\rangle))$ and left $(\mathcal{K}_k(A^\dagger, |x\rangle))$ Krylov subspace of A such that the k-dimensional matrix

$$T_k := W_k^\dagger A V_k \tag{7.11}$$

is tridiagonal, i.e.

$$T_k = \begin{pmatrix} \alpha_1 & \gamma_1 & 0 & \dots & 0 \\ \beta_1 & \alpha_2 & \ddots & \ddots & \vdots \\ 0 & \ddots & \ddots & \ddots & 0 \\ \vdots & \ddots & \ddots & \ddots & \gamma_{k-1} \\ 0 & \dots & 0 & \beta_{k-1} & \alpha_k \end{pmatrix}. \tag{7.12}$$

By plugging Equation (7.12) into (7.11) it is straightforward to derive recursion relations for the entries of T_k [127]:

$$\beta_i\,|v_{i+1}\rangle = (A - \alpha_i)\,|v_i\rangle - \gamma_{i-1}\,|v_{i-1}\rangle \qquad \gamma_0\,|v_0\rangle := 0 \tag{7.13}$$

$$\gamma_i^*\,|w_{i+1}\rangle = (A^\dagger - \alpha_i^*)\,|w_i\rangle - \beta_{i-1}^*\,|w_{i-1}\rangle \qquad \beta_0^*\,|w_0\rangle := 0 \tag{7.14}$$

The main diagonal of the matrix T_k is fixed, since the recurrence relations in combination with the biorthogonality condition $W_k^\dagger V_k = \mathbb{1}$ imply that $\alpha_i := \langle w_i | A | v_i \rangle$. The off-diagonal entries β_i and γ_i are not uniquely determined, but have to be chosen self-consistently such that $\langle w_{i+1} | v_{i+1} \rangle = 1$. As we will see later on, it is advantageous to use $|v_1\rangle = |w_1\rangle = |x\rangle / \|x\|$, with the norm $\|x\| = \sqrt{\langle x | x \rangle}$, as seed for the recurrence relations.

The product matrix $V_k W_k^\dagger$ is an oblique projector to the Krylov subspace $\mathcal{K}_k(A, |x\rangle)$. Having constructed V_k and W_k we can approximate $|y\rangle$ by the oblique projection of $f(A)|x\rangle$ on $\mathcal{K}_k(A, |x\rangle)$:

$$|y\rangle \approx |y\rangle_{\text{obl}} := V_k W_k^\dagger f(A) V_k W_k^\dagger |x\rangle \tag{7.15}$$

This expression still contains the function of the original matrix $f(A)$. The trick now is to additionally make the approximation $W_k^\dagger f(A) V_k \approx f(T_k)$. The seed vector for the recurrence relations is parallel to $|x\rangle$ and by construction $\langle w_i | x \rangle = \|x\| \, |e_1\rangle \, \delta_{1i}$, where $|e_1\rangle$ is the unit vector in the direction of the first coordinate axis. Applying the last approximation therefore yields

$$|y\rangle \approx \|x\| V_k f(T_k) |e_1\rangle \,. \tag{7.16}$$

The task of calculating $|y\rangle$ is now reduced to the construction of the bases V_k and $W_k^\dagger$ and the evaluation of the matrix function of the tridiagonal matrix $f(T_k)$. An implementation of the TSL in pseudo-code can be found in Listing F.1.

By using the approximation (7.16) the complexity of evaluating the action of the matrix function on a vector is decreased from $\mathcal{O}(n^3)$ to $\mathcal{O}(nk) + \mathcal{O}(k^3)$. In many cases it is possible to obtain a very good approximation of $|y\rangle$ already for $k \ll n$. Broadly speaking the TSL algorithm approximates a function by a matrix polynomial of order k, where the coefficients of the interpolating polynomial depend on the matrix A and the source vector $|x\rangle$. Compared to the (global) polynomial or rational function approximations, by tuning the approximation to a specific source vector the TSL typically achieves a given precision already with a lower order polynomial (see for example Figure 7.3).

The finite density overlap Dirac operator in particular can be approximated very efficiently with the TSL algorithm and the performance of the method can be further increased by using deflation methods [135, 136] (see also [137]) and a nested version of the algorithm [138].

For larger lattice sizes even the storage of the comparatively small matrices V_k and $W_k^\dagger$ can become a problem. In such cases it is necessary to use a double-pass version of the TSL algorithm. In the double pass algorithm only basis vectors necessary for the next iteration are stored. The first pass is used to construct the tridiagonal matrix T_k and in the second pass the matrix product $V_k f(T_k)$ is computed, trading speed for memory.

7.3 NUMERICAL MATRIX FUNCTION DERIVATIVES

In this section we address the question of how to compute derivatives of matrix functions numerically. From now on we assume that the matrix $A \equiv A(t)$ depends on the parameter t. In lattice calculations this parameter will typically be related to the link variables. The derivatives of $|y\rangle$ with respect to t are given by

$$\partial_t |y\rangle = \left(\partial_t f\left(A(t)\right)\right) |x\rangle \,, \tag{7.17}$$

where $\partial_t := \frac{\partial}{\partial t}$. For the rational and polynomial approximations explicit expressions for the derivative are known, but computing the derivative for an implicit, source vector dependent algorithm like the TSL is more involved. The TSL could be combined with a finite difference method, but finite differences are very sensitive to round-off errors and in practical calculations with a limited machine precision it is often not possible to compute the finite difference derivatives with a high enough precision. Algorithmic differentiation (AD) is a more advanced numerical differentiation technique and can in principle evaluate numerical derivatives with machine precision [139]. Listing F.2 sketches the algorithmic differentiation of the TSL. It turns out that a naive implementation of AD for the TSL method leads to a numerically unstable algorithm. Results of test runs for different matrix dimensions are shown in Figure 7.1. Even for relatively small matrices the error of the derivative is very large. The reason for this is probably the inherent numerical instability of the TSL. Because of round-off errors the bases W_k and V_k are not really biorthogonal in any practical calculation. In the TSL algorithm itself this is not a big issue, since in the final step the product $W_k^\dagger |x\rangle$ can simply be replaced by the analytical result $\|x\| |e_1\rangle$. Using the known analytic expression to some amount corrects for the accumulated numerical errors. In the AD calculation, however, the loss of biorthogonality seems to be a severe problem.

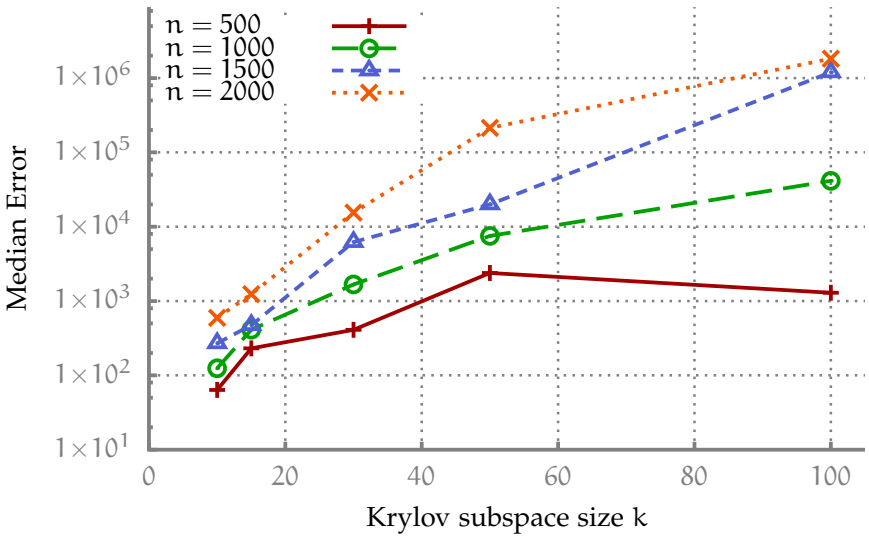

Figure 7.1: Error of the numerical derivative of the TSL computed with the algorithmic differentiation algorithm. The symbols mark the mean error for different matrix dimensions. For every matrix dimensions 200 different test matrices were used. The exponential growth of the error with the Krylov subspace size shows that the algorithm is numerically unstable.

To develop a stable numerical derivative algorithm for matrix functions, which also works for implicitly defined matrix function approximations, we therefore use a different ansatz. The proposed algorithm is based on the following theorem [140]:

Theorem 1. *Let $A(t) \in \mathbb{C}^{n\times n}$ be differentiable at $t = 0$ and assume that the spectrum of $A(t)$ is contained in an open subset $\mathcal{D} \subset \mathbb{C}$ for all t in some neighbourhood of 0. Let f be $2n-1$ times continuously differentiable on $\mathcal{D}$. Then*

$$f(\mathcal{B}) \equiv \begin{pmatrix} f(A(0)) & \partial_t f(A(t))|_{t=0} \\ 0 & f(A(0)) \end{pmatrix}, \quad \mathcal{B}(A, \partial_t A) := \begin{pmatrix} A(0) & \partial_t A(t)|_{t=0} \\ 0 & A(0) \end{pmatrix}$$

Theorem 1 relates the derivative $\partial_t f(A)$ of a matrix function to the function $f(\mathcal{B})$ of the block matrix $\mathcal{B}(A, \partial_t A)$. It is not necessary to know the explicit expression for $\partial_t f(A)$ to compute the derivative of $f(A)$, the knowledge of $\partial_t A$ is sufficient. This comes at a price, though. The function f has to be evaluated for a block matrix with twice the size of the original matrix A. In practical calculations the derivative $\partial_t A$ is usually known analytically or can be approximated with high precision. The block matrix $\mathcal{B}$ is very sparse and only the matrices A and $\partial_t A$ need to be stored.

At first sight Theorem 1 might look counterintuitive. To gain a better understanding it is helpful to consider the theorem for the special case where f is a matrix power function. We define $p_n(\mathcal{B}) := \mathcal{B}^n$ and consider $n = 2$ first, where the theorem obviously gives the correct answer for the derivative:

$$p_2(\mathcal{B}) = \begin{pmatrix} A & \partial_t A \\ 0 & A \end{pmatrix}^2 = \begin{pmatrix} A^2 & A\partial_t A + (\partial_t A)A \\ 0 & A^2 \end{pmatrix} = \begin{pmatrix} p_2(A) & \partial_t p_2(A) \\ 0 & p_2(A) \end{pmatrix} \tag{7.18}$$

The generalisation to arbitrary powers is straightforward. Assume the theorem holds for a given power n. Then the result for $n+1$ follows immediately:

$$\begin{aligned} p_{n+1}(\mathcal{B}) &= \begin{pmatrix} A & \partial_t A \\ 0 & A \end{pmatrix}^n \begin{pmatrix} A & \partial_t A \\ 0 & A \end{pmatrix} \\ &= \begin{pmatrix} p_n(A) & \partial_t p_n(A) \\ 0 & p_n(A) \end{pmatrix} \begin{pmatrix} A & \partial_t A \\ 0 & A \end{pmatrix} \\ &= \begin{pmatrix} p_n(A)A & p_n(A)\partial_t A + (\partial_t p_n(A))A \\ 0 & Ap_n(A) \end{pmatrix} \\ &= \begin{pmatrix} p_{n+1}(A) & \partial_t p_{n+1}(A) \\ 0 & p_{n+1}(A) \end{pmatrix} \end{aligned} \tag{7.19}$$

Equations (7.18) and (7.19) make the role of the block matrix for the calculation of the derivative more transparent. By taking the n-th power of the block matrix the sum of all possible permutations of the matrix product consisting of $(n-1)$ times the matrix A and $\partial_t A$, which is precisely the derivative of A^n, appears in the upper right block of the result by virtue of the recursion (7.19). The result for power functions can be directly generalised to polynomials of A and therefore to any analytic function f. A proof for arbitrary (sufficiently smooth) functions can be found in [140].

Using Theorem 1 makes it possible to compute the action of the derivative of a matrix function via

$$f(\mathcal{B}) \begin{pmatrix} 0 \\ |x\rangle \end{pmatrix} = \begin{pmatrix} \partial_t f(A)\,|x\rangle \\ f(A)\,|x\rangle \end{pmatrix}, \tag{7.20}$$

where the left hand side can be evaluated using a matrix function approximation method. In the following the TSL approximation is used, but keep in mind that any other approximation scheme can be applied instead.

7.3.1 *Deflation and Properties of the Block Matrix $\mathcal{B}$*

The convergence properties of a matrix approximation algorithm are in general related to the spectrum of the matrix in question. Calculating the matrix function amounts to evaluating the function for every Jordan block. Considering Equation (7.6) it becomes clear right away that an eigenvalue close to a pole or a branch cut of the function f can cause problems in a numerical algorithm. The sign function in particular has a discontinuity along the imaginary axis. As mentioned above, the efficiency of approximations of the sign function can be greatly improved with deflation methods [135–137]. The idea of the deflation procedure is to compute the eigenvalues of the matrix close to the problematic points and their corresponding eigenvectors. These eigenvectors are projected out from the source vector $|x\rangle$. The approximation is then applied to the new source vector and the function is evaluated exactly on the subspace spanned by the eigenvectors. The important point here is that it is not necessary to compute all eigenvalues of the matrix. The eigenvalues of interest for deflation can be calculated very efficiently with the Arnoldi algorithm, for example by using the `ARPACK` package [141].

In the case of the sign function the m eigenvalues closest to the origin are computed[2] and the evaluation of the sign function is split in the following way

$$\operatorname{sgn}(A)\,|x\rangle = \underbrace{\sum_{i=1}^{m} \operatorname{sgn}(\lambda_i)\,|R_i\rangle\,\langle L_i|\,x\rangle}_{\text{exact}} + \underbrace{\operatorname{sgn}(A) P_m^n\,|x\rangle}_{\text{approximation}}, \tag{7.21}$$

where $|R_i\rangle$ and $\langle L_i|$ are the right and left eigenvectors of A corresponding to the eigenvalue λ_i and $P_m^n = \sum_{i=m+1}^{n} |R_i\rangle\,\langle L_i|$ is a projector onto the space orthogonal to the m eigenvectors.

To visualise how deflation works we plot the sign function of 100 random points from the set $(-1,-\Delta)\cup(\Delta,1)$ together with an approximating polynomial of order 10 for different values of Δ in Figure 7.2. Clearly for the given polynomial order the approximation is better for a larger gap Δ. By treating the eigenvalues close to 0 exactly one effectively increases the gap in the matrix spectrum and an approximation with a given precision will already be achieved by a smaller order polynomial or a smaller Krylov subspace size in the case of the TSL.

If Equation (7.20) is used to calculate the derivative of a matrix function, it is no longer the spectrum of A that is important for the efficiency of the matrix function approximation but the spectrum of $\mathcal{B}(A, \partial_t A)$. Since $\mathcal{B}$ is an upper block matrix $\det(\mathcal{B}) = \det(A)\det(A) = \det(A)^2$ and it immediately follows that the eigenvalues of $\mathcal{B}$ are degenerate and identical to the eigenvalues λ_i of A.

The deflation procedure as described above is based on the spectral decomposition and hence it works only for diagonalisable matrices. The block matrix $\mathcal{B}$, however, is in general not diagonalisable as the following theorem states:

2 For numerical reasons in practical calculations it is advantageous to calculate the eigenvalues with smallest absolute value $|\lambda_i|$ instead of the ones with the smallest absolute real part $|\mathrm{Re}(\lambda_i)|$ [138].

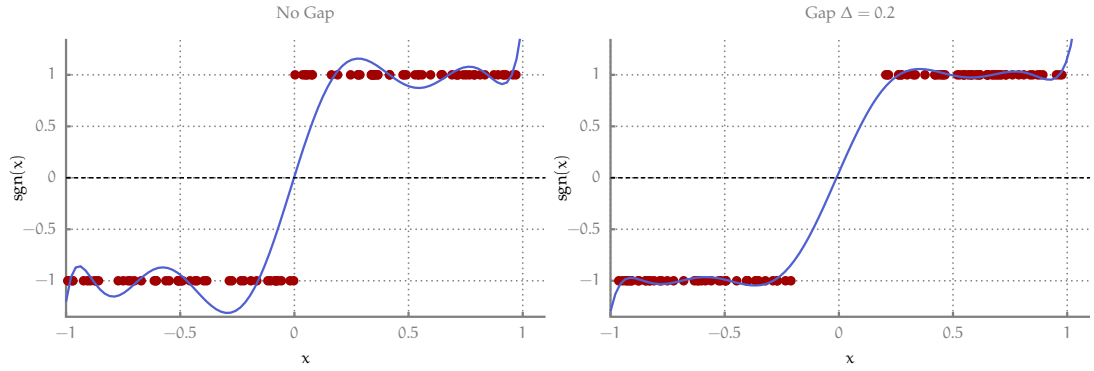

Figure 7.2: Visualisation of the deflation process. The plots show the sign function for 100 random points take from $(-1,-\Delta)\cup(\Delta,1)$ together with an approximating polynomial of order 10. On the left plot $\Delta = 0$ and there are some points very close to the discontinuity at the origin. Consequently a high order polynomial would be needed to approximate the abrupt change in the function. On the right plot the gap is $\Delta = 0.2$ and even the low order polynomial is a good approximation of the sign function.

Theorem 2. *Let A be a diagonalisable matrix. If $\partial_t\lambda_i \neq 0$ for at least one eigenvalue λ_i of A then the matrix $\mathcal{B}$ is not diagonalisable. If A has no degenerate eigenvalues and $\partial_t\lambda_i \neq 0$ for all $i \in \{1,\dots,n\}$ then every Jordan block in the Jordan normal form of $\mathcal{B}$ is of size two, i.e.*

$$\mathcal{J} = \begin{pmatrix} J_1 & 0 & 0 & \dots & 0 \\ 0 & J_2 & \ddots & \ddots & \vdots \\ 0 & \ddots & \ddots & \ddots & 0 \\ \vdots & \ddots & \ddots & \ddots & 0 \\ 0 & \dots & 0 & 0 & J_n \end{pmatrix}, \quad J_i := \begin{pmatrix} \lambda_i & 1 \\ 0 & \lambda_i \end{pmatrix}.$$

A matrix is diagonalisable if and only if its minimal polynomial is a product of *distinct* linear factors. We will now discuss the outline of a proof of Theorem 2. In the following we assume that A has no degenerate eigenvalues to simplify the argumentation. The generalisation to the case of degenerate eigenvalues is possible but a bit more involved. For every eigenvalue λ_i of A we define the two vectors

$$|v_{i,1}\rangle := \begin{pmatrix} |R_i\rangle \\ 0 \end{pmatrix} \quad \text{and} \quad |v_{i,2}\rangle := \begin{pmatrix} |\partial_t R_i\rangle \\ |R_i\rangle \end{pmatrix}, \tag{7.22}$$

where $|\partial_t R_i\rangle$ is the derivative of the eigenvector as defined in Appendix C. It is easy to convince oneself that these vectors are linearly independent and that $|v_{i,1}\rangle$ is an eigenvector of $\mathcal{B}$ to the eigenvalue λ_i. For $|v_{i,2}\rangle$ we have

$$\begin{aligned} \mathcal{B}\,|v_{i,2}\rangle &= \begin{pmatrix} A\,|\partial_t R_i\rangle + (\partial_t A)\,|R_i\rangle \\ A\,|R_i\rangle \end{pmatrix} = \begin{pmatrix} \partial_t(A\,|R_i\rangle) \\ A\,|R_i\rangle \end{pmatrix} \\ &= \begin{pmatrix} \lambda_i\,|\partial_t R_i\rangle + (\partial_t\lambda_i)\,|R_i\rangle \\ \lambda_i\,|R_i\rangle \end{pmatrix} = \lambda_i\,|v_{i,2}\rangle + (\partial_t\lambda_i)\,|v_{i,1}\rangle\,. \end{aligned}$$

The vector $|v_{i,2}\rangle$ is an eigenvector of $\mathcal{B}$ only if $\partial_t\lambda_i$ vanishes. If $\partial_t\lambda_i \neq 0$ we find

$$(\mathcal{B} - \lambda_i\mathbb{1})^2\,|v_{i,2}\rangle = (\partial_t\lambda_i)(\mathcal{B} - \lambda_i\mathbb{1})\,|v_{i,1}\rangle = 0 \tag{7.23}$$

and therefore $|v_{i,2}\rangle$ is a generalised eigenvector of rank two corresponding to the eigenvalue λ_i. From this and the fact that the algebraic multiplicity of the eigenvalue λ_i of $\mathcal{B}$ is two it immediately follows that the multiplicity of λ_i in the minimal polynomial of $\mathcal{B}$ is also two. This proves the first part of Theorem 2.

To see that the second part of Theorem 2 is true, note that for every eigenvalue of A we have at least one Jordan block. Moreover, the size of the largest Jordan block belonging to an eigenvalue λ_i is the multiplicity of the eigenvalue in the minimal polynomial. Therefore, if the eigenvalues are all pairwise distinct there are at least n Jordan blocks of size 2 and since the dimension of $\mathcal{B}$ is $2n$ this proves the Theorem.

Theorem 2 prohibits a straightforward application of the standard deflation procedure (7.21), but also gives us a precise knowledge of the form of the Jordan matrix of $\mathcal{B}$. This allows us to develop a generalised deflation algorithm based on the Jordan normal form. The Jordan decomposition of $\mathcal{B}$ can be written as $\mathcal{X}^{-1}\mathcal{B}\mathcal{X} = \mathcal{J}$ and using Theorem 2 it is possible to derive an analytic expression for $\mathcal{X}$ and $\mathcal{X}^{-1}$ in terms of the eigenvalues and left and right eigenvectors of A and their derivatives.

7.3.1.1 *Jordan decomposition of $\mathcal{B}$*

In practice one never encounters a matrix A with degenerate eigenvalues. Gauge configurations that give rise to a Dirac operator with degenerate eigenvalues are a set of measure zero in the space of all possible gauge configurations. In a Monte Carlo simulation it is therefore very unlikely to encounter them. In addition the Jordan matrix of $\mathcal{B}$ will only become simpler should one or more of the derivatives of the eigenvalues of A vanish. For this reason we assume that every Jordan block of $\mathcal{B}$ is of size two for the rest of this section. The generalisation to the case where some of the Jordan blocks have size one is straightforward.

We start our calculation of the transformation matrix $\mathcal{X}$ by rewriting the Jordan decomposition of $\mathcal{B}$ as

$$\mathcal{B}\mathcal{X} = \mathcal{X}\mathcal{J} \tag{7.24}$$

In bra–ket notation the transformation matrix reads as $\mathcal{X} := (|x_1\rangle, \ldots, |x_{2n}\rangle)$. Evaluating the right hand side of equation (7.24) yields

$$\begin{pmatrix} x_{1,1} & \cdots & x_{1,2n} \\ & & \\ \vdots & & \vdots \\ & & \\ x_{2n,1} & \cdots & x_{2n,2n} \end{pmatrix} \begin{pmatrix} \lambda_1 & 1 & 0 & \cdots & 0 \\ 0 & \lambda_1 & \ddots & \ddots & \vdots \\ \vdots & \ddots & \ddots & \ddots & 0 \\ \vdots & & \ddots & \lambda_n & 1 \\ 0 & \cdots & \cdots & 0 & \lambda_n \end{pmatrix} =$$

$$\begin{pmatrix} \lambda_1 x_{1,1} & x_{1,1} + \lambda_1 x_{1,2} & \cdots & \lambda_n x_{1,(2n-1)} & x_{1,(2n-1)} + \lambda_n x_{1,2n} \\ \vdots & \vdots & & \vdots & \vdots \\ \lambda_1 x_{2n,1} & x_{2n,1} + \lambda_1 x_{2n,2} & \cdots & \lambda_n x_{2n,(2n-1)} & x_{2n,(2n-1)} + \lambda_n x_{2n,2n} \end{pmatrix} \tag{7.25}$$

Combining equations (7.24) and (7.25) leads to n coupled equations

$$\mathcal{B}\,|x_{(2j-1)}\rangle = \lambda_j\,|x_{(2j-1)}\rangle \tag{7.26}$$

$$\mathcal{B}\,|x_{2j}\rangle = |x_{(2j-1)}\rangle + \lambda_j\,|x_{2j}\rangle\,, \tag{7.27}$$

where $j \in \{1, n\}$. Equation (7.26) is just the eigenvalue equation for the matrix $\mathcal{B}$ and is easy to solve. We have already argued that $(|R_j\rangle, 0)^T$ is an eigenvector of $\mathcal{B}$ to the eigenvalue λ_j if $|R_j\rangle$ is an eigenvector of A to the same eigenvalue.

Using the solution of equation (7.26) and defining $|x_{2j}\rangle := (|x_{j,1}\rangle, |x_{j,2}\rangle)^T$ equation (7.27) can be written as

$$\begin{pmatrix} A & \partial_t A \\ 0 & A \end{pmatrix} \begin{pmatrix} |x_{j,1}\rangle \\ |x_{j,2}\rangle \end{pmatrix} = \begin{pmatrix} |R_j\rangle \\ 0 \end{pmatrix} + \lambda_j \begin{pmatrix} |x_{j,1}\rangle \\ |x_{j,2}\rangle \end{pmatrix} \tag{7.28}$$

which simplifies to

$$\begin{aligned} (A - \lambda_j)\,|x_{j,1}\rangle + (\partial_t A)\,|x_{j,2}\rangle &= |R_j\rangle \qquad \text{I} \\ (A - \lambda_j)\,|x_{j,2}\rangle &= 0 \qquad \text{II} \end{aligned} \tag{7.29}$$

Equation II in the system (7.29) is again the eigenvalue equation for A and the solution is simply $|x_{j,2}\rangle = \kappa_i\,|R_j\rangle$, where κ_i is a finite complex number. With this result Equation (I) becomes

$$(A - \lambda_j)\,|x_{j,1}\rangle + (\partial_t A)\kappa_i\,|R_j\rangle = |R_j\rangle\,. \tag{7.30}$$

Let $\{\langle L_j|\}_{j=1,\dots,n}$ denote the set of left eigenvectors of A, i.e. $\langle L_j|\,A = \lambda_j\,\langle L_j|$ and assume the normalisation $\langle L_j|\,R_i\rangle = \delta_{ij}$. By assumption the eigenvalues are not degenerate and $P := \sum_{i \neq j} \frac{|R_i\rangle\langle L_i|}{\lambda_i - \lambda_j}$ is well defined. Multiplying both sides of equation (7.30) by P yields

$$\sum_{i \neq j} |R_i\rangle\,\langle L_i|\,x_{j,1}\rangle = \sum_{i \neq j} \kappa_i \frac{|R_i\rangle\,\langle L_i|}{\lambda_i - \lambda_j} (\partial_t A)\,|R_j\rangle\,. \tag{7.31}$$

The term $\sum_{i \neq j} |R_i\rangle\,\langle L_i|$ on the right hand side of equation (7.31) is a projector to the space $\mathbb{1} - |R_j\rangle\,\langle L_j|$ and using equation (C.9) one finds that the right hand side is equal to $|\partial_t R_j\rangle$. It follows that the projection of $|x_{j,1}\rangle$ is equal to $\kappa_j |\partial_t R_j\rangle$ and therefore

$$|x_{j,1}\rangle = \kappa_j |\partial_t R_j\rangle + \gamma_j\,|R_j\rangle\,, \tag{7.32}$$

where γ_j is a complex number. Note that $|R_j\rangle$ is in the kernel of $(A - \lambda_j)$, which means we can add any scalar multiple of $|R_j\rangle$ to the solution $|x_{j,1}\rangle$ of equation (I) and get another solution. By exploiting this freedom it is possible to set $\gamma_j = 0$. To compute the value of κ_j we simply multiply equation (I) by $\langle L_j|$ from the left. This annihilates the first term on the left hand side and we obtain

$$\kappa_j\,\langle L_j|\,(\partial_t A)\,|R_j\rangle = 1. \tag{7.33}$$

Applying equation (C.6) gives $\kappa_j = 1/\partial_t \lambda_j$. Putting everything together yields an analytic expression for the columns of the matrix $\mathcal{X}$:

$$\begin{aligned} |x_{(2j-1)}\rangle &= \begin{pmatrix} |R_j\rangle \\ 0 \end{pmatrix} \\ |x_{2j}\rangle &= \frac{1}{\partial_t \lambda_i} \begin{pmatrix} |\partial_t R_j\rangle \\ |R_j\rangle \end{pmatrix}. \end{aligned} \tag{7.34}$$

To compute the columns of $\mathcal{X}^{-1}$ we start with the equation

$$\mathcal{X}^{-1}\mathcal{B} = \mathcal{J}\mathcal{X}^{-1}, \tag{7.35}$$

which follows directly from equation (7.24). It turns out that it is more convenient to consider the transpose of this equation

$$\mathcal{B}^{T}\mathcal{Y} = \mathcal{Y}\mathcal{J}^{T}, \tag{7.36}$$

where $\mathcal{Y} := (\mathcal{X}^{-1})^{T}$ is introduced to simplify the notation. The right hand side of equation (7.36) can be written as

$$\begin{pmatrix} y_{1,1} & \cdots & y_{1,2n} \\ \vdots & & \vdots \\ y_{2n,1} & \cdots & y_{2n,2n} \end{pmatrix} \begin{pmatrix} \lambda_1 & 0 & \cdots & \cdots & 0 \\ 1 & \lambda_1 & \ddots & & \vdots \\ 0 & \ddots & \ddots & \ddots & \vdots \\ \vdots & \ddots & \ddots & \lambda_n & 0 \\ 0 & \cdots & 0 & 1 & \lambda_n \end{pmatrix} = \\ \begin{pmatrix} \lambda_1 y_{1,1} + y_{1,2} & \lambda_1 y_{1,2} & \cdots & \lambda_n y_{1,(2n-1)} + y_{1,2n} & \lambda_n y_{1,2n} \\ \vdots & \vdots & & \vdots & \vdots \\ \lambda_1 y_{2n,1} + y_{2n,2} & \lambda_1 y_{2n,2} & \cdots & \lambda_n y_{2n,(2n-1)} + y_{2n,2n} & \lambda_n y_{2n,2n} \end{pmatrix} \tag{7.37}$$

The next steps are analogous to the derivation of the columns of $\mathcal{X}$ above. Let $|y_i\rangle$ be the i—th column of $\mathcal{Y}$, then (7.37) is equivalent to n systems of two equations:

$$\mathcal{B}^{T}\,|y_{2j}\rangle = \lambda_j\,|y_{2j}\rangle \tag{7.38}$$

$$\mathcal{B}^{T}\,|y_{(2j-1)}\rangle = \lambda_j\,|y_{(2j-1)}\rangle + |y_{2j}\rangle, \tag{7.39}$$

Equation (7.38) is an eigenvalue equation and the solution is $|y_{2j}\rangle = \eta_j \left(0, \left|R_j^{T}\right\rangle\right)^{T}$, where $\left|R_j^{T}\right\rangle$ is the eigenvector of A^{T} to the eigenvalue λ_j and η_j is a scalar constant that will be fixed later by requiring $\mathcal{Y}^{T}\mathcal{X} = \mathbb{1}$.

With the notation $|y_{(2j-1)}\rangle := \left(|y_{j,1}\rangle, |y_{j,2}\rangle\right)^{T}$ we can rewrite equation (7.39) as a system of two equations:

$$\begin{aligned} (A^{T} - \lambda_j)\,|y_{j,1}\rangle &= 0 && \text{I} \\ (\partial_t A^{T})\,|y_{j,1}\rangle + (A^{T} - \lambda_j)\,|y_{j,2}\rangle &= \eta_j\,|R_j^{T}\rangle && \text{II} \end{aligned} \tag{7.40}$$

Mimicking the steps used to solve the system (7.29) one finds the following expressions for the columns of $\mathcal{Y}$:

$$\begin{aligned} |y_{(2j-1)}\rangle &= \frac{\eta_j}{\partial_t \lambda_j} \begin{pmatrix} \left|R_j^{T}\right\rangle \\ \left|\partial_t R_j^{T}\right\rangle \end{pmatrix} \\ |y_{2j}\rangle &= \eta_j \begin{pmatrix} 0 \\ \left|R_j^{T}\right\rangle \end{pmatrix}. \end{aligned} \tag{7.41}$$

The rows of the inverse transformation matrix $\mathcal{X}^{-1} = \mathcal{Y}^T$ follow immediately from equation (7.41):

$$\mathcal{X}^{-1} = \begin{pmatrix} \frac{\eta_1}{\partial_t \lambda_1} \left(\langle L_1 | , \langle \partial_t L_1 | \right) \\ \eta_1 \left(0, \langle L_1 | \right) \\ \vdots \\ \frac{\eta_n}{\partial_t \lambda_n} \left(\langle L_n | , \langle \partial_t L_n | \right) \\ \eta_n \left(0, \langle L_n | \right) \end{pmatrix}, \tag{7.42}$$

where we used the fact that $\left| R_j^T \right\rangle^T = \langle L_j |$.

To find the values of the complex constants η_j one has to evaluate the product $\mathcal{X}^{-1}\mathcal{X}$. In this computation one encounters only four different types of bra–ket products, which are all shown in the following matrix product:

$$\begin{pmatrix} \frac{\eta_i}{\partial_t \lambda_i} \left(\langle L_i | , \langle \partial_t L_i | \right) \\ \eta_i \left(0, \langle L_i | \right) \end{pmatrix} \left(\begin{pmatrix} | R_j \rangle \\ 0 \end{pmatrix} , \frac{1}{\partial_t \lambda_j} \begin{pmatrix} | \partial_t R_j \rangle \\ | R_j \rangle \end{pmatrix} \right) = \begin{pmatrix} \frac{\eta_i}{\partial_t \lambda_i} \delta_{ij} & 0 \\ 0 & \frac{\eta_i}{\partial_t \lambda_j} \delta_{ij} \end{pmatrix} \tag{7.43}$$

The entry below the diagonal is trivially zero and the super-diagonal entry vanishes because $\langle L_i | \partial_t R_j \rangle + \langle \partial_t L_i | R_j \rangle = \partial_t \left(\langle L_i | R_j \rangle \right) = \partial_t \delta_{ij} = 0$. With the choice $\eta_i = \partial_t \lambda_i$ the right hand side of equation (7.43) becomes the unit matrix and we finally get

$$\mathcal{X}^{-1} = \begin{pmatrix} \left(\langle L_1 | , \langle \partial_t L_1 | \right) \\ \partial_t \lambda_1 \left(0, \langle L_1 | \right) \\ \vdots \\ \left(\langle L_n | , \langle \partial_t L_n | \right) \\ \partial_t \lambda_n \left(0, \langle L_n | \right) \end{pmatrix} \qquad \text{and} \tag{7.44}$$

$$\mathcal{X} = \left(\begin{pmatrix} | R_1 \rangle \\ 0 \end{pmatrix} , \frac{1}{\partial_t \lambda_1} \begin{pmatrix} | \partial_t R_1 \rangle \\ | R_1 \rangle \end{pmatrix}, \cdots , \begin{pmatrix} | R_n \rangle \\ 0 \end{pmatrix} , \frac{1}{\partial_t \lambda_n} \begin{pmatrix} | \partial_t R_n \rangle \\ | R_n \rangle \end{pmatrix} \right), \tag{7.45}$$

The matrix $\mathcal{X}^{-1}$ consists of $2n$-dimensional row vectors, i.e.

$$\left(\langle L_i | , \langle \partial_t L_i | \right) = \left(\langle L_i |_1 , \ldots , \langle L_i |_n , \langle \partial_t L_i |_1 , \ldots , \langle \partial_t L_i |_n \right). \tag{7.46}$$

Analogously $\mathcal{X}$ is made up by $2n$-dimensional column vectors. With the help of the matrices $\mathcal{X}$ and $\mathcal{X}^{-1}$ we can define a generalised deflation. Let $|x_i\rangle$ be the columns of $\mathcal{X}$ and $\langle \bar{x}_i |$ the rows of $\mathcal{X}^{-1}$, then $\sum_{i=1}^{2n} |x_i\rangle \langle \bar{x}_i | = \mathbb{1}$. We define the projectors $\mathcal{P}_m = \sum_{i=1}^{m} |x_i\rangle \langle \bar{x}_i |$ and $\bar{\mathcal{P}}_m := \mathbb{1} - \sum_{i=1}^{m} |x_i\rangle \langle \bar{x}_i |$, such that for every vector $|\psi\rangle$ we have

$$|\psi\rangle = \mathcal{P}_m |\psi\rangle + \bar{\mathcal{P}}_m |\psi\rangle \tag{7.47}$$

Now we have all the necessary ingredients to define a deflation algorithm for the matrix $\mathcal{B}$. Say we want to deflate the first $2l$ eigenvalues of $\mathcal{B}$ (corresponding to the first l

eigenvalues $\lambda_1, \ldots, \lambda_l$ of A). To calculate $f(\mathcal{B})$ we split the evaluation of the function into two parts:

$$f(\mathcal{B})\,|\psi\rangle = \mathcal{X} f(\mathcal{J}) \mathcal{X}^{-1} \mathcal{P}_{2l}\,|\psi\rangle + f(\mathcal{B})\bar{\mathcal{P}}_{2l}\,|\psi\rangle \tag{7.48}$$

where we used Equation (7.5) for the first term on the right side. To compute the function of the Jordan matrix we only need to consider the function for each Jordan block. Applying Equation (7.6) to the j-th block of $\mathcal{J}$ yields:

$$f(J_i) := \begin{pmatrix} f(\lambda_j) & \partial_t f(\lambda_j) \\ 0 & f(\lambda_j) \end{pmatrix} \tag{7.49}$$

Since the block structure of $\mathcal{J}$ is preserved by the function and the $|x_i\rangle$ and $\langle \bar{x}_i|$ are biorthogonal one finds:

$$\begin{aligned} &\mathcal{X} f(\mathcal{J}) \mathcal{X}^{-1} \mathcal{P}_{2l}\,|\psi\rangle = \\ &\quad \sum_{i=1}^{l} \left[f(\lambda_i) \left(|x_{2i-1}\rangle \langle \bar{x}_{2i-1}|\psi\rangle + |x_{2i}\rangle \langle \bar{x}_{2i}|\psi\rangle \right) + \left(\partial_t f(\lambda_i)\right) |x_{2j-1}\rangle \langle \bar{x}_{2i}|\psi\rangle \right] \end{aligned} \tag{7.50}$$

It is not necessary to compute the full transformation matrices $\mathcal{X}$ and $\mathcal{X}^{-1}$ since the rows and columns needed to evaluate equation (7.50) are known analytically in terms of the left and right eigenvectors of A. The latter can be efficiently computed using the Arnoldi algorithm. In practical calculations one chooses $2l \ll 2n$ and splits the calculation of $f(\mathcal{B})$ in the following way

$$\begin{aligned} f(\mathcal{B})\,|\psi\rangle = \underbrace{f(\mathcal{B})\bar{\mathcal{P}}_{2l}\,|\psi\rangle}_{\text{TSL approximation}} + \\ \underbrace{\sum_{i=1}^{l} \left[f(\lambda_i) \left(|x_{2i-1}\rangle \langle \bar{x}_{2i-1}|\psi\rangle + |x_{2i}\rangle \langle \bar{x}_{2i}|\psi\rangle \right) + \left(\partial_t f(\lambda_i)\right) |x_{2i-1}\rangle \langle \bar{x}_{2i}|\psi\rangle \right]}_{\text{exact}} \end{aligned} \tag{7.51}$$

This looks very similar to the standard deflation formula for diagonalisable matrices. The difference is that now, because the Jordan blocks have size two, there is an additional "mixing term" proportional to $\partial_t f(\lambda_i)$.

In the derivation above we have always implicitly assumed that all calculations can be carried out with infinite precision. In a numerical implementation of the deflation the finite machine precision has to be taken into account. Additionally, it is necessary to find a fast way to compute the derivatives of the eigenvectors needed for the deflation. The numerical aspects of the deflation algorithm are discussed in detail in Appendix E.

For the sign function Equation (7.51) becomes even simpler. The sign function is piecewise constant and for realistic gauge field configurations the eigenvalues of H do not cross the discontinuity line $\mathrm{Re}(z) = 0$ when an external parameter is varied. Therefore, the derivative of the sign function $\partial_t \operatorname{sgn}(\lambda_i)$ is identically zero and the mixing term is absent in the deflation.

An important exception are Hybrid Monte-Carlo simulations with dynamical overlap fermions. In these simulations it is possible that an eigenvalue λ_i of H crosses the discontinuity of the sign function at $\mathrm{Re}\,\lambda_i = 0$, which corresponds to a change of the

topological charge (see Equation (2.53)). If that happens the derivative of $\operatorname{sgn}(\lambda_i)$ in the last term in (7.51) becomes singular. In practical calculations singularities in the Fermionic Force can be avoided by modifying the Molecular Dynamics process in the vicinity of the singularity, for example by using the transmission-reflection step of [142, 143].

7.4 NUMERICAL TEST

7.4.1 *Tuning the TSL Algorithm*

In the last section we developed a method to calculate derivatives of matrix functions with the help of the TSL algorithm. Before this new method is applied to a physical problem it is important to assess its performance and reliability in a well defined test setup. To this end we used quenched $SU(3)$ gauge configurations with different lattice sizes and parameter sets and a Wilson–Dirac operator with an external $U(1)$ gauge field and finite chemical potential. Details of the lattice setup and the analytic expression for the Wilson–Dirac operator and its derivative can be found in Appendix D.

We use a nested version of the TSL algorithm, as described in [138]. Performance tests revealed that the main gains are reached already after a single nesting step and further nesting does not significantly improve the efficiency of the algorithm. For that reason, a single nesting step is used in all our calculations. In this case the TSL algorithm has two adjustable parameters, the sizes of the inner and outer Krylov subspace. It is not known how to compute a priori error estimates for the TSL algorithm and therefore it is a non-trivial question how to chose these parameters in order to achieve a given precision in the approximation.

For the sign function it is possible to calculate an a posteriori estimate for the numerical error ε_A by employing the identity $\operatorname{sgn}(A)^2 = \mathbb{1}$:

$$\varepsilon_A = \frac{\| \operatorname{sgn}(A)^2 |\psi\rangle - |\psi\rangle \|}{2 \, \|\psi\|}, \tag{7.52}$$

where the factor two is added because the TSL has to be applied twice to calculate the square of the sign function.

Equivalently an estimate for the error $\varepsilon_{\mathcal{B}}$ in the computation of the derivative of the sign function can be defined by replacing the matrix A in (7.52) with $\mathcal{B}$ and $|x\rangle$ with the sparse vector $(0, |x\rangle)^T$:

$$\varepsilon_{\mathcal{B}} = \frac{\left\| \operatorname{sgn}(\mathcal{B})^2 \begin{pmatrix} 0 \\ |\psi\rangle \end{pmatrix} - \begin{pmatrix} 0 \\ |\psi\rangle \end{pmatrix} \right\|}{2 \, \||\psi\rangle\|}. \tag{7.53}$$

It is interesting to note that the square of the sign function of the block matrix $\mathcal{B}$ is given by

$$\operatorname{sgn}(\mathcal{B})^2 = \begin{pmatrix} \operatorname{sgn}(A)^2 & \operatorname{sgn}(A)(\partial_t \operatorname{sgn}(A)) + (\partial_t \operatorname{sgn}(A)) \operatorname{sgn}(A) \\ 0 & \operatorname{sgn}(A)^2 \end{pmatrix} \tag{7.54}$$

and that the error estimate $\varepsilon_{\mathcal{B}}$ for the derivative contains the anti-commutator of the $\{\operatorname{sgn}(A), \partial_t \operatorname{sgn}(A)\}$ of the sign function and its derivative:

$$\varepsilon_{\mathcal{B}} = \sqrt{\left(\frac{\| \operatorname{sgn}(A)^2 |\psi\rangle - |\psi\rangle \|}{2 \, \| |\psi\rangle \|} \right)^2 + \left(\frac{\| \{\operatorname{sgn}(A), \partial_t \operatorname{sgn}(A)\} |\psi\rangle \|}{2 \, \| |\psi\rangle \|} \right)^2} \tag{7.55}$$

Typically, the approximating polynomials for the sign function of A and $\mathcal{B}$ are not the same and the first term under the square root in Equation (7.55) is not equal to ε_A^2. The commutator $\{\mathrm{sgn}(A), \partial_t \mathrm{sgn}(A)\} = \partial_t(\mathrm{sgn}(A)^2) = \partial_t \mathbb{1}$ should vanish identically and its deviation from zero can be used as an error measure for the approximation of $\partial_t \mathrm{sgn}(A)$. This approach was used in an earlier work [114], but subsequent numerical studies showed that $\varepsilon_{\mathcal{B}}$ gives a more reliable estimate of the true error of the derivative. Additionally, the anti-commutator is more cumbersome to compute and therefore we will use $\varepsilon_{\mathcal{B}}$ as an error estimate from now on. Calculating the error using equations (7.52) and (7.53) takes one additional evaluation of the sign function per source vector, which would effectively double the run time of the algorithm. In production runs it is not feasible to check the error for every source vector $|x\rangle$ and a more viable method to control the error is needed.

As a rule the optimal values for the Krylov subspace size depends on the matrix and the source vector. The situation is different, however, if deflation techniques are used. In this cast the performance critical parts of the source vector are projected out and treated exactly . It is reasonable to assume that for a given matrix the optimal parameters depend only weakly on the deflated source vectors. It should therefore be possible to find a set of parameters such that the nested TSL gives the desired error for any (deflated) vector.

In order to find the optimal TSL parameters for a given gauge configuration we propose to perform an initial "tunig run" consisting of the following steps:

1. Select the desired precision ε_0.
   (Typically, $\varepsilon_0 = 10^{-8}$ is sufficient for practical calculations)

2. Select a trial vector $|\phi\rangle$.
   The trial vector should be kept fixed during the tuning run in order to make different parameter sets comparable. Additionally, it should be representative for the vectors that will be used in the production runs. We used $|\phi\rangle = (1, \cdots, 1)^T$ to estimate the error ε_A of $\mathrm{sgn}(A)$ and $(0, |\phi\rangle)$ for the error $\varepsilon_{\mathcal{B}}$ of $\mathrm{sgn}(A)$.

3. Choose a set p of trial parameters.
   Let k^O (k^I) be the size of the outer (inner) Krylov subspace size. Then p is given by $p = \{(k_1^O, k_1^I), \cdots, (k_1^O, k_1^I)\}$.

4. For every $p_i \in p$ compute the corresponding error $\varepsilon_i = \varepsilon(p_i)$ and the elapsed CPU time $t_i = t(p_i)$ for the TSL approximation.

5. Discard all p_i for which $\varepsilon_i > \varepsilon_0$

6. From the remaining tuples p_i choose the one for which the elapsed CPU time t_i is minimal.

7. Store the optimal parameters k_{opt}^O and k_{opt}^I found in the last step for use in the production runs.

Be aware that there is no guaranty that for some vector other than the trial vector the parameters k_{opt}^O and k_{opt}^I will give an error smaller than ε_0. To validate the results on can expand the tuning procedure and perform a cross check:

8. Compute the error for l random vectors using the parameters k^{O}_{opt} and k^{I}_{opt}. (In practice $l = 20 - 30$.)

9. Check if the maximal error for all l random vectors is smaller than ε_0.

If the maximal error turns out to be larger than the desired error ε_0 one can restart the tuning run with a different trial vector, for example with the random vector that led to the largest error, to find better estimates for the optimal parameters. Another strategy is to use a smaller value for ε_0 than is actually necessary. Our calculations show that in most cases the largest error for the random vectors is of the same order of magnitude as the error for the trial vector. As a rule of thumb one should therefore choose the target precision $\varepsilon_0/10$ for the trial run to achieve a precision of ε_0.

A different and independent way to check the reliability of the optimal parameter estimates obtained in the trial run is to compare the results of the TSL approximation to some other matrix function approximation algorithm. We have mentioned above that the TSL implicitly constructs a polynomial interpolation of the sign function. The size of the (outer) Krylov subspace corresponds to the order of the approximating polynomial. If we set the chemical potential to $a\mu = 0$ the matrix H is Hermitian and the minimax polynomial approximation [132] can be used to evaluate the sign function.

To compare the minimax polynomial approximation with the TSL algorithm we generated 20 gauge configurations on a lattice of size 8×8^3 and $\beta = 8.1$. The role of the matrix A in is now played by the operator H, which is a matrix of size $n = 49152$ for this lattice size. For the given parameters the spectrum of H has only a small gap around the line $\mathrm{Re}(z) = 0$, which makes it harder to approximate the sign function with a low order polynomial (compare Figure 7.2). For both algorithms the 30 eigenvalues of H with smallest absolute value were deflated.

The mean error is computed by averaging over random vectors and over gauge configurations. In Figure 7.3 the mean error is plotted as a function of the highest power of H in the approximating polynomial. For a fixed polynomial degree the error of the TSL approximation is smaller than the error of the minmax polynomial approximation. The explanation for this result is quite simple and intuitive: The minimax polynomial tries to minimise the maximal error over all possible source vectors, while the TSL method constructs a different optimised polynomial for every source vector.

As the matrix size grows larger the main computational cost for both algorithms is coming from the evaluation of the matrix-vector products. As a result the differences in the time the algorithms spend for the construction of the coefficients of the approximating polynomial becomes negligible. The minimax method internally actually constructs a polynomial in H^2, while the TSL method generates the Krylov subspace for both H and $H^\dagger$. Taking this into account one finds that for a given maximal power of H in the interpolating polynomial the TSL algorithm takes twice as many matrix-vector multiplications as the minmax method. While it is still possible to keep all the Krylov vectors in the RAM for a lattice of size 8×8^3, this is in general not feasible. Therefore, we used a two-pass version of the TSL as described above. As a result one expects that the TSL is roughly four times slower than the minimax algorithm. The CPU time for the two algorithms is plotted in Figure 7.3 and is in very good agreement with this expectation.

The numerical test for configurations of size 8×8^3 confirms our earlier arguments and shows that the error of the (deflated) TSL method does not strongly depend on the source vector. Moreover, the error for a given Krylov subspace size is almost an

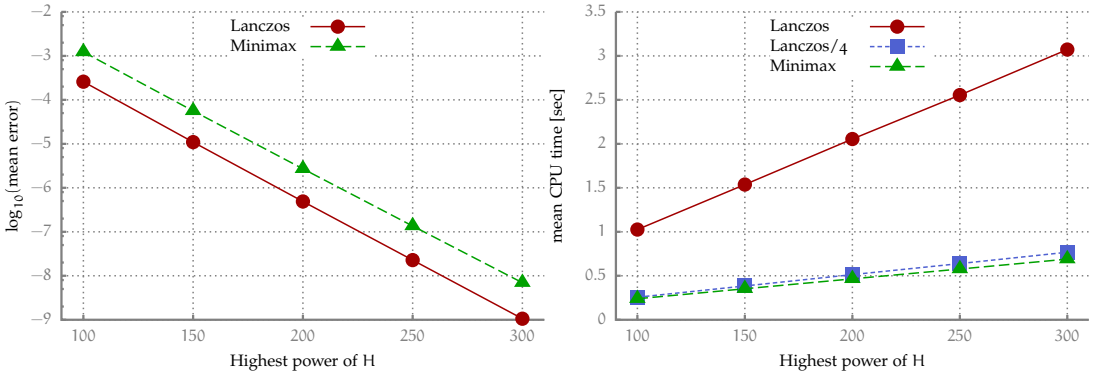

Figure 7.3: Comparison of the TSL approximation with the minmax polynomial method. Left: Logarithm of the mean error of both methods as a function of the highest power of the polynomial. Right: Mean time required for the calculation of $\mathrm{sgn}(H)\,|x\rangle$ on an Intel® Core™ i5-3470 CPU, with multi-core OpenBLAS [144] used for basic linear algebra. As expected the TSL is slower than the minmax polynomial approach by a factor of four.

order of magnitude smaller than a naive comparison with the minimax method would suggest, see Figure 7.3. Building on these findings we use a single tuning run per gauge configuration to find the optimal parameters for the production runs.

7.4.2 *TSL Approximation of the Derivatives of the Matrix Sign Function*

Having developed a reliable tuning prescription for the TSL algorithm, we come back to the problem of computing derivatives of the matrix sign function. Ultimately we are interested in the calculation of the conserved lattice currents for the overlap Dirac operator. For the numerical tests we therefore consider the derivative of the operator H taken with respect to the Abelian lattice gauge field $\Theta_{x,\mu}$ as defined in Appendix D and the block matrix is given by $\mathcal{B} = \mathcal{B}(H, \partial H)$, where $\partial H = \frac{\partial H}{\partial \Theta_{x,\mu}}$.

Figure 7.4 shows results for the estimated error of $\mathrm{sgn}(H)$ and $\mathrm{sgn}(\mathcal{B}(H, \partial H)$ as a function of the outer Krylov subspace size at $a\mu = 0$ with lattice sizes ranging from 4×4^3 ($n = 3072$) to 14×14^3 ($n = 460992$). In most of the plots the positive effects of the deflation procedure are clearly visible. The one exception is the configuration with $V = 6 \times 18^3$ and $\beta = 8.45$. For this setup the temperature is above the deconfinement transition temperature for the Lüscher-Weisz action (see for example [145]) and the spectrum of H already has a large gap around the line $\mathrm{Re}(z) = 0$. Widening the gap further only leads to a relatively small improvement of the efficiency of the TSL approximation.

Interestingly deflation has an additional positive side effect in the case of the derivative computation. The source vector that is used as an input for the calculation of the derivative has a vanishing upper part. Additionally, the derivative matrix ∂H is very sparse, since in lattice QCD a single link only affects two lattice sites (see Equation (D.3)). For this reason the Krylov vectors constructed in the TSL algorithm have a sparse upper part and the Krylov subspace is not a good approximation of the full space. For the deflation the vectors corresponding to the eigenvalues close to the zero are projected out from the source vector and in general the deflated source vector will not be sparse. The Krylov subspace of the deflated source vector has a more general form, which has a positive influence on the convergence rate of the TSL method.

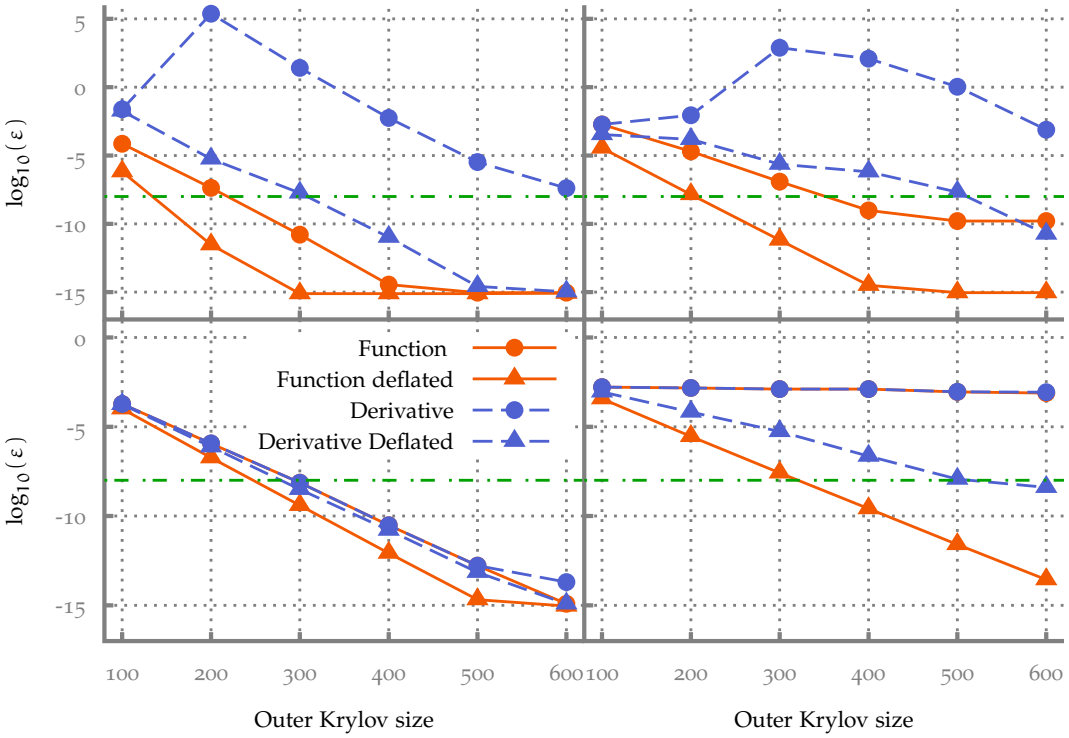

Figure 7.4: Matrix size dependence of the optimal outer Krylov subspace size for zero chemical potential. The green, dash-dotted line marks the desired error of 10^{-8}. (Un-)deflated results are marked by (circular) triangular Symbols. The data points are connected with lines to guide the eye. A solid line stands for the sign function results while a broken line indicates the results for the derivative. Clockwise from top left the results are shown for 4×4^3, 6×6^3, 14×14^3 and 6×18^3 lattices. For 4×4^3, 6×6^3, 14×14^3 lattices we used $\beta = 8.1$ ($a = 0.125\,\mathrm{fm}$) and for 6×18^3 lattice we used $\beta = 8.45$ ($a = 0.095\,\mathrm{fm}$). The inner Krylov subspace size is set to 100 in all plots. For the deflation of the sign function we use the 40 eigenvalues with the smallest magnitude. To deflate the derivative, we used two eigenvalues for 4×4^3, 6×6^3 and 6×18^3 lattices and six eigenvalues for 14×14^3.

Another observation from Figure 7.4 is that the TSL scales very well with the lattice volume V. The size of the Krylov subspace needed to achieve a given error only slightly increases with V. It is also of interest to study the dependence of the optimal Krylov subspace size on the chemical potential. As μ is increased the matrix H differs more and more from a Hermitian matrix and the expectation is that a larger Krylov subspace size is necessary to obtain the desired precision. Figure 7.5 shows the results for test runs at different values of μ. The plots in Figure 7.4 and Figure 7.5 indicate that for $a\mu = 0$ and $V = 14 \times 14^3$ an outer Krylov subspace size of 500 is sufficient to achieve an error of 10^{-8} for the deflated derivative. If the chemical potential is increased to $a\mu = 0.05$ a subspace size of approximately 600 has to be used for the same error. For $a\mu = 0.30$ it seems that an error of 10^{-8} can be obtained by increasing the subspace size to 650. Comparing the relative changes in the Krylov subspace size we find that it is necessary to increase the subspace size by about 20% when going from vanishing chemical potential to $a\mu = 0.05$. Once the chemical potential is switched on the further increase in the optimal Krylov subspace size is not that dramatic. Between $a\mu = 0.05$ and the relatively large value $a\mu = 0.30$ the Krylov size grows by approximately 10%.

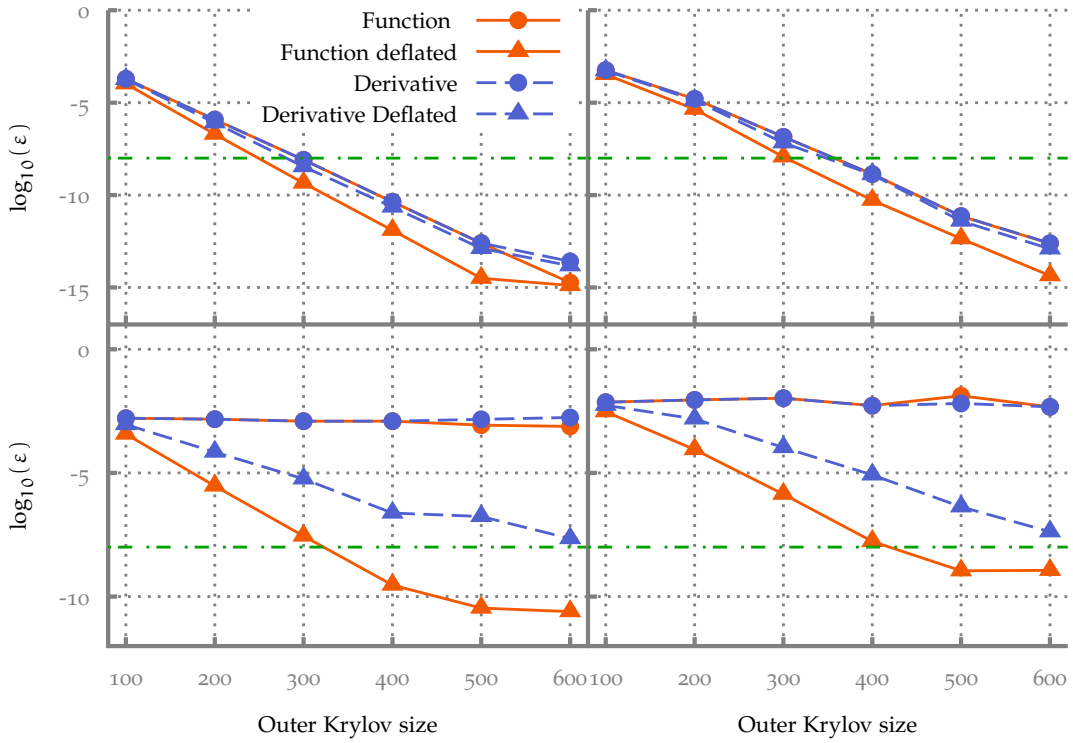

Figure 7.5: Chemical potential dependence of the error as a function of the outer Krylov subspace size. Top: $V = 6 \times 18^3$ and $a\mu = 0.04$ on the left and $a\mu = 0.23$ on the right. Bottom: $V = 14 \times 14^3$ and $a\mu = 0.05$ on the left and $a\mu = 0.30$ on the right. All other parameters are the same as for Figure 7.4.

For the $V = 8 \times 16^3$ configuration the picture is a bit different. Switching on a small chemical potential has only a negligible effect on the error for a given Krylov subspace size. For larger values of the chemical potential it is necessary to use a larger Krylov subspace to obtain the desired error and for $a\mu = 0.23$ the size is around 350. Compared to the Krylov subspace size of 280 at $a\mu = 0$ this is an increase of roughly 25%.

In summary, we find that the Krylov subspace size necessary to obtain the desired precision does indeed depend on the value of the chemical potential. Even for comparatively large values of μ the relative growth of the optimal Krylov subspace size does not exceed 25% and in practical calculations this should not pose a problem.

7.4.3 *A Physical Test Case - The Divergence of the* $U(1)$ *Vector Current*

Finally we consider a test case for our numerical derivative method that is more practice-oriented, namely the computation of the divergence of the $U(1)$ vector current

$$\delta j_x = \sum_\mu \left(j_{x,\mu} - j_{x-\mu,\mu} \right). \tag{7.56}$$

To perform the test we randomly pick a single configuration from an ensemble of equilibrium gauge configurations. For this fixed configuration we calculate δj_x for a randomly chosen lattice site x.

The invariance of the lattice Dirac operator under the gauge transformations $\Theta_{x,\mu} \to \Theta_{x,\mu} + \phi_x - \phi_{x+\mu}$ gives rise to a conserved (Noether) vector current. Hence the di-

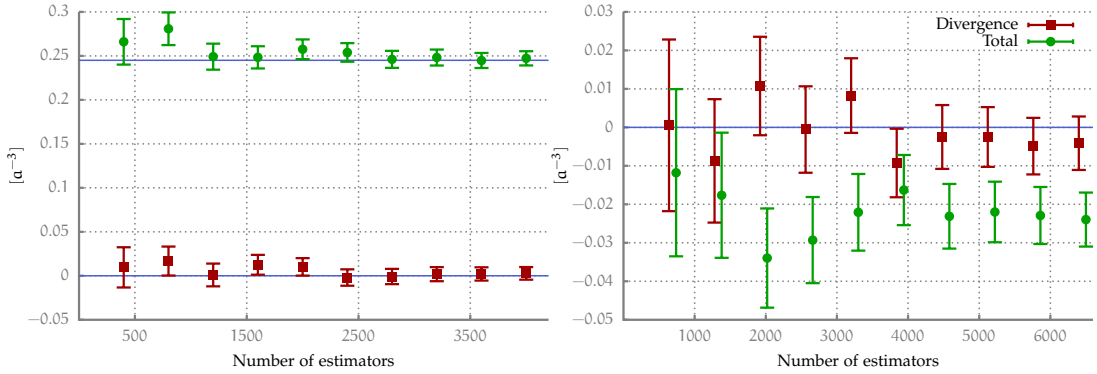

Figure 7.6: Results for divergence (red squares) of the vector current and the total current (green circles) at a lattice site for configurations with $\beta = 8.1$ and $a\mu = 0.30$, plotted as functions of the number of stochastic estimators. Left: For this small configuration with $V = 3 \times 4^3$ the exact values can be computed and are indicated by solid blue lines. Right: Here $V = 6 \times 6^3$ and it is not feasible to compute the exact values. The results for the total current are shifted by 100 estimators to the right for better visibility and the blue line marks zero.

vergence (7.56) has to vanish on physical grounds. For the overlap Dirac operator the expectation value of the conserved vector current (7.1) is given by

$$\begin{aligned}\langle j_{x,\mu}\rangle &= \operatorname{tr}\left(D_{ov}^{-1}\frac{1}{2}\left(K_{x,\mu} - \gamma_5 K_{x,\mu}\gamma_5(1 - D_{ov})\right)\right)\\ &= \operatorname{tr}\left(D_{ov}^{-1}\frac{\partial D_{ov}}{\partial \Theta_{x,\mu}}\right),\end{aligned} \tag{7.57}$$

where we used the Ginsparg–Wilson equation and the fact[3] that $\partial_\Theta \operatorname{tr}(D\gamma_5) = 2\partial_\Theta Q = 0$ to simplify the expression.

On small lattices the trace in Equation (7.57) can be evaluated exactly, but for larger lattice volumes this becomes unfeasible. A standard method to calculate an estimate for the trace of large matrices is the so-called stochastic estimation. The trace of a matrix $A \in \mathbb{C}^{n\times n}$ is defined as

$$\operatorname{tr}(A) = \sum_{i=1}^{n} \langle i|A|i\rangle, \tag{7.58}$$

where any orthonormal basis of $\mathbb{C}^{n\times n}$ can be used for the vectors $|i\rangle$. For the stochastic estimation of the trace one constructs l random vectors $|\eta_1\rangle, \cdots, |\eta_l\rangle$ of dimension n which obey the following constraints

$$\begin{aligned}\left\langle \eta^i \right\rangle_s &= 0 \qquad \text{and}\\ \left\langle \eta^i \eta^j \right\rangle_s &= \delta_{ij},\end{aligned} \tag{7.59}$$

where $\langle\cdots\rangle_s$ is the stochastic expectation value defined as $\left\langle \eta^i \right\rangle_s := \frac{1}{l}\sum_{k=1}^{l} \eta_k^i$ with η_k^i being the i-th component of the random vector $|\eta_k\rangle$. The stochastic estimator for the trace of A is given by

$$\operatorname{tr}(A) \approx \frac{1}{l}\sum_{k=1}^{l} \langle \eta_k|A|\eta_k\rangle. \tag{7.60}$$

3 The topological charge Q is constant for smooth variations of the field $\Theta_\nu(x)$.

In the limit $l \to \infty$ this equation becomes exact. The error that is made for a finite value of l depends to some amount on the properties of the random vectors. In our calculations we use stochastic estimators with Z_2-noise, where the entries of the random vectors are chosen randomly from the set $\{1, -1\}$ [146].

As an additional check we also computed the "total current" at the lattice site x, which is defined as the sum over incoming and outgoing currents. The total current is calculated by simply changing the minus to a plus sign in Equation (7.56). This quantity has no physical meaning and its value is not constrained. If the total current is finite an exact cancellation is necessary to render the divergence zero. Finding numerically that divergence vanishes while the total current is finite can be seen as an additional cross check.

Figure 7.6 shows results for the divergence and the total current as a function of the number of stochastic estimators for two gauge configurations of different size. The error bars in the plots show the standard estimate for the error of the sample mean. In both plots we observe that the total current is finite, while the value of the divergence is consistent with zero.

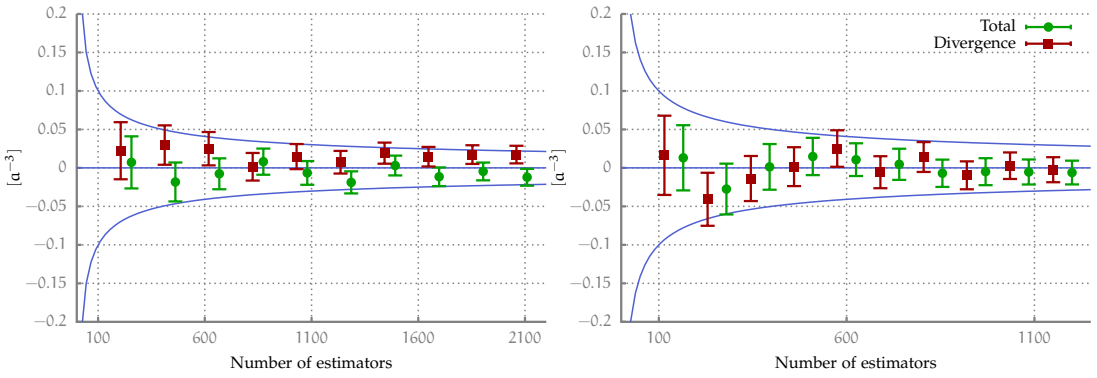

Figure 7.7: Results for divergence and the sum of the vector current at a lattice site for large lattices, plotted as functions of the number n_e of stochastic estimators. Left $V = 6 \times 18^3$ with $\beta = 8.45$, right $V = 14 \times 14^3$ with $\beta = 8.1$. The chemical potential is $a\mu = 0$ for both plots. The results for the total current are shifted by 50 estimators to the right for better visibility. The straight blue line marks zero and the curved blue lines depicting $\pm 1/\sqrt{n_e}$ are drawn to visualise the error dependence on the number of estimators.

In Figure 7.7 we present results for configurations with a larger volume. The calculation of the stochastic estimators is numerically very expensive, even for relatively small lattice sizes. For the larger lattices we therefore consider only the numerically less demanding case $a\mu = 0$. The divergence as well as the total current turn out to be very small for both configurations. A much larger number of stochastic estimators would be needed to see a clear separation of the two quantities within error bars. Even so, we find that for both configurations the divergence is consistent with zero. Moreover, the error bars evidently show the expected inverse square root dependence on the number of stochastic estimators.

8

THE CHIRAL SEPARATION EFFECT IN DENSE QCD

In the last chapter we developed a numerical differentiation method for matrix functions and presented a tuning prescription for the TSL algorithm. Using these tools we can now finally study the CSE in QCD on the lattice.

At low temperatures and densities the chiral symmetry of QCD is broken by a finite chiral condensate and non-perturbative corrections to the CSE current (3.4) are expected to occur. For a sufficiently small chemical potential the changes to the transport coefficient σ_{CSE} can be expressed in terms of the in-medium amplitude $g_{\pi^0\gamma\gamma}$ of the $\pi^0 \to \gamma\gamma$ decay [12]:

$$\sigma_{\mathrm{CSE}} = \sigma^0_{\mathrm{CSE}}(1 - g_{\pi^0\gamma\gamma}), \tag{8.1}$$

where σ^0_{CSE} is the universal value. For continuum QCD with $N_f = 1$ quark flavour it is given by

$$\sigma^0_{\mathrm{CSE}} = \frac{q N_c \mu}{2\pi^2}, \tag{8.2}$$

where $N_c = 3$ is the number of colours and q is the charge of the quark.

In the high-temperature phase of QCD chiral symmetry is restored. The transport coefficient in this phase is the same as for free quarks and $g_{\pi^0\gamma\gamma} = 0$ [8, 9, 12]. So far there are no first-principle QCD calculations of $g_{\pi^0\gamma\gamma}$ in the the phase with broken chiral symmetry. Computations within the linear sigma model yield [12, 147, 148]

$$g_{\pi^0\gamma\gamma} = \frac{7\zeta(3)m^2}{4\pi^2 T^2}, \tag{8.3}$$

where m is the constituent quark mass and ζ is the Riemann ζ-function. In the linear sigma model the constituent quark mass is a free parameter. A realistic description of the low energy spectrum of QCD can be achieved if it is set to $m \sim 300$ MeV [149]. If we plug $m = 300$ MeV into Equation (8.3) we find that even at a relatively large temperature of $T \sim 150$ MeV the term $g_{\pi^0\gamma\gamma}$ is still of order of $\mathcal{O}(1)$. The linear sigma model therefore predicts large corrections to the CSE current in the phase with spontaneous chiral symmetry breaking. The aim of our lattice simulations is to test this prediction and to provide a model independent, first-principle calculation of the corrections to σ_{CSE} in QCD.

8.1 NUMERICAL SETUP

Before we discuss our results, we briefly describe the lattice setup and the numerics used in our calculations. Our quenched $SU(3)$ gauge configurations were generated using the same parameters as for the test runs in the last chapter, see Appendix D for details.

To study the CSE current it is necessary to work with a finite (external) magnetic field. We followed the prescription in [150] to introduce a constant and homogeneous external magnetic field in our simulations. On the lattice the quantisation of the magnetic flux leads to the quantisation condition

$$qB = \frac{2\pi\Phi_B}{L_s^2}. \tag{8.4}$$

Additionally, the periodicity of the lattice gauge field restricts the value of the magnetic flux quantum to $0 \leqslant \Phi_B < L_s^2$. Simulations with a homogeneous magnetic field can therefore only be performed at specific values of qB for a given L_s.

A big advantage of using conserved currents for the overlap operator is that they are protected from renormalisation at zero quark mass. Therefore, they can be directly related to the continuum currents. We have already discussed the expectation value of the conserved vector current in Section 7.4.3. The analogous expression for the expectation value of the conserved axial current (7.2) reads as

$$\left\langle j^A_{x,\mu} \right\rangle = \operatorname{tr}\left(D_{ov}^{-1} K_{x,\mu}\gamma_5\right), \qquad K_{x,\mu} = \frac{\partial D_{ov}}{\partial \Theta_{x,\mu}}. \tag{8.5}$$

To improve the statistics of our result for the CSE current we computed the average axial current over all lattice sites x, which is given by

$$\left\langle j^A_{\mu} \right\rangle = \frac{1}{V}\sum_x \left\langle j^A_{x,\mu} \right\rangle = \frac{1}{V}\sum_x \operatorname{tr}\left(D_{ov}^{-1} K_{x,\mu}\gamma_5\right) = \frac{1}{V}\operatorname{tr}\left(D_{ov}^{-1}\sum_x K_{x,\mu}\gamma_5\right), \tag{8.6}$$

where we have exploited the linearity of the trace in the last step. The operator $\sum_x K_{x,\mu}$ is sparse and can be constructed in a straight forward way using (D.3). Since just a single trace has to be evaluated the calculation of $\left\langle j^A_{\mu} \right\rangle$ is only insignificantly more expensive than the computation of $\left\langle j^A_{x,\mu} \right\rangle$.

The trace in Equation (8.6) was calculated using the stochastic estimator method (7.60). For every stochastic estimator the inverse of D_{ov} has to be computed. To evaluate the action of the inverse overlap operator on a source vector $|\eta\rangle$ we used the identity

$$D_{ov}^{-1}|\eta\rangle = D_{ov}^{\dagger}(D_{ov}D_{ov}^{\dagger})^{-1}|\eta\rangle \tag{8.7}$$

and applied the Conjugate Gradient (CG) algorithm to the Hermitian operator $D_{ov}D_{ov}^{\dagger}$. Most of the CPU time in our calculations was spent in the CG algorithm and we therefore used a deflation method to speed up the inversions. To this end we calculated the 30 eigenvalues with smallest absolute value $\bar{\lambda}_i$ and the corresponding eigenvectors $|\bar{\lambda}_i\rangle$ of $D_{ov}D_{ov}^{\dagger}$ with `ARPACK` [141] and evaluated the inverse exactly on the subspace spanned by these eigenvectors:

$$(D_{ov}D_{ov}^{\dagger})^{-1}|\eta\rangle = \underbrace{\sum_j^{30}\frac{1}{\bar{\lambda}_j}|\bar{\lambda}_j\rangle\langle\bar{\lambda}_j|\eta\rangle}_{\text{exact}} + \underbrace{(D_{ov}D_{ov}^{\dagger})^{-1}P|\eta\rangle}_{\text{CG}}, \tag{8.8}$$

with the projector $P = \mathbb{1} - \sum_j^{30}|\bar{\lambda}_j\rangle\langle\bar{\lambda}_j|$. The eigenvalues and eigenvectors were calculated once for every gauge configuration and stored, so that they could be reused for all stochastic estimators.

The knowledge of the eigenvalues $\bar{\lambda}_i$ makes it possible to compute the topological charge of our gauge configurations via Equation (2.53). It is straight forward to show that the number of zero modes of $D_{ov}D_{ov}^{\dagger}$ is exactly the same as the number of zero modes of D_{ov}. For realistic gauge configurations it never occurs simultaneously that $n_+ \neq 0$ and $n_- \neq 0$, see for example the discussion in [22, Chapter 7]. By simply counting the number of zero modes of $D_{ov}D_{ov}^{\dagger}$ we therefore immediately obtain the absolute value of Q.

Obviously, for massless quarks the expectation value (8.6) is only well defined if $Q = 0$, since the massless overlap Dirac operator is not invertible for $Q \neq 0$. Our calculations for vanishing quark mass are therefore restricted to fixed topology $Q = 0$.

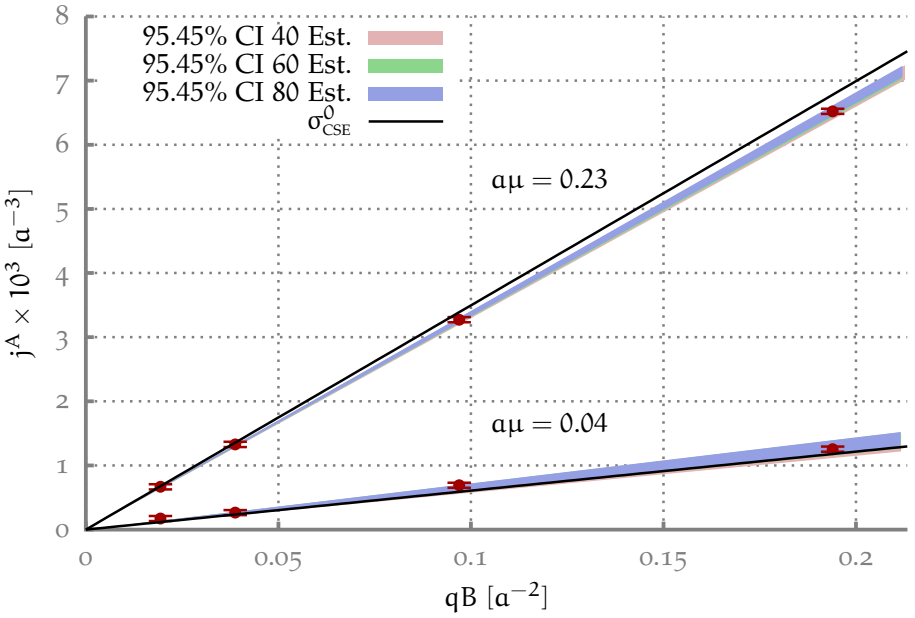

Figure 8.1: The axial current as a function of the magnetic field strength for topological charge $Q = 0$ at $T > T_c$. The red dots with error bars denote our data for 80 stochastic estimators and the shaded regions show the bootstrap confidence intervals for σ_{CSE} for different numbers of estimators.

For each of the lattices with $V = 6 \times 18^3$ and $V = 14 \times 14^3$ we generated about 10^3 gauge configurations. From these configurations we randomly chose 100 with $Q = 0$ for our calculations with vanishing quark mass. Moreover, we picked 100 configurations with $|Q| = 1$ for the $V = 6 \times 18^3$ lattice and for the $V = 14 \times 14^3$ lattice 111 configurations with $|Q| = 1$ and 97 with $|Q| = 2$. For the computations on configurations with $|Q| > 0$ we introduced a small but finite quark mass $am_q = 0.001$.

The calculations for the smaller $V = 8 \times 8^3$ lattice are considerably cheaper than for the larger lattices. It is therefore viable to work with a larger number of configurations. We generated around $5 \cdot 10^3$ gauge configurations for the small lattice. From these we randomly chose 200 configurations with $Q = 0$, $|Q| = 1$ and $|Q| = 2$. To investigate the quark mass dependence of the conductivity σ_{CSE} we considered a vanishing quark mass, $am_q = 0.001$, and $am_q = 0.002$ for the small lattice.

We stress again that we did not explicitly compute the chirality of the zero modes of the overlap operator and therefore only know the absolute value of the topological charge Q for our configurations.

The conductivity σ_{CSE} is given by the slope of the axial current as a function of the external magnetic field. It can be found by fitting a linear function to our axial current data. At $a^2 qB = 0$ the CSE current vanishes and thus the offset is fixed to zero and the fit has only one parameter. The confidence intervals for σ_{CSE} were computed with the statistical bootstrap. For the same gauge configuration axial current results for different values of Φ_B are strongly correlated. Therefore, independent samples for every value of Φ_B are drawn for the bootstrap fits.

8.2 RESULTS

8.2.1 *High Temperature*

First we present the results for the high temperature phase. For the lattice setup with $V = 6 \times 18^3$ and $\beta = 8.45$ the temperature $T = 346$ MeV is higher than the critical temperature T_c for the deconfinement transition of the Lüscher–Weisz action. At this temperature the chiral symmetry should be at least partially restored[1]. As mentioned above no corrections to the CSE are expected in this case.

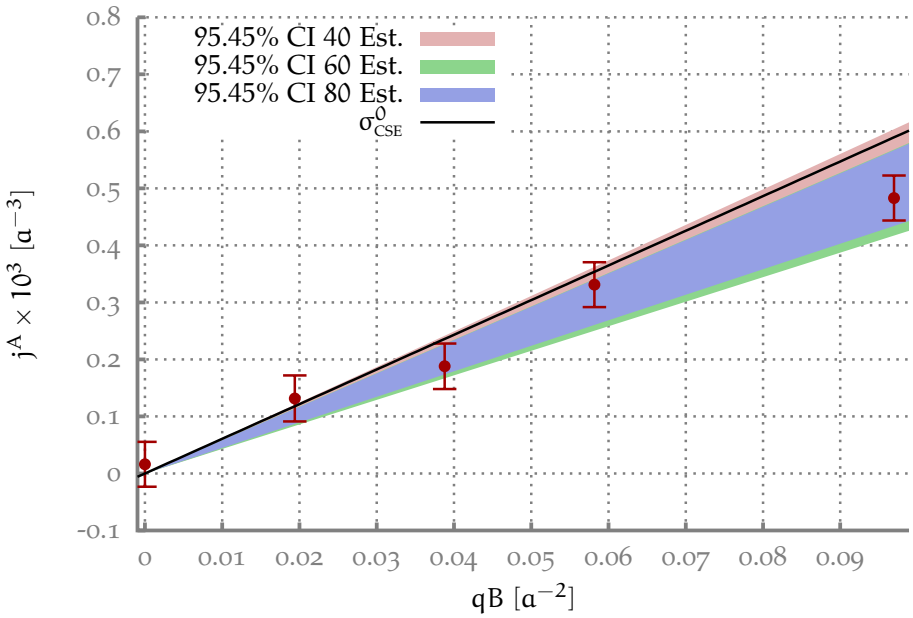

Figure 8.2: The axial current as a function of the magnetic field strength for topological charge $|Q| = 1$ and $a\mu = 0.04$ at $T > T_c$ for a quark mass $am_q = 0.001$. The red dots with error bars denote our data and the shaded regions show the bootstrap confidence intervals for σ_{CSE} computed with different numbers of stochastic estimators. Note that the scale is different than in Figure 8.1.

In Figure 8.1 we plot our results for the axial current as a function of qB at $\Phi_B = 1, 2, 5, 10$ for two values $a\mu = 0.04, 0.23$ of the chemical potential. The outcome of our calculations depends on the number of stochastic estimators used in the trace calculation. To ensure that the final results are not affected by the way we compute the trace we

1 For a discussion of the restoration of chiral symmetry in the high temperature phase of quenched QCD we refer to [151, 152].

increased the number of stochastic estimators until the bootstrap confidence intervals converged. The shaded regions in the plot show the bootstrap confidence intervals for σ_{CSE} for a different number of estimators. The error bands for 40, 60 and 80 stochastic estimators already lie on top of each other. Our results can therefore no longer be improved by using more estimators to compute the trace.

In general, we find a good agreement between the free fermion result σ^0_{CSE} and our data. The one exception is the data point for $a\mu = 0.23$ and $\Phi_B = 10$, where the chemical potential and the magnetic flux are quite large. It is possible that we observe the onset of a saturation effect for these parameters.

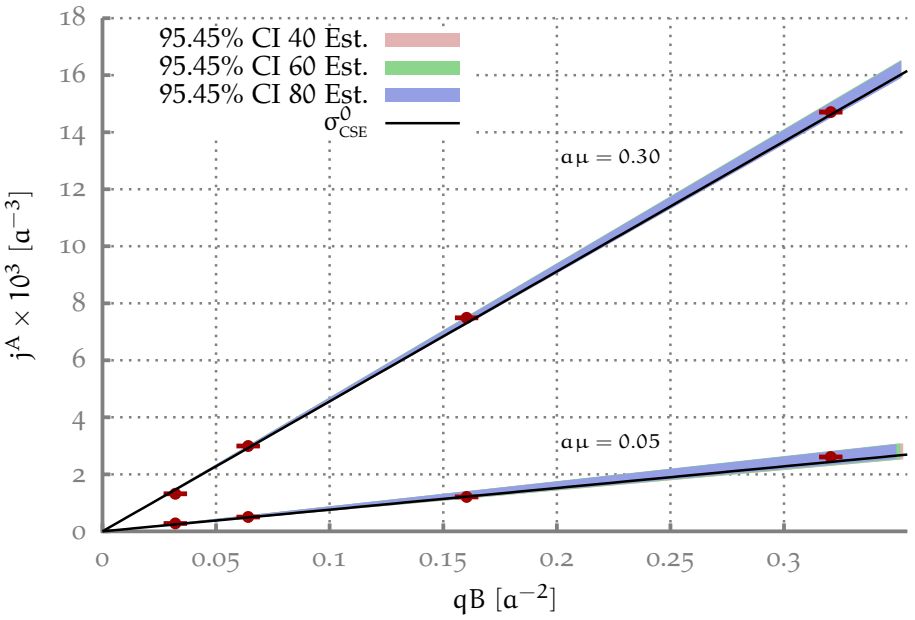

Figure 8.3: The axial current as a function of the magnetic field strength for topological charge $Q = 0$ at $T < T_c$ for the lattice $V = 14 \times 14^3$. The red dots with error bars mark the results for 80 stochastic estimators. The shaded regions show the bootstrap confidence intervals for σ_{CSE} computed with different numbers of estimators.

By working at fixed topology we made a systematic error and it is important to investigate possible effects of a nonzero topological charge on the CSE current. To this end we additionally computed the axial current for configurations with $|Q| = 1$ at $\Phi_B = 0, 1, 2, 3, 5$ for $a\mu = 0.04$. We introduced a small finite quark mass $am_q = 0.001$ to make the overlap operator invertible. The results are shown in Figure 8.2 and again the bootstrap confidence intervals for the slope show good agreement with σ^0_{CSE}. For this setup we performed an additional cross check and also calculated the axial current for $\Phi_B = 0$. As expected the result is consistent with a vanishing axial current for $a^2 qB = 0$.

To take a possible saturation effect for large magnetic flux into account we performed additional fits where the data for the largest magnetic flux was left out for all the lattice setups we considered. The results for the bootstrap confidence intervals are summarised in Figure 8.6. For the configurations with $Q = 0$ as well as for the configurations with $|Q| = 1$ and $am_q = 0.001$ we find that our results are consistent with the value σ^0_{CSE} within statistical errors. We observe that the signal-to-noise ratio of our measurements is better for larger values of the chemical potential. At $a\mu = 0.23$ the relative error of the

slope measurement is smaller than 10%, even if we leave out the data point for $\Phi_B = 10$ in our fits.

8.2.2 *Low Temperature*

In this section we discuss our results for the low temperature phase of QCD, where the chiral symmetry is spontaneously broken. The setup with $V = 14 \times 14^3$ and $\beta = 8.1$ corresponds to a temperature $T = 113$ MeV, which is considerably lower than T_c. The linear sigma model result (8.3) suggests that there should be large corrections to σ_{CSE} in this phase.

In Figure 8.3 we show our results[2] for $Q = 0$, $am_q = 0$, $\Phi_B = 1, 2, 5, 10$ and $a\mu = 0.05, 0.30$. Again we increased the number of stochastic estimators until the bootstrap confidence intervals became stable. Contrary to the expectation our results for σ_{CSE} are in very good agreement with the universal value σ^0_{CSE} and we do not observe any corrections to the anomalous transport coefficient. The confidence intervals for σ_{CSE} are very small, see Figure 8.6, and for the best fit at large chemical potential the relative error of the slope is smaller than 6%.

For this parameter set we do not observe any saturation of the axial current, even for the highest value of the chemical potential and magnetic field strength we considered.

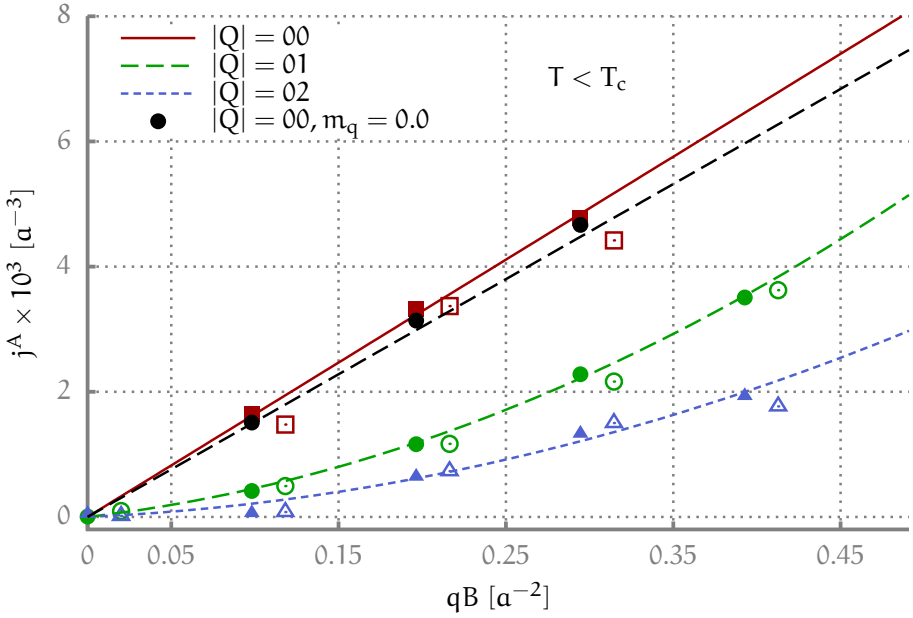

Figure 8.4: The axial current in different topological sectors for the $V = 8 \times 8^3$ lattice. Filled symbols denote the results for $am_q = 0.001$. The results for $am_q = 0.002$ are shifted by $0.02/a^2$ in the qB direction for better visibility and are marked by open symbols. For comparison we plot the results for the axial current for vanishing quark mass at $Q = 0$ as black dots. The black dashed line corresponds to the free continuum result σ^0_{CSE}. To guide the eye a linear ($Q = 0$) or second order polynomial ($|Q| > 0$) fit to the data is shown. The error bars are smaller than the symbols and are not plotted.

2 One of the configurations with the parameters $a\mu = 0.05$ and $\Phi_B = 1$ caused a serious breakdown in the Lanczos algorithm in the computation of the overlap operator. Only the remaining 99 configurations were used for this parameter set.

The computations for the large lattice in the low temperature phase are numerically very expensive. For a first study of the CSE in different topological sectors we therefore considered a smaller lattice with $V = 8 \times 8^3$ with $\beta = 8.1$ and $T = 197$ MeV and only one chemical potential $a\mu = 0.10$. The results for the axial current in this setup are shown in Figure 8.4.

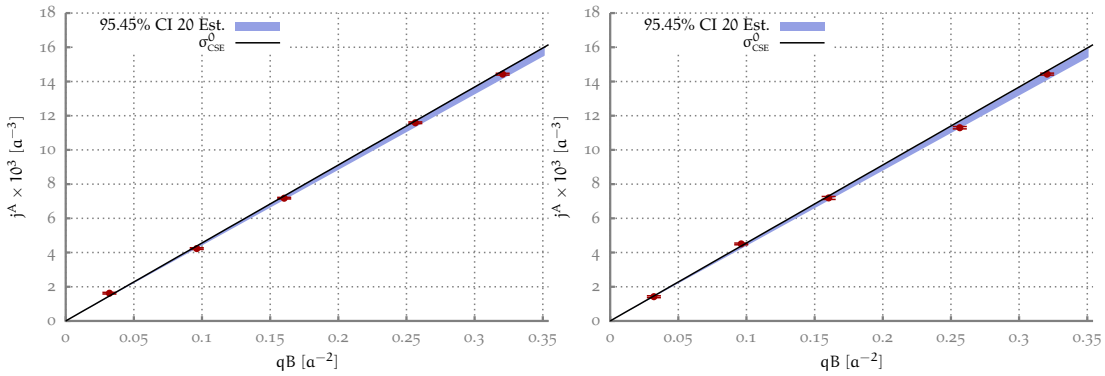

Figure 8.5: The axial current as a function of the magnetic field strength in sectors with nonzero topological charge for the lattice with $V = 14 \times 14^3$ at $T < T_c$. On the left plot $|Q| = 1$ and on the right $|Q| = 2$. The red dots show the results for 20 stochastic estimators and the shaded region is the corresponding bootstrap confidence interval for σ_{CSE}.

In the topological sector with $Q = 0$ we studied the axial current for zero quark mass and for $am_q = 0.001, 0.002$. The data for all three quark masses are in good agreement with the free fermion result σ^0_{CSE} and it seems that finite-volume effects are very small for the CSE current.

On the gauge configurations with nonzero topological charge $|Q| = 1$ and $|Q| = 2$ we observe a strong suppression of the axial current. Moreover, the dependence of the axial current on the magnetic field is no longer linear. We fitted a second order polynomial to the data and the results suggest that there is still a finite slope for small qB, which is much smaller than σ^0_{CSE}. At larger values of qB the non-linear effects seem to be dominant.

In all topological sectors we find that the axial current practically does not depend on the quark mass m_q. At finite quark mass the axial current is no longer protected from renormalisation and strictly speaking it should not be directly compared with the continuum result. For our data, however, we do not see any effects related to a finite quark mass. For the very small quark masses used in our calculations ($m_q = 1.6, 3.2$ MeV in physical units) the renormalisation of the axial current seems to be negligible.

To gain a better understanding of the role of topology for the CSE we separately computed the contributions

$$\left\langle \psi^0_k \right| D^{-1}_{ov} \sum_x K_{x,\mu} \gamma_5 \left| \psi^0_k \right\rangle \tag{8.9}$$

of the "topological modes" $\left|\psi^0_k\right\rangle$ to the CSE current. We define the topological modes $\left|\psi^0_k(m_q)\right\rangle$ for $k = 1, \cdots, |Q|$ as the eigen modes of the massive overlap Dirac operator that become zero modes in the limit $m_q \to 0$. After subtracting the contribution from the topological modes we find that the axial current becomes a linear function of qB again. The slope is given by σ^0_{CSE} and we recover the free fermion result once more.

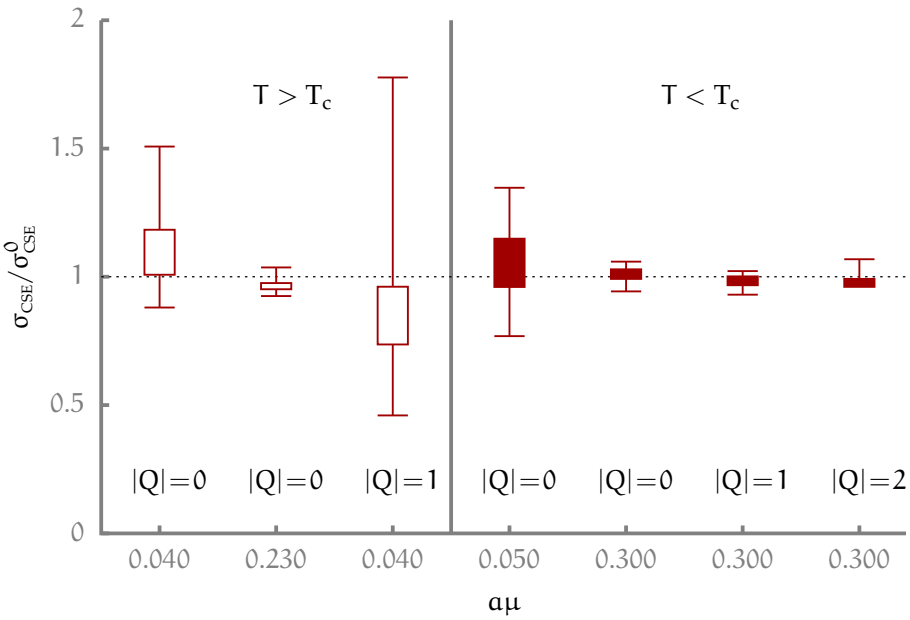

Figure 8.6: Confidence intervals for the ratio $\sigma_{CSE}/\sigma^0_{CSE}$ on larger lattices ($V = 6 \times 18^3$ and $V = 14 \times 14^3$) for different values of the chemical potential μ and the topological charge $|Q|$. Boxes and whiskers mark the confidence interval for a fit with all data points and with the data for largest value of Φ_B excluded, respectively. The open boxes denote the result for $T > T_c$ and the filled boxes for $T < T_c$.

The results for $Q = 0$ on the $V = 8 \times 8^3$ lattice agree very well with the results for the larger lattice and suggest that finite volume effects do not play a large role for the axial current. Nevertheless, it is desirable to perform a cross check of our findings for $|Q| \neq 0$ on the larger lattice. We therefore carried out additional calculations for the $V = 14 \times 14^3$ lattice at $|Q| = 1$ and $|Q| = 2$ for a quark mass $am_q = 0.001$ and a single chemical potential value $a\mu = 0.30$. To better resolve possible non-linearities in the qB dependence of the axial current we used more Φ_B values than for the $Q = 0$ calculations and chose $\Phi_B = 1, 3, 5, 8, 10$. The results of these computations are shown in Figure 8.5. Because of the large numerical costs we calculated only a maximum of 20 stochastic estimators per parameter set. Even though the number of stochastic estimators is relatively small we get a very narrow error band. The reason for this is that we have an additional data point compared to the calculations for $Q = 0$.

On the larger lattice we do not see any corrections to the CSE current for configurations with topological charge $|Q| = 1$ and $|Q| = 2$. The slope of the axial current as a function of qB is consistent with σ^0_{CSE} within the very small statistical errors. In Figure 8.6 we plot the confidence intervals for $\sigma_{CSE}/\sigma^0_{CSE}$ for all our calculations on larger lattices. For all the parameter sets we studied and for both phases of QCD we find, within statistical errors, that the chiral separation conductivity is given by the universal value σ^0_{CSE}.

9

DISCUSSION AND CONCLUSION

In Chapter 7 we developed and tested a numerical method to efficiently compute derivatives of matrix functions of general complex matrices. The method in principle works in combination with any matrix function approximation algorithm. We showed that together with the TSL algorithm our method can be used to compute derivatives of the matrix sign function with high precision.

The efficiency of approximation algorithms for the matrix sign function can often be greatly improved by a so-called deflation. The standard deflation methods only work for diagonalisable matrices. Our method to calculate derivatives makes it necessary to compute the sign function of a non-diagonalisable matrix. To improve the numerical matrix derivative algorithm we therefore developed an generalised deflation method that also works for non-diagonalisable matrices.

In practical calculations it is very important to know the error of an approximation. A big disadvantage of the TSL is that it is in general not possible to obtain an a-priori estimate for the error. We developed a heuristic for tuning the parameters of our method to obtain a given error. The reliability of the error estimates was checked for a large number of random source vectors on gauge configurations with $V = 8 \times 8^3$. In addition we compared the error of the TSL method to the error of a minmax polynomial approximation. We found that our heuristic performs very well and results in a good error estimate.

To test the numerical matrix function derivative in a realistic setting we computed derivatives of the finite-density overlap Dirac operator on different gauge configurations and for several values of the chemical potential μ. The larger the chemical potential the more the kernel operator H differs from a Hermitian matrix. The tests show that our method works very well even for relatively large values of μ of approximately 470 MeV in physical units. The Krylov subspace size necessary to obtain the desired error does not strongly depend on μ.

We compared the performance of the deflated and the undeflated version of the derivative algorithm on all test configurations. On the configurations with $T < T_c$ the spectrum of the operator H in general only has a small gap around the line $\mathrm{Re}(z) = 0$ where the sign function has a discontinuity. For these configurations deflation greatly improves the efficiency of the derivative computation. At $T > T_c$ the situation is different. We find numerically that the spectrum of H on configurations with $T > T_c$ has a comparatively large gap around zero. As expected the deflation has only a minor effect in this case.

The part consuming the most CPU time in the deflated version of the derivative calculation described in Chapter 7 and Appendix E is the inversion of the matrices $A_{\lambda_i} = (\lambda_i - A)$ in Equation (E.4). All this inversions act on the same source vector. It

should therefore be possible to greatly improve the efficiency of the algorithm by using a multi-shift inverter. We tried to use a multi-shift version of the Biconjugate Gradient Stabilized (BiCGSTAB) algorithm for the inversions, but this turned out to be numerically unstable. Finding a stable multi-shift inverter for the matrices A_{λ_i} could further improve the performance of our method.

In physical calculations also higher order derivatives can be of interest. Second order derivatives are for example required to compute current-current and charge-charge correlators, which can be used to compute the electric conductivity or the charge diffusion rate. Generalisations of Theorem 1 to higher order derivatives exist [140]. Thus it is in principle possible to extend our method to calculate higher order derivatives. The calculation of the k-th derivative of a n-dimensional matrix function does, however, require the construction of an upper block triangular matrix of dimension $(k+1)n$. For matrices of this type the deflation procedure becomes very involved. Therefore, deflation is no longer feasible for higher derivatives, which severely limits the usefulness of the method.

The main motivation for the development of described matrix function differentiation method was the computation of conserved currents for the overlap Dirac operator. The conserved currents of a chiral lattice Dirac operator are not renormalised in lattice simulations with massless quarks and are therefore well suited to study anomalous transport phenomena on the lattice.

In Chapter 8 we used the framework of quenched lattice QCD to study the CSE in finite density QCD. It is expected that the CSE is very sensitive to the spontaneous breaking of chiral symmetry in QCD [12]. In the high temperature phase, where the chiral symmetry is restored, no modifications to the transport coefficient σ_{CSE} are anticipated. If chiral symmetry is spontaneously broken, on the other hand, calculations within the linear sigma model predict strong corrections to σ_{CSE}. The goal of our lattice simulations was to test this prediction and to quantify possible corrections to the CSE current. To this end we generated quenched $SU(3)$ gauge configurations for the high temperature and the low temperature phase and computed the conserved axial current of the overlap Dirac operator as a function of the chemical potential and an external magnetic field.

In order to calculate the expectation value of the conserved axial current it is necessary to compute the inverse of the overlap operator. For vanishing quark mass the overlap operator can have exact zero modes and the expectation value of the current becomes ill defined. The index theorem (2.53) relates the zero modes of the overlap operator to the topological charge of the gauge configurations. On the lattice on never encounters the case that there are zero modes of both chiralities for a single configuration and the absolute value of the topological charge is simply given by the number of zero modes. We used this fact to calculate the absolute value of the topological charge for our configurations and considered only configurations with $Q = 0$ for our computations with vanishing quark mass.

We first studied the CSE in the deconfinement phase of QCD for two different values of the chemical potential. The results are depicted in Figure 8.1 and we observe that the axial current depends linearly on the magnetic field strength and on the chemical potential. Our fits for the transport coefficient show that it is consistent with the universal value σ^0_{CSE} for free quarks within statistical errors. The relative errors we obtain for the fit parameter are very small, especially for the larger chemical potential value.

The restriction to gauge configurations with $Q = 0$ introduces a systematic error in our calculations. At vanishing quark mass we can not directly check possible effects of a finite topological charge on the CSE. We therefore introduced a small but finite quark mass to study the axial current on configurations with $|Q| = 1$. For the finite Q calculations we only considered a single chemical potential value and the results are shown in Figure 8.2. We find again a very good agreement between the observed conductivity and σ^0_{CSE}. All in all our calculations for the high temperature phase show that there are no corrections to the CSE in this phase.

We also investigated the CSE in the low temperature phase with broken chiral symmetry. In this phase large deviations of σ_{CSE} from the universal value are expected. For our calculations with massless quarks in the topological sector $Q = 0$ we considered two different chemical potential values. The results are plotted in Figure 8.3. Contrary to the predictions in [12] we do not find any corrections to σ_{CSE} and reproduce the free fermion value σ^0_{CSE} within our small statistical errors. For the best fit at large chemical potential the bootstrap error for the fit parameter is smaller than 6%.

The numerical calculations in the low temperature phase are very expensive and we decided to use a smaller lattice to study the effects of fixed topology on the CSE. For the smaller lattice we could afford to use a larger number of configurations and two different finite quark masses. The data for all our simulations with smaller lattice size are summarised in Figure 8.4. For vanishing topological charge we once more reproduce the free fermion result for the CSE. The data points for different quark masses lie all very close to each other and we do not see any renormalisation of the axial current due to a finite quark mass.

Interestingly, for $|Q| > 0$ we observe large corrections to the CSE current. The axial current is strongly suppressed and no longer a linear function of the external magnetic field. It seems that the corrections are bigger for larger values of $|Q|$. Fits to a second order polynomial suggest that the slope at $a^2 qB = 0$ is still finite, but very small compared to σ^0_{CSE}. To better understand the origin of the corrections to the CSE we calculated the contribution of the topological modes, the eigen modes of D_{ov} that become zero modes in the limit $m_q \to 0$, to the total axial current. After removing the contribution from the topological modes we regain the free fermion result for the CSE. We conclude that the corrections to the CSE at non-zero topological charge are saturated by contribution of topological modes to the total axial current.

The results for $Q = 0$ on the smaller lattice do not show any signs of a finite size effect. It is therefore tempting to assume that also the results for $|Q| > 0$ will hold for larger lattices. To test this assumption we additionally studied the CSE for $|Q| = 1$ and $|Q| = 2$ on the larger lattice. Although we could only afford to use a relative small number of stochastic estimators in these calculations, the errors for the final results are very small. The results are depicted in Figure 8.5. For the larger lattice the axial current for $|Q| > 0$ is again a linear function of the field strength. We recover the universal value σ^0_{CSE} for the slope and find no signs for a correction to the chiral separation conductivity.

A possible explanation for the different results for $|Q| > 0$ for the small and the large lattice is that the configurations for the small lattice correspond to the large instanton limit. It was shown in an analytical calculation that the CSE current identically vanishes in the background of a constant Euclidean self-dual non-Abelian gauge field (see [115, Supplemental Material]). This setup can be understood as the limit of a very large in-

stanton[153]. If the instantons occupy a large ratio of the total volume of the smaller lattice, this would explain the suppression of the CSE current.

The main result of Chapter 8 is the plot in Figure 8.6, where we summarise our final results for the simulations with the large lattices. The plot shows the normalised confidence interval for the transport coefficient σ_{CSE} for both phases of QCD and for all parameter sets we considered. All of the confidence intervals are consistent with the universal value σ^0_{CSE} for the chiral separation conductivity. In particular, for the phase with broken chiral symmetry the statistical errors are very small and for the larger chemical potential value the best relative error is $\lesssim 5\%$.

Taking all our results together we conclude that non-perturbative corrections to the CSE current are absent in quenched lattice QCD. This clearly contradicts the model calculation in [12], which predicts large modifications to the transport coefficient in the phase with broken chiral symmetry. The reason for this discrepancy remains unclear.

One the one hand, it is known from random matrix theory that the chiral condensate vanishes in quenched QCD for any finite chemical potential $\mu > 0$ [154]. This suggests that the pattern of chiral symmetry breaking in our simulations is different than in the linear sigma model. On the other hand, random matrix theory calculations do not take into account finite magnetic fields. An external magnetic field can act as a catalyst for the formation of a chiral condensate [155] or give rise to a different kind of fermionic condensate, the so-called chiral shift parameter. In model calculations it was shown that a finite chiral shift parameter gives corrections to the axial current, see for example [156].

It would be interesting to check if our results hold in unquenched lattice QCD with dynamical overlap fermions. Simulations with dynamical fermions at finite chemical potential are, however, hampered by the sign problem. Our calculations show that it is possible to observe the CSE current already for small values of the chemical potential, albeit with a relatively large statistical error. It might therefore be viable to use reweighting methods to investigate the CSE with dynamical overlap fermions.

As a final remark we emphasise that the high precision we achieved in our calculations of the anomalous transport coefficient σ_{CSE} proves the reliability of our numerical methods. Together with the finite-density overlap Dirac operator described in [40] the numerical tools developed in this thesis lay the foundations to anomalous transport studies with overlap fermions on the lattice.

Part IV

EPILOGUE

10

OUTLOOK

In the final chapter of this thesis we discuss possible future research directions. In Part II we considered an application from solid state physics and investigated the CME in a WSM. We used a model based on the Wilson–Dirac Hamiltonian and performed a mean-field approximation to calculate the static chiral magnetic conductivity.

A potential next step could be to go beyond the mean-field approximation and to study a tight-binding WSM model with Monte-Carlo methods. In general, Monte-Carlo simulations with dynamical fermions suffer from the sign problem. It was shown, however, that the fermion determinant is positive definite in models with a $\mathcal{T}$-symmetric Hamiltonian [157]. Tight-binding models that are are $\mathcal{T}$-symmetric and exhibit a WSM phase were described in [108, 158]. An interesting continuation of the work in this thesis would be to do Monte-Carlo simulations of these WSMs models.

In Part III we developed a numerical differentiation method that makes it possible to compute conserved currents for the finite-density overlap operator. Using this method we studied the CSE in a homogeneous external magnetic field in quenched lattice QCD.

In the existing implementation of the deflated numerical differentiation method for the matrix sign function a large fraction of the total CPU time is spent for the inversion of the matrices A_{λ_i}. All of these inversions act on the same source vector and the development of an multi-shift algorithm for the inversions could vastly improve the efficiency of the differentiation method.

Conserved currents of the overlap operator are not only interesting in the context of anomalous transport calculations, they also have potential applications in hadron structure calculations and in general transport/conductivity studies on the lattice. Moreover, comparing the results for conserved and naive currents is a possible way to determine the value of renormalisation factors.

A conceivable continuation of the work started in this thesis is to investigate the CSE in spatially inhomogeneous external magnetic fields. While this is interesting in itself, it also has an additional advantage: For inhomogeneous magnetic fields the flux and the field strength are not directly related, which allows for a better control of the field strength in lattice simulations.

A more ambitious research project would be to use reweighting techniques to study the CSE with dynamical overlap fermions. Our calculations in Chapter 8 show that CSE current is observable already for small chemical potential values. A reweighting approach could therefore be feasible.

Another interesting research direction is to study the CME with interacting overlap fermions. Previous works either used free overlap fermions [13] or interacting Wilson–Dirac fermions, which explicitly break chiral symmetry and give rise to systematic errors [118, 119]. The introduction of a finite chiral chemical potential for overlap fermions is quite involved but possible [120]. Lattice QCD with finite chiral chemical

potential does not have a sign problem and unquenched calculations are viable. In a first exploratory study one could work with overlap valence quarks and Wilson–Dirac sea quarks to minimise the numerical costs. A comparison with a quenched calculation could give insights into the effects of quenching and be useful for the interpretation of the CSE results, where unquenched calculations are hindered by the sign problem.

On the whole it can be said that the numerical tools developed in this thesis lay the ground to address interesting open questions about the transport properties of strongly interacting chiral fermions.

Part V

APPENDIX

A

CONVENTIONS

A.1 NATURAL UNITS

"For the same reason that we no longer use a certain king's feet to measure distance, we use natural units in which the speed of light c and the Dirac symbol $\hbar$ are both set equal to 1" [20]. Additionally, we also set the Boltzmann constant k_B to 1. Using natural units every dimensionful quantity can be expressed in powers of energy. Owing more to historical reasons than to actual practical considerations the convention in particle physics is to measure energy in units of electron volt (eV).

In lattice gauge theory calculations it is convenient to set the lattice spacing a to 1 and to measure dimensionful quantities in units of a.

A.2 DIRAC MATRICES AND METRIC

Throughout this work the n-dimensional unit matrix is denoted by $\mathbb{1}_n$ and frequently we will leave out the dimension index if the matrix dimension can be inferred unambiguously from the context.

We use the chiral representation of the Dirac gamma matrices γ_i and in terms of the Pauli spin matrices

$$\sigma_1 = \begin{pmatrix} 0 & 1 \\ 1 & 0 \end{pmatrix}, \quad \sigma_2 = \begin{pmatrix} 0 & -i \\ i & 0 \end{pmatrix}, \quad \sigma_3 = \begin{pmatrix} 1 & 0 \\ 0 & -1 \end{pmatrix} \tag{A.1}$$

they read as

$$\gamma_0 = \begin{pmatrix} 0 & \mathbb{1}_2 \\ \mathbb{1}_2 & 0 \end{pmatrix}, \quad \gamma_{1,2,3} = \begin{pmatrix} 0 & \sigma_{1,2,3} \\ -\sigma_{1,2,3} & 0 \end{pmatrix}. \tag{A.2}$$

The matrix $\gamma_5 = i\gamma_0\gamma_1\gamma_2\gamma_3$ anti-commutes with all other gamma matrices and is diagonal in the chiral representation:

$$\gamma_5 = \begin{pmatrix} \mathbb{1}_2 & 0 \\ 0 & -\mathbb{1}_2 \end{pmatrix} \tag{A.3}$$

The anti-commutator of the gamma matrices is given by $\{\gamma_\mu, \gamma_\nu\} = 2g_{\mu\nu}\mathbb{1}$. We use the metric $g_{\mu\nu} = \mathrm{diag}(1, -1, -1, -1)$. In the Hamiltonian formalism it is more common to work with the alpha matrices, which are related to the gamma matrices via $\alpha_k = \gamma_0\gamma_k$. The Euclidean Dirac gamma matrices γ_i^E are defined as

$$\gamma_1^E = -i\gamma_1, \quad \gamma_2^E = -i\gamma_2, \quad \gamma_3^E = -i\gamma_3 \quad \text{and} \quad \gamma_4^E = \gamma_0 \tag{A.4}$$

and $\gamma_5^E = \gamma_1^E\gamma_2^E\gamma_3^E\gamma_4^E = \gamma_5$. The anti-commutator of the Euclidean gamma matrices is given by $\{\gamma_\mu^E, \gamma_\nu^E\} = 2\delta_{\mu\nu}\mathbb{1}$. When there is no risk for a confusion with the Minkowski gamma matrices we will simply drop the index E.

B

FERMI VELOCITY AND WILSON TERM IN THE WSM MODEL

The model (4.4) with the single-particle Hamiltonian (4.5) contains five free parameters. In this work we are interested in general qualitative features of WSMs, hence we do not fix these free parameters and scan over the whole parameter space.

Even for our simple model the computation of the phase diagram and the static chiral magnetic conductivity is numerically very costly. An exhaustive study of the whole parameter space is not feasible and, as we will show in this Appendix, not necessary. It turns out that different values of the Fermi velocity v_F or the Wilson parameter r will not change qualitative results for our model.

DEPENDENCE ON THE FERMI VELOCITY

In the Hamiltonian (4.4) we use a instantaneous on-site interaction as an approximation for the inter-fermion interactions. The simple form of the interaction term gives rise to a non-trivial feature of our model: If we use the rescaled parameter values

$$\widetilde{m}^0 = m^0/v_F, \quad \widetilde{r} = r/v_F, \quad \widetilde{\mu}_A^0 = \mu_A^0/v_F, \quad \widetilde{U} = U/v_F \tag{B.1}$$

and set the Fermi velocity $v_F = 1$ in the Hamiltonian (4.4), this simply amounts to rescaling the original Hamiltonian by $1/v_F$, i.e.:

$$\hat{H}(v_F = 1, \widetilde{m}^0, \widetilde{r}, \widetilde{\mu}_A^0, \widetilde{U}) = \frac{1}{v_F}\hat{H}(v_F, m^0, r, \mu_A^0, U). \tag{B.2}$$

A straightforward calculation shows that the same scaling law holds for the Hubbard–Stratonovich transformation, if we use the rescaled Hubbard–Stratonovich field $\widetilde{\Phi}_x = \Phi_x/v_F$. Consequently the knowledge of the renormalised model parameters $\widetilde{\mu}_A$, $\widetilde{m}_r$ and $\widetilde{m}_i$ immediately gives us the renormalised values for any value of the Fermi velocity:

$$\mu_A = v_F\widetilde{\mu}_A, \quad m_r = v_F\widetilde{m}_r, \quad m_i = v_F\widetilde{m}_i. \tag{B.3}$$

It is obvious that the free energy $\mathcal{F} = -T\ln(\mathrm{tr}\, e^{-\beta\hat{H}})$ inherits the scaling law (B.2) of the Hamiltonian, if we additionally rescale the temperature $\widetilde{T} = T/v_F$:

$$\mathcal{F}(v_F = 1, \widetilde{m}^0, \widetilde{\mu}_A^0, \widetilde{U}, \widetilde{T}) = \frac{1}{v_F}\mathcal{F}(v_F, m^0, \mu_A^0, U, T). \tag{B.4}$$

To calculate the static chiral magnetic conductivity with the Kubo formula (5.3) the second variations of the free energy with respect to the link phases $A_{x,k}$ have to be evaluated. The link phases enter the single-particle Hamiltonian (4.6) via the Peierls

substitution in (4.7). They do not depend on v_F and are not affected if the Fermi velocity is rescaled. Using (B.4) we find

$$\frac{\delta^2 \mathcal{F}(v_F, m^0, \mu_A^0, U, T)}{\delta A_{x,k} \delta A_{y,l}} = v_F \frac{\mathcal{F}(v_F = 1, \widetilde{m}^0, \widetilde{\mu}_A^0, \widetilde{U}, \widetilde{T})}{\delta A_{x,k} \delta A_{y,l}}. \tag{B.5}$$

The coordinates x, y and the wave vector k in the Kubo formula (5.3) do not depend on v_F and are not rescaled. Plugging (B.5) into the Kubo formula yields

$$\sigma_{CME}(k, v_F, m^0, \mu_A^0, U, T) = v_F \sigma_{CME}(k, v_F = 1, \widetilde{m}^0, \widetilde{\mu}_A^0, \widetilde{U}, \widetilde{T}). \tag{B.6}$$

Expanding both sides of (B.6) and using equations (B.3) and (B.1) we find that the derivative of $\sigma_{CME}(k, v_F, m^0, \mu_A^0, U, T)$ with respect to μ_A (or μ_A^0) does not depend on the Fermi velocity. This result is actually to be expected, since the derivative of the chiral magnetic conductivity with respect to μ_A is related to the anomaly coefficient, which does not depend on v_F.

Exploiting the scaling laws (B.2) and (B.4) we can set $v_F = 1$ in all the calculations of Part II. We are then left with only four free parameters. The dependence of our results on the Fermi velocity can be restored in our results using equations (B.3), (B.1) and (B.6)

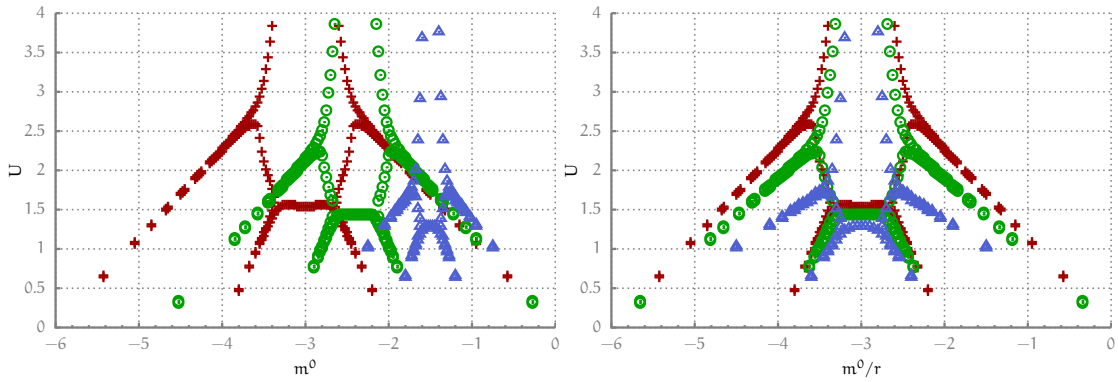

Figure B.1: The phase diagram in the U-m^0–plane for different values of the Wilson parameter r. In the plot on the left hand side the boundary of the Aoki phase is plotted for different values or r. The right hand side shows the same data but with a rescaled bare mass $m^0 \to m^0/r$.

DEPENDENCE ON THE WILSON TERM

The dependence of the Hamiltonian on the Wilson term r is non-trivial. The phase diagram of the model in the U-m^0–plane for $T = 0$, $L_s = 8$, $\mu_A^0 = 0$ and different values of r is depicted on the left hand side of Figure B.1. As r gets smaller and smaller the Aoki phase shrinks and the whole phase diagram is shifted towards the origin. On the right hand side of Figure B.1 we plot the same data for the rescaled bare mass $m^0 \to m^0/r$.

On the one hand, changing the Wilson parameter is obviously not equal to a simple rescaling of the phase diagram. On the other hand, the phase diagrams for different values of r look very similar and have the same main features. While the exact location of the Aoki phase depends on the Wilson term, this phase clearly exists for all (finite) values of r.

We conclude that we can expect qualitatively similar results for different values of r. Thus, in addition to $v_F = 1$, we set $r = 1$ (or rather $r/v_F = \widetilde{r} = 1$) throughout this work. In doing so we have effectively eliminated two free parameters from our model and significantly decreased the numerical costs of our mean-field calculations.

C

DERIVATIVES OF EIGENVECTORS AND EIGENVALUES

In this chapter of the appendix[1] we formally define the notion of the derivative of eigenvectors and summarise some useful results.

Let $A(t)$ be a diagonalisable matrix which depends on an parameter t and has eigenvalues λ_i, left eigenvectors $\langle L_i|$ and right eigenvectors $|R_i\rangle$. For the sake of brevity we assume that A has no degenerate eigenvalues, i.e. $\lambda_i \neq \lambda_j$ if $i \neq j$. For the Wilson-Dirac operator on real lattice QCD configurations, this is usually the case, since configurations with degenerate eigenvalues form a set of measure zero in the space of all gauge field configurations.

If $\left|R_j\right\rangle$ is an eigenvector of A so is $\alpha\left|R_j\right\rangle$ for any $\alpha \in \mathbb{C} \setminus \{0\}$. The direction of an eigenvector is fixed, but its norm and phase are not. In practice a common choice is to fix the eigenvectors by requiring that the left and right eigenvectors are biorthonormal:

$$\left\langle L_i \middle| R_j \right\rangle = \delta_{ij} \tag{C.1}$$

In general, α can be any non-vanishing differentiable function $\alpha(t)$. The freedom in choosing α leads to a freedom in the norm and the direction of the derivative of the eigenvector, since

$$\partial_t \left(\alpha \left|R_j\right\rangle\right) = \alpha\left|\partial_t R_j\right\rangle + (\partial_t \alpha)\left|R_j\right\rangle \tag{C.2}$$

This means the derivative of an eigenvector is fixed only up to a multiplication with a scalar and the addition of any vector from $\operatorname{span}(\left|R_j\right\rangle)$. Therefore, it is necessary to specify which one of all this possible derivatives is used in a certain calculation. Requiring the normalisation (C.1) does not fully fix the derivatives of the eigenvectors. Throughout this thesis we will therefore employ the additional constraint

$$\left\langle L_j \middle| \partial_t R_j \right\rangle = 0 \tag{C.3}$$

so that the derivative of an eigenvector is uniquely defined. It is always possible to choose the eigenvectors such that (C.3) is fulfilled. To see this note that the condition (C.1) does not fix the norm of the vectors $\left|R_j\right\rangle$ and $\left\langle L_j\right|$. Suppose we found vectors that obey (C.1). Then $\left\langle L_j \middle| \partial_t R_j \right\rangle = \xi$, where ξ is a complex number. If we now define $\left|\overline{R_j}\right\rangle := e^{-\xi t}\left|R_j\right\rangle$ and $\left\langle \overline{L_j}\right| := \left\langle L_j\right| e^{\xi t}$ we find that $\left\langle \overline{L_j} \middle| \overline{R_j} \right\rangle = 1$ and $\left\langle \overline{L_j} \middle| \overline{\partial_t R_j} \right\rangle = 0$.

Using the definitions above we will now derive some useful relations. We start with the eigenvalue equation

$$A\left|R_j\right\rangle = \lambda_j \left|R_j\right\rangle . \tag{C.4}$$

1 An earlier version of this chapter appeared in [112].

Taking the derivative on both sides yields

$$(\partial_t A)\left|R_j\right\rangle + A\left|\partial_t R_j\right\rangle = (\partial_t \lambda_j)\left|R_j\right\rangle + \lambda_j\left|\partial_t R_j\right\rangle. \tag{C.5}$$

Multiplying from the left by $\left\langle L_j\right|$ gives the following relation for the derivative of the eigenvalue:

$$\left\langle L_j\right|(\partial_t A)\left|R_j\right\rangle = \partial_t \lambda_j \tag{C.6}$$

To derive a similar result for the derivative of the eigenvectors multiply (C.5) from the left by $\langle L_i|$ for some $i \neq j$. With the normalisation (C.1) this gives

$$\langle L_i|(\partial_t A)\left|R_j\right\rangle + \lambda_i\left\langle L_i\right|\partial_t R_j\right\rangle = \lambda_j\left\langle L_i\right|\partial_t R_j\right\rangle. \tag{C.7}$$

Therefore, the following equation holds for $i \neq j$:

$$\left\langle L_i\right|\partial_t R_j\right\rangle = \frac{\langle L_i|(\partial_t A)\left|R_j\right\rangle}{\lambda_j - \lambda_i} \tag{C.8}$$

Multiplying this equation by $|R_i\rangle$ from the left and summing over $i \neq j$ yields

$$\left|\partial_t R_j\right\rangle = \sum_{i\neq j} \frac{|R_i\rangle\langle L_i|(\partial_t A)\left|R_j\right\rangle}{\lambda_j - \lambda_i}, \tag{C.9}$$

where we used (C.3) and the identity $\sum_{i=1}^{n}|R_i\rangle\langle L_i| = \mathbb{1}$ to make the replacement $\sum_{i\neq j}|R_i\rangle\left\langle L_i\right|\partial_t R_j\right\rangle = \sum_{i=1}^{n}|R_i\rangle\left\langle L_i\right|\partial_t R_j\right\rangle = \left|\partial_t R_j\right\rangle$. Similarly we obtain for the derivative of the left eigenvectors

$$\left\langle\partial_t L_j\right| = \sum_{i\neq j}\frac{\left\langle L_j\right|(\partial_t A)|R_i\rangle\langle L_i|}{\lambda_j - \lambda_i}. \tag{C.10}$$

D

SETUP OF LATTICE CALCULATIONS

D.1 DIRAC OPERATOR

In Section 2.2.1 we have discussed the construction of the Wilson–Dirac operator $D_W(\mu)$. For lattice QCD with a single quark flavour at finite quark chemical potential μ and in the presence of a background $U(1)$ gauge field the Wilson–Dirac operator is given by

$$D_W(\mu) = \mathbb{1} - \kappa \sum_{i=1}^{3} \left(G_i^+ + G_i^- \right) - \kappa \left(e^{\mu} G_4^+ + e^{-\mu} G_4^- \right), \tag{D.1}$$

with

$$(G_\nu^\pm)_{x,y} := (1 \pm \gamma_\nu) U_{\pm\nu}(x) e^{i\Theta_{\pm\nu}(x)} \delta_{x\pm\hat{\nu},y}. \tag{D.2}$$

The $U_{\pm\nu}(x) \in SU(3)$ are (dynamical) lattice gauge fields and the factors $e^{i\Theta_{\pm\nu}(x)} \in U(1)$ describe the (background) lattice gauge fields corresponding to the external Abelian gauge field $\Theta_\nu(x)$. The lattice spacing a and the Wilson parameter r are set to one and the hopping parameter is defined as $\kappa := 1/(2m_W + 8)$, where $m_W \in (0, 2)$ is the Wilson mass term.

The derivative of the Wilson–Dirac operator with respect to the Abelian gauge field $\Theta_\nu(x)$ can be computed analytically and reads as

$$\left(\frac{\partial D_W}{\partial \Theta_\nu(z)} \right)_{x,y} = -i\kappa \left((G_\nu^+)_{x,y}\, \delta_{x,z} - (G_\nu^-)_{x,y}\, \delta_{x-\hat{\nu},z} \right). \tag{D.3}$$

D.2 LATTICE PARAMETERS

For the quenched lattice simulations in Part III we use the tadpole-improved [159–162] Lüscher–Weisz gauge action [163]. An improved gauge action suppresses the UV fluctuations of the gauge field and has a positive effect on the numerical properties of the lattice Dirac operator. The tadpole-improved Lüscher–Weisz action has one free parameter, the inverse gauge coupling β, and two additional parameters that have to be fixed self-consistently. We take these parameters from [164], where they were computed with high precision.

All together we used three different sets of lattice parameters, which are summarised in the upper part of Table D.1. The lattice volume is given by $V = L_T \times L_S^3$, where L_T and L_S stand for the temporal and spacial extend of the lattice.

The deconfinement transition temperature T_c for the Lüscher–Weisz action is $T_c \approx 300$ MeV [145]. The setup with $V = 6 \times 18^3$ and $\beta = 8.45$ corresponds to a temperature

$T > T_c$. The simulations with $V = 14 \times 14^4$ and $V = 8 \times 8^4$ at $\beta = 8.1$ both have a temperature $T < T_c$.

To set the scale we use results from [164], where the lattice spacing was determined using the Sommer parameter [165]. The physical values of the lattice parameters are summarised in Table D.1.

Setup	β	8.1	8.1	8.45
	Volume	14×14^3	8×8^3	6×18^3
	Lattice	Phys. Value		
a [fm]	1	0.125	0.125	0.095
L_S^3 [fm^3]	L_S^3	5.4	1.0	5.0
T [MeV]	L_T^{-1}	113	197	346
μ [MeV]	0.050	79	–	–
	0.100	–	158	–
	0.300	474	–	–
	0.040	–	–	83
	0.230	–	–	478
$\frac{qB}{\Phi_B}$ [MeV]^2	$\frac{2\pi}{a^2 L_S^2}$	283^2	495^2	289^2

Table D.1: Simulation parameters

E

EFFICIENT DEFLATION OF DERIVATIVES OF THE SIGN FUNCTION

In the following we present an efficient numerical algorithm for the deflation of derivatives of the sign function[1]. Considering Equation (7.20) it is tempting to exploit the sparsity of $(0, |x\rangle)^T$ to simplify the deflation calculations. However, it turns out that it is necessary to define the deflation for general source vectors $|\Phi\rangle := (|x_1\rangle, |x_2\rangle)^T$. The reason is that the most convenient way to estimate the error of the TSL approximation is via Equation (7.52), where the TSL approximation is applied twice and the deviation from unity of the final result is measured. Even if the source vector is sparse, the resulting vector after the first TSL approximation will in general not be. Consequently, we need a deflation method that works with general input vectors. From Equation (7.51) we then get

$$\begin{aligned} \operatorname{sgn}(\mathcal{B}) \begin{pmatrix} |x_1\rangle \\ |x_2\rangle \end{pmatrix} &= \underbrace{\sum_{i=1}^{k} s_i \left\{ \begin{pmatrix} |R_i\rangle \\ 0 \end{pmatrix} [\langle L_i | x_1\rangle + \langle \partial_t L_i | x_2\rangle] + \begin{pmatrix} |\partial_t R_i\rangle \\ |R_i\rangle \end{pmatrix} \langle L_i | x_2\rangle \right\}}_{\text{I}} \\ &\quad \underbrace{+ \operatorname{sgn}(\mathcal{B}) \bar{\mathcal{P}}_{2k} \begin{pmatrix} |x_1\rangle \\ |x_2\rangle \end{pmatrix}}_{\text{II}}, \end{aligned} \tag{E.1}$$

where we used the fact that $\partial_t \operatorname{sgn}(\lambda_i) = 0$ since the sign function is piecewise constant and introduced the notation $s_i := \operatorname{sgn}(\lambda_i)$. Let us now investigate part I of (E.1).

$$\text{I} = \sum_{i=1}^{k} s_i \left\{ \begin{pmatrix} |R_i\rangle \\ 0 \end{pmatrix} \underbrace{[\langle L_i | x_1\rangle + \langle \partial_t L_i | x_2\rangle]}_{c_{1i}} + \begin{pmatrix} |\partial_t R_i\rangle \\ |R_i\rangle \end{pmatrix} \underbrace{\langle L_i | x_2\rangle}_{c_{2i}} \right\} \tag{E.2}$$

In a practical calculation we are interested in finding an efficient way to compute the coefficients c_{1i} and c_{2i}. Note that these coefficients are proportional to the scalar products of $|\Phi\rangle$ with the odd and even rows of the matrix $\mathcal{X}^{-1}$ respectively. The same coefficients appear in the projection $\bar{\mathcal{P}}_{2k} |\Phi\rangle$, which is needed to compute part II. Apart from c_{1i} and c_{2i} the only non-trivial part of the deflation is the computation of $|\partial_t R_i\rangle$. As we mentioned earlier, the left and right eigenvectors $\langle L_i|$ and $|R_i\rangle$ can be computed with ARPACK routines.

The coefficients c_{2i} are simply scalar products. As we will see later on, they appear in several parts of the deflation and therefore it pays off to pre-compute and save them.

1 This chapter also appeared in [112].

The first part of the coefficients c_{1i} is again a scalar product. The computation of the second part is more involved. First we use Equation (C.10) to get rid of the derivative of the eigenvector:

$$\langle \partial_t L_i | x_1 \rangle = \sum_{j \neq i} \frac{\langle L_i | (\partial_t A) | R_j \rangle \langle L_j | x_2 \rangle}{\lambda_i - \lambda_j} \tag{E.3}$$

Computing all the eigenvectors of A is in general way too expensive and only the first k eigenvectors are known explicitly. The trick now is to use the identity $\sum_{j=k+1}^{n} \frac{|R_j\rangle\langle L_j|x_2\rangle}{\lambda_i - \lambda_j} \equiv (\lambda_i - A)^{-1} P_k |x_2\rangle$, where $P_k := \sum_{i=k+1}^{n} |R_i\rangle \langle L_i|$. Note that the inverse of $(\lambda_i - A)$ is well defined for $P_k |x_2\rangle$ and we can write

$$\langle \partial_t L_i | x_1 \rangle = \sum_{\substack{j=1 \\ j \neq i}}^{k} \frac{\langle L_i | (\partial_t A) | R_j \rangle c_{2j}}{\lambda_i - \lambda_j} + \langle L_i | (\partial_t A) (\lambda_i - A)^{-1} P_k | x_2 \rangle \tag{E.4}$$

In practical applications the matrix $A_{\lambda_i} := (\lambda_i - A)$ is sparse and its inverse can be computed very efficiently with iterative methods. Since the vector $P_k |x_2\rangle$ in Equation (E.4) is the same for all λ_i with $i \in \{1, \ldots, k\}$ it is in principle possible to use a multi-shift inversion algorithm to compute the inversions. In practice, however, we found that the numerical inversion with the (multi-shift) BiCGSTAB algorithm was unstable. To avoid stability issues we used the CG algorithm to find the inverse of the Hermitian matrix $A_{\lambda_i} A_{\lambda_i}^{\dagger}$, from which it is straightforward to compute the inverse of A_{λ_i}.

The vector $|R_i\rangle$ lies in the kernel of the matrix A_{λ_i}. For this reason and because of numerical errors the vector $A_{\lambda_i}^{-1} P_k |x_2\rangle$ can have non-zero components in $|R_i\rangle$ direction. Remember that we normalised the derivative of the eigenvectors such that $\langle \partial_t L_i | R_i \rangle = 0$. In order to enforce this normalisation in a numerical calculation we have to project out the spurious $|R_i\rangle$ component. To this end we define the projection operator Q_i in the following way

$$Q_i |\psi\rangle := |\psi\rangle - |R_i\rangle \langle L_i | \psi \rangle . \tag{E.5}$$

With this operator we can now write down the final equation for $\langle \partial_t L_i | x_1 \rangle$ that can be used in numerical calculations

$$\langle \partial_t L_i | x_1 \rangle = \langle L_i | (\partial_t A) \left(\sum_{\substack{j=1 \\ j \neq i}}^{k} \frac{|R_j\rangle c_{2j}}{\lambda_i - \lambda_j} + Q_i (\lambda_i - A)^{-1} P_k | x_2 \rangle \right) . \tag{E.6}$$

Analogously one can use Equation (C.9) to derive the following formula for the derivative of the right eigenvectors

$$|\partial_t R_i\rangle = \sum_{\substack{j=1 \\ j \neq i}}^{k} \frac{|R_j\rangle \langle L_j | (\partial_t A) | R_i \rangle}{\lambda_i - \lambda_j} + Q_i (\lambda_i - A)^{-1} P_k (\partial_t A) | R_i \rangle . \tag{E.7}$$

We now have all the parts needed for an efficient computation of the deflation and an implementation in pseudo-code is given in Listing F.3.

F

CODE LISTINGS

1: **function** LANCZOS(A,$|x\rangle$,k,f)
2: $|v_1\rangle \leftarrow |x\rangle / \|x\|$
3: $|w_1\rangle \leftarrow |x\rangle / \|x\|$
4: **for** $i \leftarrow 1$ **to** $k-1$ **do**
5: $T_{ii} \leftarrow \langle w_i| A |v_i\rangle$
6:
7: $|v_{i+1}\rangle \leftarrow (A - T_{ii}) |v_i\rangle$
8: $|w_{i+1}\rangle \leftarrow (A^\dagger - T^*_{ii}) |w_i\rangle$
9:
10: **if** $i > 1$ **then**
11: $|v_{i+1}\rangle \leftarrow |v_{i+1}\rangle - T_{(i-1)i} |v_{i-1}\rangle$
12: $|w_{i+1}\rangle \leftarrow |w_{i+1}\rangle - T^*_{i(i-1)} |w_{i-1}\rangle$
13: **end if**
14:
15: **if** $\langle w_{i+1}| v_{i+1}\rangle = 0$ **then**
16: **if** $|w_{i+1}\rangle = 0$ or $|v_{i+1}\rangle = 0$ **then**
17: invariant subspace found
18: $k \leftarrow i$
19: **else**
20: serious breakdown
21: **end if**
22: **end if**
23:
24: $T_{(i+1)i} \leftarrow \| |v_{i+1}\rangle \|$
25: $T_{i(i+1)} \leftarrow \langle w_{i+1}| v_{i+1}\rangle$
26: $T_{i(i+1)} \leftarrow T_{i(i+1)} / T_{(i+1)i}$
27: $|v_{i+1}\rangle \leftarrow |v_{i+1}\rangle / T_{(i+1)i}$
28: $|w_{i+1}\rangle \leftarrow |w_{i+1}\rangle / T^*_{i(i+1)}$
29: **end for**
30: $T_{kk} \leftarrow \langle w_k| A |v_k\rangle$
31:
32: **return** $\|x\| Vf(T) |e_1\rangle$
33: **end function**

Listing F.1: An implementation of the Lanczos algorithm in pseudocode. The algorithm can end prematurely if an invariant subspace of A (or $A^\dagger$) is found or if a serious breakdown occurs. The first case can be taken care of, but a serious breakdown can not be fixed.

function LANCZOSAD(A,$\partial_t A$,$|x\rangle$,k,f,∂_tf)
  $|v_1\rangle \leftarrow |x\rangle / \|x\|$ $\quad$ $|\partial_t v_1\rangle \leftarrow 0$
  $|w_1\rangle \leftarrow |x\rangle / \|x\|$ $\quad$ $|\partial_t w_1\rangle \leftarrow 0$

  for $i \leftarrow 1$ **to** $k-1$ **do**
    $T_{ii} \leftarrow \langle w_i| A |v_i\rangle$ $\quad$ $\partial_t T_{ii} \leftarrow \langle \partial_t w_i| A |v_i\rangle + \langle w_i| (\partial_t A) |v_i\rangle + \langle w_i| A |\partial_t v_i\rangle$

    $|v_{i+1}\rangle \leftarrow (A - T_{ii}) |v_i\rangle$ $\quad$ $|\partial_t v_{i+1}\rangle \leftarrow (\partial_t A - \partial_t T_{ii}) |v_i\rangle + (A - T_{ii}) |\partial_t v_i\rangle$
    $|w_{i+1}\rangle \leftarrow (A^\dagger - T^*_{ii}) |w_i\rangle$ $\quad$ $|\partial_t w_{i+1}\rangle \leftarrow (\partial_t A^\dagger - \partial_t T^*_{ii}) |w_i\rangle + (A^\dagger - T^*_{ii}) \partial_t |w_i\rangle$

    if $i > 1$ **then**
      $|v_{i+1}\rangle \leftarrow |v_{i+1}\rangle - T_{(i-1)i} |v_{i-1}\rangle$
      $|\partial_t v_{i+1}\rangle \leftarrow |\partial_t v_{i+1}\rangle - \{(\partial_t T_{(i-1)i}) |v_{i-1}\rangle + T_{(i-1)i} |\partial_t v_{i-1}\rangle\}$
      $|w_{i+1}\rangle \leftarrow |w_{i+1}\rangle - T^*_{i(i-1)} |w_{i-1}\rangle$
      $|\partial_t w_{i+1}\rangle \leftarrow |\partial_t w_{i+1}\rangle - \{(\partial_t T^*_{i(i-1)}) |w_{i-1}\rangle + T^*_{i(i-1)} |\partial_t w_{i-1}\rangle\}$
    end if

    $T_{(i+1)i} \leftarrow \| |v_{i+1}\rangle \|$ $\quad$ $\partial_t T_{(i+1)i} \leftarrow \mathrm{Re}(\langle v_{i+1}| \partial_t v_{i+1}\rangle) / \| |v_{i+1}\rangle \|$
    $T_{i(i+1)} \leftarrow \langle w_{i+1}| v_{i+1}\rangle$ $\quad$ $\partial_t T_{i(i+1)} \leftarrow \langle \partial_t w_{i+1}| v_{i+1}\rangle + \langle w_{i+1}| \partial_t v_{i+1}\rangle$

    $T_{i(i+1)} \leftarrow T_{i(i+1)} / T_{(i+1)i}$
    $\partial_t T_{i(i+1)} \leftarrow (\partial_t T_{i(i+1)}) / T_{(i+1)i} - (T_{i(i+1)} \partial_t T_{(i+1)i}) / T^2_{(i+1)i}$
    $|v_{i+1}\rangle \leftarrow |v_{i+1}\rangle / T_{(i+1)i}$
    $|\partial_t v_{i+1}\rangle \leftarrow |\partial_t v_{i+1}\rangle / T_{(i+1)i} - (|v_{i+1}\rangle \partial_t T_{(i+1)i}) / T^2_{(i+1)i}$
    $|w_{i+1}\rangle \leftarrow |w_{i+1}\rangle / T^*_{i(i+1)}$
    $|\partial_t w_{i+1}\rangle \leftarrow |\partial_t w_{i+1}\rangle / T^*_{i(i+1)} - (|w_{i+1}\rangle \partial_t T^*_{i(i+1)}) / T^{*2}_{i(i+1)}$
  end for

  $T_{kk} \leftarrow \langle w_k| A |v_k\rangle$ $\quad$ $\partial_t T_{kk} \leftarrow \langle \partial_t w_k| A |v_k\rangle + \langle w_k| (\partial_t A) |v_k\rangle + \langle w_k| A |\partial_t v_k\rangle$

  return $\|x\| \Big((\partial_t V) f(T) |e_1\rangle + V(\partial_t f(T)) |e_1\rangle + V f(T) (\partial_t W) |x\rangle \Big)$
end function

Listing F.2: Algorithmic differentiation for the TSL. The original parts of the algorithm are set in grey and the algorithmic differentiation steps in black. Note that in a practical calculation the algorithmic differentiation would be performed automatically and not put in the code by hand.

1: **function** DEFLATEDSIGNDERIVATIVE
2: // Compute $|out\rangle = (|out_1\rangle, |out_2\rangle)^T = sgn(\mathcal{B})(|x_1\rangle, |x_2\rangle)^T$
3: // with deflation
4:
5: **for** $i \leftarrow 1$ **to** k **do** // Compute $|\partial_t R_i\rangle$
6: $|\partial_t R_i\rangle = |0\rangle$
7: **for** $j \leftarrow 1$ **to** k **do**
8: **if** $i \neq j$ **then**
9: $|\partial_t R_i\rangle = |\partial_t R_i\rangle + \frac{|R_j\rangle\langle L_j|(\partial_t A)|R_i\rangle}{\lambda_i - \lambda_j}$
10: **end if**
11: **end for**
12: $|\partial_t R_i\rangle = |\partial_t R_i\rangle + Q_i (\lambda_i - A)^{-1} P_k(\partial_t A) |R_i\rangle$
13: **end for**
14:
15: **for** $i \leftarrow 1$ **to** k **do** // Compute c_{2i}
16: $c_2[i] = \langle L_i | x_2 \rangle$
17: **end for**
18:
19: // Compute c_{1i}, the exact part and the projection of $|x\rangle$
20: $|x_k\rangle = P_k |x_2\rangle$
21: $|out_1\rangle = |0\rangle$
22: $|out_2\rangle = |0\rangle$
23: **for** $i \leftarrow 1$ **to** k **do**
24: $|v\rangle = Q_i (\lambda_i - A)^{-1} |x_k\rangle$
25: **for** $j \leftarrow 1$ **to** k **do**
26: **if** $i \neq j$ **then**
27: $|v\rangle = |v\rangle + \frac{c_2[j]|R_j\rangle}{\lambda_i - \lambda_j}$
28: **end if**
29: **end for**
30: $c_1[i] = \langle L_i | ((\partial_t A) |v\rangle + |x_1\rangle)$
31: // Exact part of output
32: $s_i = sgn(\lambda_i)$
33: $|out_1\rangle = |out_1\rangle + s_i (c_1[i] |R_i\rangle + c_2[i] |\partial_t R_i\rangle)$
34: $|out_2\rangle = |out_2\rangle + s_i (c_2[i] |R_i\rangle)$
35: // Projection of input vector
36: $|x_1\rangle = |x_1\rangle - (c_1[i] |R_i\rangle + c_2[i] |\partial_t R_i\rangle)$
37: $|x_2\rangle = |x_2\rangle - (c_2[i] |R_i\rangle)$
38: **end for**
39: // Exact part plus TSL approximation of projected part
40: $|out\rangle = (|out_1\rangle, |out_2\rangle)^T + TSL(\mathcal{B}, (|x_1\rangle, |x_2\rangle)^T)$
41: **return** $|out\rangle$
42: **end function**

Listing F.3: Deflated version of the derivative computation using the Lanczos algorithm.

BIBLIOGRAPHY

[1] D. Kharzeev and A. Zhitnitsky. 'Charge separation induced by $\mathcal{P}$-odd bubbles in QCD matter'. *Nucl. Phys. A* 797 (2007), pp. 67–79. arXiv: 0706.1026.

[2] D. E. Kharzeev, L. D. McLerran and H. J. Warringa. 'The effects of topological charge change in heavy ion collisions: "Event by event P and CP violation"'. *Nucl. Phys. A* 803 (2007), pp. 227–253. arXiv: 0711.0950v1.

[3] L. Adamczyk et al. 'Beam-energy dependence of charge separation along the magnetic field in Au+Au collisions at RHIC'. *Phys. Rev. Lett.* 113, 052302 (2014). arXiv: 1404.1433v2.

[4] G. Başar, D. E. Kharzeev and H.-U. Yee. 'Triangle anomaly in Weyl semi-metals'. *Phys. Rev. B* 89, 035142 (2013). arXiv: 1305.6338.

[5] H.-J. Kim et al. 'Dirac vs. Weyl in topological insulators: Adler-Bell-Jackiw anomaly in transport phenomena'. *Phys. Rev. Lett.* 111, 246603 (2013). arXiv: 1307.6990v1.

[6] Q. Li et al. 'Chiral magnetic effect in ZrTe5'. *Nat. Phys.* 12 (2014), pp. 550–554. arXiv: 1412.6543v1.

[7] A. Vilenkin. 'Equilibrium parity-violating current in a magnetic field'. *Phys. Rev. D* 22 (1980), pp. 3080–3084. DOI: 10.1103/physrevd.22.3080.

[8] D. T. Son and A. R. Zhitnitsky. 'Quantum Anomalies in Dense Matter'. *Phys. Rev. D* 70, 074018 (2004). arXiv: hep-ph/0405216.

[9] M. A. Metlitski and A. R. Zhitnitsky. 'Anomalous Axion Interactions and Topological Currents in Dense Matter'. *Phys.Rev. D* 72, 045011 (2005). arXiv: hep-ph/0505072.

[10] H. Tashiro, T. Vachaspati and A. Vilenkin. 'Chiral Effects and Cosmic Magnetic Fields'. *Phys. Rev. D* 86, 105033 (2012). arXiv: 1206.5549v1.

[11] G. Sigl and N. Leite. 'Chiral Magnetic Effect in Protoneutron Stars and Magnetic Field Spectral Evolution'. *J. Cosmol. Astropart. Phys.* 2016 (2016), pp. 025–025. arXiv: 1507.04983v2.

[12] G. M. Newman and D. T. Son. 'Response of strongly interacting matter to a magnetic field: Some exact results'. *Phys. Rev. D* 73, 045006 (2005). arXiv: hep-ph/0510049.

[13] P. V. Buividovich. 'Anomalous transport with overlap fermions'. *Nucl. Phys. A* 925 (2014), pp. 218–253. arXiv: 1312.1843.

[14] P. V. Buividovich. 'Spontaneous chiral symmetry breaking and the Chiral Magnetic Effect for interacting Dirac fermions with chiral imbalance'. *Phys. Rev. D* 90, 125025 (2014). arXiv: 1408.4573v2.

[15] E. V. Gorbar et al. 'Radiative corrections to chiral separation effect in QED'. *Phys. Rev. D* 88, 025025 (2013). arXiv: 1304.4606.

[16] K. Jensen, P. Kovtun and A. Ritz. 'Chiral conductivities and effective field theory'. *JHEP* 2013, 186 (2013). arXiv: 1307.3234v1.

[17] U. Gursoy and A. Jansen. '(Non)renormalization of Anomalous Conductivities and Holography'. *JHEP* 2014, 092 (2014). arXiv: 1407.3282v2.

[18] M. E. Peskin and D. V. Schroeder. *An Introduction to Quantum Field Theory*. The Perseus Books Group, 1995.

[19] M. Srednicki. *Quantum Field Theory*. Cambridge University Press, 2007.

[20] A. Zee. *Quantum Field Theory in a Nutshell*. Princeton Univers. Press, 2010.

[21] I. Montvay and G. Münster. *Quantum Fields on a Lattice*. Cambridge University Press, 1997.

[22] C. Gattringer and C. B. Lang. *Quantum Chromodynamics on the Lattice. An Introductory Presentation*. Springer Berlin Heidelberg, 2010.

[23] C. Gattringer and K. Langfeld. 'Approaches to the sign problem in lattice field theory'. *Int. J. Mod. Phys. A* 31, 1643007 (2016). arXiv: 1603.09517v1.

[24] P. Hasenfratz and F. Karsch. 'Chemical potential on the lattice'. *Phys. Lett. B* 125 (1983), pp. 308–310. DOI: 10.1016/0370-2693(83)91290-x.

[25] N. Bilić and R. V. Gavai. 'On the thermodynamics of an ideal fermi gas on the lattice at finite density'. *Z. Phys. C* 23 (1984), pp. 77–83. DOI: 10.1007/bf01558043.

[26] J. Kogut et al. 'Chiral symmetry restoration in baryon rich environments'. *Nucl. Phys. B* 225 (1983), pp. 93–122. DOI: 10.1016/0550-3213(83)90014-7.

[27] H. B. Nielsen and M. Ninomiya. 'A no-go theorem for regularizing chiral fermions'. *Phys. Lett. B* 105 (1981), pp. 219–223. DOI: 10.1016/0370-2693(81)91026-1.

[28] H. Nielsen and M. Ninomiya. 'Absence of neutrinos on a lattice'. *Nucl. Phys. B* 185 (1981), pp. 20–40. DOI: 10.1016/0550-3213(81)90361-8.

[29] H. Nielsen and M. Ninomiya. 'Absence of neutrinos on a lattice'. *Nucl. Phys. B* 193 (1981), pp. 173–194. DOI: 10.1016/0550-3213(81)90524-1.

[30] D. Friedan. 'A proof of the Nielsen-Ninomiya theorem'. *Commun. Math. Phys.* 85 (1982), pp. 481–490. DOI: 10.1007/bf01403500.

[31] F. Wilczek. 'Lattice Fermions'. *Phys. Rev. Lett.* 59 (1987), pp. 2397–2400. DOI: 10.1103/PhysRevLett.59.2397.

[32] P. H. Ginsparg and K. G. Wilson. 'A remnant of chiral symmetry on the lattice'. *Phys. Rev. D* 25 (10 1982), pp. 2649–2657. DOI: 10.1103/PhysRevD.25.2649.

[33] M. Lüscher. 'Exact chiral symmetry on the lattice and the Ginsparg-Wilson relation'. *Phys. Lett. B* 428 (1998), pp. 342–345. arXiv: hep-lat/9802011.

[34] P. Hasenfratz, V. Laliena and F. Niedermayer. 'The index theorem in QCD with a finite cut-off'. *Phys. Lett. B* 427 (1998), pp. 125–131. arXiv: hep-lat/9801021.

[35] K. Fujikawa. 'A continuum limit of the chiral Jacobian in lattice gauge theory'. *Nucl. Phys. B* 546 (1998), pp. 480–494. arXiv: hep-th/9811235.

[36] Y. Kikukawa and A. Yamada. 'Weak coupling expansion of massless QCD with a Ginsparg-Wilson fermion and axial U(1) anomaly'. *Phys. Lett. B* 448 (1998), pp. 265–274. arXiv: hep-lat/9806013.

[37] D. H. Adams. 'Axial anomaly and topological charge in lattice gauge theory with Overlap Dirac operator'. *Ann. Phys.* 296 (1998), pp. 131–151. arXiv: hep-lat/9812003v6.

[38] H. Neuberger. 'Exactly massless quarks on the lattice'. *Phys. Lett. B* 417 (1998), pp. 141–144. arXiv: hep-lat/9707022v3.

[39] H. Neuberger. 'More about exactly massless quarks on the lattice'. *Phys. Lett. B* 427 (1998), pp. 353–355. arXiv: hep-lat/9801031v1.

[40] J. Bloch and T. Wettig. 'Overlap Dirac Operator at Nonzero Chemical Potential and Random Matrix Theory'. *Phys. Rev. Lett.* 97, 012003 (2006). arXiv: hep-lat/0604020.

[41] K. Fukushima, D. E. Kharzeev and H. J. Warringa. 'Chiral magnetic effect'. *Phys. Rev. D* 78 (2008). arXiv: 0808.3382.

[42] D. E. Kharzeev. 'The Chiral Magnetic Effect and Anomaly-Induced Transport'. *Prog. Part. Nucl. Phys.* 75 (2013), pp. 133–151. arXiv: 1312.3348.

[43] D. E. Kharzeev et al. 'Chiral Magnetic and Vortical Effects in High-Energy Nuclear Collisions — A Status Report'. *Prog. Part. Nucl. Phys.* 88 (2015), pp. 1–28. arXiv: 1511.04050.

[44] S. L. Adler. 'Axial-Vector Vertex in Spinor Electrodynamics'. *Phys. Rev.* 177 (1969), pp. 2426–2438. DOI: 10.1103/physrev.177.2426.

[45] J. S. Bell and R. Jackiw. 'A PCAC puzzle: $\pi^0 \to \gamma\gamma$ in the σ-model'. *Il Nuovo Cimento A* 60 (1969), pp. 47–61. DOI: 10.1007/bf02823296.

[46] K. Fujikawa. 'Path integral for gauge theories with fermions'. *Phys. Rev. D* 21.10 (May 1980), pp. 2848–2858. DOI: 10.1103/physrevd.21.2848; K. Fujikawa. 'Erratum'. *Phys. Rev. D* 22.6 (Sept. 1980), pp. 1499–1499. DOI: 10.1103/physrevd.22.1499.

[47] S. L. Adler and W. A. Bardeen. 'Absence of Higher-Order Corrections in the Anomalous Axial-Vector Divergence Equation'. *Phys. Rev.* 182 (1969), pp. 1517–1536. DOI: 10.1103/physrev.182.1517.

[48] D. E. Kharzeev and H.-U. Yee. 'Anomalies and time reversal invariance in relativistic hydrodynamics: the second order and higher dimensional formulations'. *Phys. Rev. D* 84 (2011). arXiv: 1105.6360v1.

[49] D. T. Son and P. Surowka. 'Hydrodynamics with Triangle Anomalies'. *Phys. Rev. Lett.* 103, 191601 (2009). arXiv: 0906.5044.

[50] A. V. Sadofyev and M. V. Isachenkov. 'The chiral magnetic effect in hydrodynamical approach'. *Phys. Lett. B* 697 (2010), pp. 404–406. arXiv: 1010.1550.

[51] N. Banerjee et al. 'Constraints on Fluid Dynamics from Equilibrium Partition Functions'. *JHEP* 2012, 046 (2012). arXiv: 1203.3544.

[52] P. V. Buividovich and M. Puhr. 'A lattice mean-field study of the phase diagram of interacting parity-breaking Weyl semimetals'. *PoS(LATTICE2014)061* (2014). arXiv: 1410.6704.

[53] P. V. Buividovich, M. Puhr and S. N. Valgushev. 'Chiral magnetic conductivity in an interacting lattice model of parity-breaking Weyl semimetal'. *Phys. Rev. B* 92, 205122 (2015). arXiv: 1505.04582.

[54] S. N. Valgushev, M. Puhr and P. V. Buividovich. 'Chiral Magnetic Effect in finite-size samples of parity-breaking Weyl semimetals'. *PoS(LATTICE2015)043* (2015). arXiv: 1512.01405v2.

[55] A. Bansil, H. Lin and T. Das. 'Colloquium: Topological Band Theory'. *Rev. Mod. Phys.* 88, 021004 (2016). arXiv: 1603.03576v1.

[56] T. O. Wehling, A. M. Black-Schaffer and A. V. Balatsky. 'Dirac materials'. *Adv. Phys.* 63 (2014), pp. 1–76. arXiv: 1405.5774v1.

[57] X. Wan et al. 'Topological semimetal and Fermi-arc surface states in the electronic structure of pyrochlore iridates'. *Phys. Rev. B* 83, 205101 (2010). arXiv: 1007.0016.

[58] M. M. Vazifeh and M. Franz. 'Electromagnetic Response of Weyl Semimetals'. *Phys. Rev. Lett.* 111, 027201 (2013). arXiv: 1303.5784.

[59] S.-Y. Xu et al. 'Discovery of a Weyl Fermion semimetal state in NbAs'. *Nature Physics* 11 (2015), pp. 748–754. arXiv: 1504.01350v2.

[60] J. Xiong et al. 'Signature of the chiral anomaly in a Dirac semimetal: a current plume steered by a magnetic field' (2015). arXiv: 1503.08179.

[61] C.-L. Zhang et al. 'Signatures of the Adler–Bell–Jackiw chiral anomaly in a Weyl fermion semimetal'. *Nat. Commun.* 7, 10735 (2016). arXiv: 1601.04208.

[62] Y. Wu et al. 'Observation of Fermi Arcs in Type-II Weyl Semimetal Candidate WTe2'. *Phys. Rev. B* 94, 121113 (2016). arXiv: 1604.05176v1.

[63] H. B. Nielsen and M. Ninomiya. 'The Adler-Bell-Jackiw anomaly and Weyl fermions in a crystal'. *Phys. Lett. B* B130 (1983), pp. 389–396. DOI: 10.1016/0370-2693(83)91529-0.

[64] P. V. Buividovich et al. 'Magnetic-Field-Induced insulator-conductor transition in SU(2) quenched lattice gauge theory'. *Phys. Rev. Lett.* 105, 132001 (2010). arXiv: 1003.2180.

[65] K. Landsteiner, Y. Liu and Y.-W. Sun. 'Negative magnetoresistivity in chiral fluids and holography'. *JHEP* 2015, 127 (2014). arXiv: 1410.6399v3.

[66] A. Jimenez-Alba et al. 'Anomalous magnetoconductivity and relaxation times in holography'. *JHEP* 2015, 117 (2015). arXiv: 1504.06566.

[67] K. Landsteiner. 'Anomaly related transport of Weyl fermions for Weyl semimetals'. *Phys. Rev. B* 89, 075124 (2013). arXiv: 1306.4932v3.

[68] P. Goswami and S. Tewari. 'Axionic field theory of (3+1)-dimensional Weyl semimetals'. *Phys. Rev. B* 88, 245107 (2012). arXiv: 1210.6352.

[69] P. Goswami and S. Tewari. 'Chiral magnetic effect of Weyl fermions and its applications to cubic noncentrosymmetric metals' (2013). arXiv: 1311.1506v2.

[70] A. A. Zyuzin, S. Wu and A. A. Burkov. 'Weyl semimetal with broken time reversal and inversion symmetries'. *Phys. Rev. B* 85, 165110 (2012). arXiv: 1201.3624.

[71] Y. Chen, S. Wu and A. A. Burkov. 'Axion response in Weyl semimetals'. *Phys. Rev. B* 88, 125105 (2013). arXiv: 1306.5344v2.

[72] N. Yamamoto. 'Generalized Bloch theorem and chiral transport phenomena'. *Phys. Rev. D* 92, 085011 (2015). arXiv: 1502.01547.

[73] D. Hou, H. Liu and H.-c. Ren. 'Some Field Theoretic Issues Regarding the Chiral Magnetic Effect'. *JHEP* 2011, 046 (2011). arXiv: 1103.2035v2.

[74] K. Jensen. 'Triangle Anomalies, Thermodynamics, and Hydrodynamics'. *Phys. Rev. D* 85, 125017 (2012). arXiv: 1203.3599.

[75] M. A. Stephanov and Y. Yin. 'Chiral Kinetic Theory'. *Phys. Rev. Lett.* 109, 162001 (2012). arXiv: 1207.0747.

[76] D. T. Son and N. Yamamoto. 'Berry Curvature, Triangle Anomalies, and the Chiral Magnetic Effect in Fermi Liquids'. *Phys. Rev. Lett.* 109, 181602 (2012). arXiv: 1203.2697.

[77] C.-C. Lee et al. 'Fermi arc topology and interconnectivity in Weyl fermion semimetals TaAs, TaP, NbAs, and NbP'. *Phys. Rev. B* 92, 235104 (2015). arXiv: 1508.05999.

[78] Y. Akamatsu and N. Yamamoto. 'Chiral Plasma Instabilities'. *Phys. Rev. Lett.* 111, 052002 (2013). arXiv: 1302.2125v2.

[79] C. Manuel and J. M. Torres-Rincon. 'Dynamical evolution of the chiral magnetic effect: Applications to the quark-gluon plasma'. *Phys. Rev. D* 92 (2015). arXiv: 1501.07608.

[80] Z. V. Khaidukov et al. 'On Magnetostatics of Chiral Media' (2013). arXiv: 1307.0138.

[81] V. P. Kirilin, A. V. Sadofyev and V. I. Zakharov. 'Anomaly and long-range forces'. In: *Proceedings, 100th anniversary of the birth of I.Ya. Pomeranchuk*. World Scientific, 2014. arXiv: 1312.0895.

[82] A. Boyarsky, J. Froehlich and O. Ruchayskiy. 'Self-consistent evolution of magnetic fields and chiral asymmetry in the early Universe'. *Phys. Rev. Lett.* 108, 031301 (2011). arXiv: 1109.3350v2.

[83] P. V. Buividovich and M. V. Ulybyshev. 'Numerical study of chiral plasma instability within the classical statistical field theory approach'. *Phys. Rev. D* 94, 025009 (2015). arXiv: 1509.02076.

[84] A. Sekine et al. 'Strong Coupling Expansion in a Correlated Three-Dimensional Topological Insulator'. *Phys. Rev. B* 87, 165142 (2013). arXiv: 1301.4424.

[85] A. Sekine and K. Nomura. 'Weyl Semimetal in the Strong Coulomb Interaction Limit'. *J. Phys. Soc. Jpn.* 83, 094710 (2013). arXiv: 1309.1079.

[86] A. Sekine and K. Nomura. 'Axionic Antiferromagnetic Insulator Phase in a Correlated and Spin-Orbit Coupled System'. *J. Phys. Soc. Jpn.* 83, 104709 (2014). arXiv: 1401.4523.

[87] Y. Araki et al. 'Phase structure of topological insulators by lattice strong-coupling expansion'. *PoS(LATTICE 2013)050* (2013). arXiv: 1311.3973.

[88] R. Peierls. 'Zur Theorie des Diamagnetismus von Leitungselektronen'. *Z. Phys.* 80 (1933), pp. 763–791. DOI: 10.1007/BF01342591.

[89] J. M. Luttinger. 'The Effect of a Magnetic Field on Electrons in a Periodic Potential'. *Phys. Rev.* 84 (1951), pp. 814–817. DOI: 10.1103/PhysRev.84.814.

[90] G. H. Wannier. 'Dynamics of Band Electrons in Electric and Magnetic Fields'. *Rev. Mod. Phys.* 34 (1962), pp. 645–655. DOI: 10.1103/RevModPhys.34.645.

[91] R. L. Stratonovich. 'On a Method of Calculating Quantum Distribution Functions'. *Soviet Phys. Doklady* 2, 416 (1958).

[92] J. Hubbard. 'Calculation of Partition Functions'. *Phys. Rev. Lett.* 3 (1959), pp. 77–78. DOI: 10.1103/PhysRevLett.3.77.

[93] R. Storn and K. Price. 'Differential Evolution – A Simple and Efficient Heuristic for global Optimization over Continuous Spaces'. *J. Global Optim.* 11 (1997), pp. 341–359. DOI: 10.1023/A:1008202821328.

[94] S. Aoki. 'New phase structure for lattice QCD with Wilson fermions'. *Phys. Rev. D* 30 (1984), pp. 2653–2663. DOI: 10.1103/PhysRevD.30.2653.

[95] R. Li et al. 'Dynamical Axion Field in Topological Magnetic Insulators'. *Nat. Phys.* 6 (2009), pp. 284–288. arXiv: 0908.1537v1.

[96] J. Maciejko and R. Nandkishore. 'Weyl semimetals with short-range interactions'. *Phys. Rev. B* 90, 035126 (2013). arXiv: 1311.7133.

[97] J. Wang, B. Lian and S.-C. Zhang. 'Dynamical axion field in a magnetic topological insulator superlattice'. *Phys. Rev. B* 93, 045115 (2015). arXiv: 1512.00534.

[98] A. Gynther et al. 'Holographic Anomalous Conductivities and the Chiral Magnetic Effect'. *JHEP* 2011, 110 (2010). arXiv: 1005.2587.

[99] I. Amado, K. Landsteiner and F. Pena-Benitez. 'Anomalous transport coefficients from Kubo formulas in Holography'. *JHEP* 2011, 081 (2011). arXiv: 1102.4577.

[100] K. Landsteiner, E. Megias and F. Pena-Benitez. 'Anomalous Transport from Kubo Formulae'. In: *Strongly Interacting Matter in Magnetic Fields*. Springer Nature, 2012, pp. 433–468. arXiv: 1207.5808.

[101] J. Behrends et al. 'Visualizing the chiral anomaly in Dirac and Weyl semimetals with photoemission spectroscopy'. *Phys. Rev. B* 93, 075114 (2015). arXiv: 1503.04329.

[102] F. W. Olver et al. *NIST Handbook of Mathematical Functions*. New York, USA: Cambridge University Press, 2010.

[103] E. V. Gorbar et al. 'Chiral separation and chiral magnetic effects in a slab: The role of boundaries'. *Phys. Rev. B* 92, 245440 (2015). arXiv: 1509.06769.

[104] S. G. Johnson. *Cubature (Multi-dimensional integration)*. URL: http://ab-initio.mit.edu/wiki/index.php/Cubature.

[105] K.-Y. Kim, B. Sahoo and H.-U. Yee. 'Holographic chiral magnetic spiral'. *JHEP* 2010, 005 (2010). arXiv: 1007.1985.

[106] C. A. Ballon-Bayona, K. Peeters and M. Zamaklar. 'A non-homogeneous ground state of the low-temperature Sakai-Sugimoto model'. *JHEP* 2011, 092 (2011). arXiv: 1104.2291.

[107] A. Ballon-Bayona, K. Peeters and M. Zamaklar. 'A chiral magnetic spiral in the holographic Sakai-Sugimoto model'. *JHEP* 2012, 164 (2012). arXiv: 1209.1953.

[108] G. B. Halász and L. Balents. 'Time-reversal invariant realization of the Weyl semimetal phase'. *Phys. Rev. B* 85, 035103 (2011). arXiv: 1109.6137.

[109] J. Kogut and L. Susskind. 'Hamiltonian formulation of Wilson's lattice gauge theories'. *Phys.Rev. D* 11 (1975), pp. 395–408. DOI: 10.1103/PhysRevD.11.395.

[110] M. Creutz, I. Horváth and H. Neuberger. 'A new fermion Hamiltonian for lattice gauge theory'. *Nucl. Phys. B Proc. Suppl.* 106-107 (2001), pp. 760–762. arXiv: hep-lat/0110009.

[111] M. Knecht et al. 'New nonrenormalization theorems for anomalous three point functions'. *JHEP* 2004 (2003), pp. 035–035. arXiv: hep-ph/0311100.

[112] M. Puhr and P. Buividovich. 'A numerical method to compute derivatives of functions of large complex matrices and its application to the overlap Dirac operator at finite chemical potential'. *Comput. Phys. Commun.* 208 (2016), pp. 135–148. arXiv: 1604.08057.

[113] M. Puhr and P. Buividovich. 'A method to compute derivatives of functions of large complex matrices'. *PoS(LATTICE2016)257* (2016). arXiv: 1611.00195.

[114] M. Puhr and P. V. Buividovich. 'A Method to Calculate Conserved Currents and Fermionic Force for the Lanczos Approximation to the Overlap Dirac Operator'. *PoS(LATTICE2014)047* (2014). arXiv: 1411.0477.

[115] M. Puhr and P. Buividovich. 'A numerical study of non-perturbative corrections to the Chiral Separation Effect in quenched finite-density QCD'. *Submitted to PRL* (2016). arXiv: 1611.07263.

[116] V. Skokov, A. Illarionov and V. Toneev. 'Estimate of the magnetic field strength in heavy-ion collisions'. *Int. J. Mod. Phys. A* 24 (2009), pp. 5925–5932. arXiv: 0907.1396v1.

[117] J. Liao. 'Chiral Magnetic Effect in Heavy Ion Collisions'. *Nucl. Phys. A* 956 (2016), pp. 99–106. arXiv: 1601.00381v1.

[118] A. Yamamoto. 'Chiral magnetic effect in lattice QCD with a chiral chemical potential'. *Phys. Rev. Lett.* 107 (2011), p. 031601. arXiv: 1105.0385.

[119] A. Yamamoto. 'Lattice study of the chiral magnetic effect in a chirally imbalanced matter'. *Phys. Rev. D* 84 (2011), p. 114504. arXiv: 1111.4681.

[120] P. V. Buividovich. 'Overlap Dirac operator with chiral chemical potential and Chiral Magnetic Effect on the lattice'. *PoS(Lattice2013) 179* (2013). arXiv: 1309.2850.

[121] D. E. Kharzeev and H.-U. Yee. 'Chiral Magnetic Wave'. *Phys. Rev. D* 83, 085007 (2010). arXiv: 1012.6026v2.

[122] Y. Burnier et al. 'Chiral magnetic wave at finite baryon density and the electric quadrupole moment of quark-gluon plasma in heavy ion collisions'. *Phys. Rev. Lett.* 107, 052303 (2011). arXiv: 1103.1307v1.

[123] Y. Burnier et al. 'From the chiral magnetic wave to the charge dependence of elliptic flow' (2012). arXiv: 1208.2537v1.

[124] Y. Kikukawa and A. Yamada. 'A note on the exact lattice chiral symmetry in the overlap formalism'. *Nucl. Phys. B* 547 (1998), pp. 413–423. arXiv: hep-lat/9810024.

[125] P. Hasenfratz et al. 'Testing the fixed-point QCD action and the construction of chiral currents'. *Nucl. Phys. B* 643 (2002), pp. 280–320. arXiv: hep-lat/0205010.

[126] N. J. Higham. *Functions of Matrices: Theory and Computation*. Society for Industrial & Applied Mathematics (SIAM), 2008.

[127] G. H. Golub and C. F. Van Loan. *Matrix Computations*. Third Edition. The Johns Hopkins University Press Baltimore and London, 1996.

[128] G. Fischer. *Lineare Algebra*. Springer Nature, 2014.

[129] V. Y. Pan and Z. Q. Chen. 'The complexity of the matrix eigenproblem'. In: *Proceedings of the thirty-first annual ACM symposium on Theory of computing - STOC '99*. Association for Computing Machinery (ACM), 1999.

[130] F. Le Gall. 'Powers of Tensors and Fast Matrix Multiplication'. In: *Proceedings of the 39th International Symposium on Symbolic and Algebraic Computation - ISSAC '14*. Association for Computing Machinery (ACM), 2014. arXiv: 1401.7714.

[131] A. D. Kennedy. 'Approximation Theory for Matrices'. *Nucl. Phys. Proc. Suppl.* 128C (2004), pp. 107–116. arXiv: hep-lat/0402037.

[132] L. Giusti et al. 'Numerical techniques for lattice QCD in the ϵ–regime'. *Comput.Phys.Commun.* 153 (2002), pp. 31–51. arXiv: hep-lat/0212012.

[133] J. van den Eshof et al. 'Numerical Methods for the QCD Overlap Operator: I. Sign-Function and Error Bounds'. *Comput. Phys. Commun.* 146 (2002), pp. 203–224. arXiv: hep-lat/0202025.

[134] N. Cundy, A. Kennedy and A. Schäfer. 'A lattice Dirac operator for QCD with light dynamical quarks'. *Nucl. Phys. B* 845 (2010), pp. 30–47. arXiv: 1010.5629v3.

[135] J. Bloch, T. Breu and T. Wettig. 'Comparing iterative methods to compute the overlap Dirac operator at nonzero chemical potential'. *PoS(LATTICE2008)027* (2008). arXiv: 0810.4228.

[136] J. C. R. Bloch et al. 'Short-recurrence Krylov subspace methods for the overlap Dirac operator at nonzero chemical potential'. *Comput. Phys. Commun.* 181 (2009), pp. 1378–1387. arXiv: 0910.1048.

[137] J. Bloch et al. 'An iterative method to compute the sign function of a non-Hermitian matrix and its application to the overlap Dirac operator at nonzero chemical potential'. *Comput. Phys. Commun.* 177 (2007), pp. 933–943. arXiv: 0704.3486.

[138] J. Bloch and S. Heybrock. 'A nested Krylov subspace method to compute the sign function of large complex matrices'. *Comput. Phys. Commun.* 182 (2011), pp. 878–889. DOI: 10.1016/j.cpc.2010.09.022.

[139] A. Griewank and A. Walther. *Evaluating Derivatives: Principles and Techniques of Algorithmic Differentiation*. SIAM, 2008.

[140] R. Mathias. 'A Chain Rule for Matrix Functions and Applications'. *SIAM J. Matrix Anal. & Appl.* 17 (1996), pp. 610–620. DOI: 10.1137/S0895479895283409.

[141] R. B. Lehoucq, D. C. Sorensen and C. Yang. *ARPACK Users' Guide: Solution of Large-Scale Eigenvalue Problems with Implicitly Restarted Arnoldi Methods*. SIA, 1998.

[142] Z. Fodor, S. D. Katz and K. K. Szabo. 'Dynamical overlap fermions, results with hybrid Monte-Carlo algorithm'. *JHEP* 0408 (2003), p. 003. arXiv: hep-lat/0311010.

[143] N. Cundy et al. 'Numerical Methods for the QCD Overlap Operator IV: Hybrid Monte Carlo'. *Comput. Phys. Commun.* 180 (2009), pp. 26–54. arXiv: hep-lat/0502007.

[144] Z. Xianyi et al. *OpenBLAS*. 2016. URL: http://www.openblas.net.

[145] C. Gattringer et al. 'Chiral symmetry restoration and the Z3 sectors of QCD'. *Phys. Rev. D* 66, 054502 (2002). arXiv: hep-lat/0202009v1.

[146] S. J. Dong and K. F. Liu. 'Stochastic Estimation with Z_2 Noise'. *Phys.Lett. B* 328 (1993), pp. 130–136. arXiv: hep-lat/9308015.

[147] R. D. Pisarski. 'In a hot, chirally symmetric phase, π^0 doesn't go into 2γ, but $\pi^0\sigma$ does'. In: *From Thermal Field Theory to Neural Networks: A Day to Remember Tanguy Altherr*. World Scientific Pub Co Pte Lt, 1996, pp. 41–47. arXiv: hep-ph/9510375v1.

[148] F. Gelis. 'Ambiguities in the zero momentum limit of the thermal $\pi^0\gamma\gamma$ triangle diagram'. *Phys. Rev. D* 59, 076004 (1998). arXiv: hep-ph/9806425v1.

[149] L. R. Baboukhadia, V. Elias and M. D. Scadron. 'Linear Sigma Model Linkage with Nonperturbative QCD'. *J. Phys. G: Nucl. Part. Phys.* 23 (1997), pp. 1065–1075. arXiv: hep-ph/9708431.

[150] M. H. Al-Hashimi and U. .-.-J. Wiese. 'Discrete Accidental Symmetry for a Particle in a Constant Magnetic Field on a Torus'. *Ann. Phys.* 324 (2009), pp. 343–360. arXiv: 0807.0630v1.

[151] R. G. Edwards et al. 'Chiral Condensate in the Deconfined Phase of Quenched Gauge Theories'. *Phys. Rev. D* 61, 074504 (1999). arXiv: hep-lat/9910041v1.

[152] J. Kiskis and R. Narayanan. 'Quenched divergences in the deconfined phase of SU(2) gauge theory'. *Phys. Rev. D* 64, 117502 (2001). arXiv: hep-lat/0106018v2.

[153] G. Basar, G. V. Dunne and D. E. Kharzeev. 'Electric dipole moment induced by a QCD instanton in an external magnetic field'. *Phys. Rev. D* 85 (2012). arXiv: 1112.0532v1.

[154] M. A. Stephanov. 'Random matrix model of QCD at finite density and the nature of the quenched limit'. *Phys. Rev .Lett.* 76 (1996), pp. 4472–4475. arXiv: hep-lat/9604003v2.

[155] V. P. Gusynin, V. A. Miransky and I. A. Shovkovy. 'Dimensional Reduction and Dynamical Chiral Symmetry Breaking by a Magnetic Field in $3+1$ Dimensions'. *Phys. Lett. B* 349 (1994), pp. 477–483. arXiv: hep-ph/9412257v1.

[156] E. V. Gorbar, V. A. Miransky and I. A. Shovkovy. 'Chiral asymmetry of the Fermi surface in dense relativistic matter in a magnetic field'. *Phys. Rev. C* 80, 032801 (2009). arXiv: 0904.2164v2.

[157] C. Wu and S.-C. Zhang. 'A sufficient condition for the absence of the sign problem in the fermionic quantum Monte-Carlo algorithm'. *Phys. Rev. B* 71, 155115 (2005). arXiv: cond-mat/0407272v3.

[158] T. Ojanen. 'Helical Fermi arcs and surface states in time-reversal invariant Weyl semimetals'. *Phys. Rev. B* 87, 245112 (2013). arXiv: 1304.3601v2.

[159] M. Lüscher and P. Weisz. 'Computation of the action for on-shell improved lattice gauge theories at weak coupling'. *Phys. Lett. B* 158 (1985), pp. 250–254. DOI: 10.1016/0370-2693(85)90966-9.

[160] G. P. Lepage and P. B. Mackenzie. 'On the Viability of Lattice Perturbation Theory'. *Phys. Rev. D* 48 (1992), pp. 2250–2264. arXiv: hep-lat/9209022v1.

[161] M. Alford et al. 'Lattice QCD on Small Computers'. *Phys. Lett. B* 361 (1995), pp. 87–94. arXiv: hep-lat/9507010v3.

[162] J. Snippe. 'Computation of the one-loop Symanzik coefficients for the square action'. *Nucl. Phys. B* 498 (1997), pp. 347–396. arXiv: hep-lat/9701002v1.

[163] M. Lüscher and P. Weisz. 'On-shell improved lattice gauge theories'. *Comm. Math. Phys.* 97.1-2 (Mar. 1985), pp. 59–77. DOI: 10.1007/BF01206178; M. Lüscher and P. Weisz. 'Erratum: On-shell improved lattice gauge theories'. *Commun. Math. Phys.* 98.3 (Sept. 1985), pp. 433–433. DOI: 10.1007/bf01205792.

[164] C. Gattringer, R. Hoffmann and S. Schaefer. 'Setting the scale for the Lüscher-Weisz action'. *Phys. Rev. D* 65 (2001). arXiv: hep-lat/0112024.

[165] R. Sommer. 'A New Way to Set the Energy Scale in Lattice Gauge Theories and its Application to the Static Force and α_s in SU(2) Yang–Mills Theory'. *Nucl. Phys. B* 411 (1993), pp. 839–854. arXiv: hep-lat/9310022v1.